Sensing impacts to the Earth-ionosphere waveguide from terrestrial and space weather

Todd Anderson

A dissertation

submitted in partial fulfillment of the

requirements for the degree of

Doctor of Philosophy

University of Washington
2023

Reading Committee:
Robert H. Holzworth, II, Chair
Michael P. McCarthy
Abram H. Jacobson

Program Authorized to Offer Degree:
Earth and Space Sciences

University of Washington

Abstract

Sensing impacts to the Earth-ionosphere waveguide from terrestrial and space weather

Todd Anderson

Chair of the Supervisory Committee:

Robert H. Holzworth, II
Department of Earth and Space Sciences

The Earth's lower ionosphere forms the lower-altitude limit of space plasma near the Earth, coexisting with the neutral mesosphere-lower thermosphere at 60-150 km altitude. In-situ measurements of this region are made difficult by the significant neutral density there, preventing long-duration satellite orbits, while at the same time being too high for balloons to reach. The ionization of this region is perturbed by dynamic solar processes. Solar flares and precipitating radiation belt particles enhance low-altitude ionization, causing communication blackouts, and generating ozone-destroying radicals in the mesosphere. In order to quantify the global impacts of solar flare ionization and energetic electron precipitation (EEP) on low-altitude ionization, measurements of the spatial extent of solar flare and EEP signatures are needed.

The Earth-ionosphere waveguide, a region formed by the lower ionosphere and conducting Earth surface, allows radio waves in the very low frequency (VLF) band to propagate long distances around the world. This fact is useful for communication and other technological means, and also allows for the location of global lightning by sensing the radio waves emitted by lightning strokes, called sferics.

Previous work has analyzed signal propagation in this waveguide from both natural (lightning) and artificial (transmitter) sources, in order to study the response of the waveguide to space weather drivers. However, such efforts have focused on accurately measuring ionosphere conditions either at a small number of specific locations relative to source lightning, or else along long propagation paths between a small number of source-receiver pairs.

Here, we present efforts to detect and quantify the spatial signatures of both solar flare and EEP ionization in the Earth-ionosphere waveguide using lightning location data from the World Wide Lightning Location Network. First, we demonstrate a method using only changes in the stroke-to-station propagation path distribution to infer ionization associated with solar flares, and compare the timing of enhanced ionization with geostationary X-ray flux measurements for two X-class solar flares in September 2017. Then, we expand the method to include sferic waveform information, calculate the range-normalized dispersion of each WWLLN sferic, and investigate changes in range-normalized dispersion statistics associated with enhanced >300 keV electron flux detected by POES spacecraft. We find that spatiotemporal averaging of WWLLN propagation paths, and of sferic properties associated with these paths, is an effective proxy for detecting the onset and extent of enhanced ionization during strong solar flares, and may be used to determine changes in the lower ionosphere height associated with EEP.

Additionally, the Earth-ionosphere waveguide, a spherical capacitor, plays host to the global electric circuit, a current system carrying charge to the ionosphere from global thunderstorms and other drivers, where it then disperses horizontally and leaks through the fair weather atmosphere to the ground. The fair-weather current density in this circuit has been thought to be spatially invariant, as supported by simultaneous measurements of the electric field and conductivity by separated stratospheric balloons. Were this invariance to be well-established, studies to determine the relative importance of various drivers to the circuit could open the door for long-term observations of global thunderstorm activity and other large-scale atmospheric electrical parameters using small numbers of instrumented stratospheric balloons.

In order to test this expectation, we launched two stratospheric balloons in June 2021 that measured electric fields and conductivity in the stratosphere over several days. We found that, in disagreement with previous findings, the two balloons measured vertical return current density that differed by as much as a factor of two. We compared the balloon tracks to WWLLN and spaceborne lightning detections, measurements of cloud-top temperature related to vigorous convection, and precipitation estimates, and found no significant weather near either balloon that could account for the discrepancy in the return current density. This result suggests that fair-weather component of the global electric circuit is not as spatially invariant as previously thought, and further investigation into the causes of this invariance is needed to determine the relationships between atmospheric electrical drivers and the global circuit response.

Acknowledgements

My supervisory committee, like all good PhD supervisory committees, was immensely useful in completing the work in this dissertation; I am fortunate enough to say that the process, while perhaps longer than expected, was nearly always enjoyable and exciting. Bob Holzworth and Michael McCarthy allowed me considerable freedom to explore the ideas I was interested in, despite these ideas not always being aligned with our main project priorities. They also allowed and encouraged my participation in development and outreach activities, which have helped further my career in space science. They have provided training opportunities in a rich variety of experiment and analysis techniques, giving me the tools to shape my own research program. Abe Jacobson has provided significant and helpful input to the chapters on subionospheric VLF wave propagation, and additionally has encouraged and helped enable the next steps in my space science journey.

In addition my supervisory committee, a number of people contributed to the success of this work. James Brundell provided helpful guidance on the intricacies of WWLLN workings, and was instrumental in the nimble wrangling of WWLLN sferic data, as was Carl Christofferson. Steven Peterzen and the ISTAR Group provided launch support and consulting services at the Sisters Eagle Airport, whose operators also generously supported our launch campaign with hangar and tarmac space.

I immensely enjoyed working with the students and faculty in the Earth and Space Sciences. I learned so much about aspects of geophysics and geology that I would have missed in traditional Physics department, both at department colloquia and around the keg afterwards. I look forward to continuing to work and recreate with many of them in the future.

Finally, I owe a great debt to my partner Anabelle, for her unparalleled patience, understanding and support over the course of my long PhD.

Contents

List of Figures

List of Tables

Chapter 1

Introduction

The ionosphere, a layer of plasma maintained by solar ionization of the neutral atmosphere, is a fundamental feature in Earth's nearby space environment. This partially-ionized plasma plays host to many important physical processes and coupling mechanisms across significant length scales. The ionosphere is driven from above by solar radiation, and so changes in the Sun's radiation output results in changes in the ionosphere electron density and altitude. Since the ionosphere spans the transition between highly collisional neutral atmosphere at its lower boundary ($< 60\,\mathrm{km}$) and nearly collisionless plasma at its highest reaches ($> 1000\,\mathrm{km}$), it contains the footprints of many electromagnetic and plasma processes that occur at greater distances in the magnetosphere. Perhaps the most charismatic of these is the aurora, formed when low-energy ($\sim 10\,\mathrm{keV}$) magnetospheric plasma precipitates down geomagnetic field lines until collides with and excites neutral species in the mesosphere and thermosphere, which then emit photons that give the aurora its familiar range of colors.

Studying the many processes that give rise to variability in the lower ionosphere is needed both to understand the dynamics and coupling mechanisms at play in this region, but also to quantify the impact these phenomena make on human life and infrastructure. Perhaps the most compelling reason to carefully study this region is its importance to radio communication systems. Satellite communication systems, including global navigational satellite systems (GNSS), rely on radio propagation between orbiting satellites to ground stations, necessarily transiting the ionosphere. Variation in electron density with altitude results in refraction of the transionospheric radio signal. Under quiescent ionospheric conditions, this refraction can be predicted

and corrected for, but a host of space and terrestrial weather phenomena can perturb the ionosphere and make transionospheric radio communication difficult. Lower frequencies communication techniques that rely on reflection off the lower ionosphere may be similarly disrupted.

Although its altitude range varies diurnally, the denser lower regions of the ionosphere lie between 60 and $300\,\mathrm{km}$, presenting a challenge to scientists hoping to measure its properties. Due to the high neutral density in this altitude range, satellites cannot orbit for long before drag causes their orbits to decay. At lower altitudes, even the highest-reaching stratospheric balloons achieve heights of perhaps $40\,\mathrm{km}$, a little more than halfway to the lowest parts of the dayside ionosphere. In-situ measurements can therefore only be performed by short duration means, with sounding rockets being the most common. Even these typically target higher altitude regions, making direct observations of the lower ionosphere rare. The lack of in-situ measurements has led to the lower ionosphere, between 60 and about $100\,\mathrm{km}$, being called the "ignorosphere".

Because of this measurement difficulty, remote sensing efforts to study the lower ionosphere are crucial to understanding its dynamics and the mechanisms by which space drivers from higher altitudes couple with terrestrial and atmospheric drivers from below. Fortunately, the same radio frequencies that are affected by space and terrestrial weather impacts to the ionosphere provide means by which to study its variability. By studying changes to radio propagation and comparing these to supplemental data on perturbative phenomena, we can deduce the effects of various types of space or terrestrial drivers on the key altitude region of the ionosphere where our radio signal refracts or reflects.

The very-low-frequency (VLF) band, between 3 and $30\,\mathrm{kHz}$, is an important one for remote sensing of the lower ionosphere. VLF radio waves reflect in this region, and by reflecting also from the conductive ground, they may propagate long distances around the Earth; this pair of concentric reflectors forms the Earth-ionosphere waveguide (EIWG). Since the properties of the ground reflector are largely invariant with time, changes in VLF propagation in the EIWG can be used to infer changes in the reflection region of the lower ionosphere.

Two space weather phenomena are particularly compelling for study with subionospheric VLF techniques. The first is extreme solar flares, sudden enhancements in solar X-ray and extreme ultraviolet flux that are associated with sunspot regions. These flares cause dramatically enhanced ionization in the day-

side lower ionosphere, lowering the reflection height for all radio frequencies, and thereby increasing the electron-neutral collision frequency at this reflection region. Reflecting radio waves are therefore significantly attenuated when propagating through the subsolar region during extreme solar flares. Solar flares can thus cause dropouts in HF over-the-horizon radio communication, including the systems used by commercial aircraft. They also cause significant attenuation of VLF radio waves. Fortunately, solar flares are relatively well-studied phenomena, and their impact region on Earth is highly predictable, being related entirely to the amount of atmosphere the solar X-rays must penetrate to reach a given altitude.

Another space weather phenomenon that impacts this altitude region is less predictable. The Earth's radiation belts, a pair of roughly-toroidal regions of high-energy ($100\,\mathrm{keV} - 10\,\mathrm{MeV}$) plasma, exhibit dynamic loss and refilling during geomagnetic substorms. These substorms cause energetic electron precipitation (EEP) into the high-latitude regions immediately below the auroral oval in latitude. Like auroral electrons, EEP deposits energy into the neutral atmosphere through collisions with neutral species. Because these electrons have far more energy than auroral electrons, they are able to penetrate to far deeper altitudes, and ionize neutral species in collisions. Ionization in the mesosphere ($50-80\,\mathrm{km}$) and lower thermosphere ($> 80\,\mathrm{km}$) results in the production of odd-nitrogen (NO_x) and odd-hydrogen radicals (HO_x), both of which catalytically destroy ozone. EEP during substorms can therefore cause significant depletions of mesospheric ozone. Although both NO_x and HO_x are destroyed by solar UV, when these chemicals are produced by EEP in the polar winter, they may be circulated downwards in the polar winter vortex and destroy stratospheric ozone.

Unlike solar flares, EEP regions are difficult to predict. Only a few polar-orbiting spacecraft detect precipitating electrons, so while these may be used to build long-time-averaged statistics of EEP latitude and local dependence, resolving the spatial characteristics of individual events is impractical with in-situ particle detectors. Although EEP does produce photons, rather than stimulating emission from atmospheric species in or near the visible range, bremsstrahlung X-rays are instead produced by the relativistic electrons. These X-rays are mostly absorbed by the troposphere, so may only be detected from below by balloon-borne instruments; alternatively, backscattered X-rays may be detected from space. Several spacecraft missions have imaged X-rays associated with EEP regions with varying spatial and spectral resolution, and development of the next generation of these imaging systems is ongoing [*Berland et al.*, 2023].

Since EEP enhances ionization at VLF reflection altitudes, VLF waves propagating below EEP regions may be sensitive to particle precipitation. Both solar flares and EEP have been studied using subionospheric techniques. These chiefly rely on powerful transmitters, operated by navies for long-distance encrypted communication with submarines, and receiver networks that study perturbations to the transmitter signals. Such transmitter-receiver networks measure waveguide conditions integrated over each propagation path. These networks run the gamut from single transmitter-receiver pairs, to global networks like AARDDVARK, to regional networks with receivers deployed strategically with spatial resolution in mind. Although transmitter-receiver networks have proven highly successful at estimating the ionosphere response to both solar flares and EEP, they have done so with varying degrees of spatial resolution and accuracy. Understanding the spatial characteristics of EEP especially is needed in order to accurately estimate the location and amount of NO_x and HO_x production.

To fill this measurement gap, we can turn to another type of VLF receiver network. Lightning location networks receive the VLF portion of the broadband atmospheric waves, called sferics, launched by lightning strokes around the world. Sferics propagate in the EIWG the same way transmitter signals do, and hence are sensitive to lower ionosphere conditions. Although lightning provides a transient and highly variable VLF source, its globally-distributed nature means that the propagation paths between lightning sources and detecting stations can cover more of the Earth than transmitter-receiver networks, and with greater density of paths. Because lightning occurs clustered in thunderstorms, sferic propagation paths can be used to sample waveguide conditions in dense bundles, where a transmitter-receiver pair will access only a single path.

Global thunderstorms also contribute to another electric system in the EIWG. The global electric circuit (GEC) is a current system wherein electric charge is driven upwards from the troposphere to the conducting lower ionosphere, disperses horizontally there, and returns to the Earth surface via the weakly-conducting fair-weather middle atmosphere. The source of lower and middle atmosphere conductivity is cosmic rays, even more energetic than EEP; this conductivity allows a fair-weather return current to flow, while thunderstorms and other GEC drivers maintain roughly $250\,\mathrm{keV}$ ionospheric potential relative to the ground. Although tropospheric convection, aerosols and anthropogenic interference prevent easy ground-based current measurements, the fair-weather return current density may be estimated by measurements of the electric field and conductivity in the stratosphere.

The GEC is a compelling target for study because determination of the relationships between its drivers and currrent response would allow investigation in global atmospheric electrical coupling mechanisms, and proxies could then be used to estimate one GEC parameter, which may be important for meteorological or climate studies, with measurements of another. Because middle atmospheric conductivity and the fair-weather electric field depend on the cosmic ray flux at Earth and the height of the lower ionosphere, both of which are affected by solar activity, the GEC provides a coupling mechanism between solar and space weather and atmospheric electricity.

However, studies of this coupling require knowledge of the impacts of GEC drivers, such as thunderstorms and electrified precipitation, on the fair-weather current. Although a long-time-averaged relationship between these has long been established, there is considerable uncertainty around the instantaneous state of the fair-weather current for given driver input. Accurate measurements of the variability of this fair-weather current will be the first step toward estimating the relative contributions of different GEC drivers.

This dissertation will address the broad topic of impacts to the Earth-ionosphere waveguide by space and terrestrial drivers using three separate analyses. In Chapters 3 and 4, we demonstrate new techniques to investigate the waveguide response to first solar flares, then EEP. We use sferics detected by the World Wide Lightning Location Network (WWLLN), a network of around 80 stations; the solar flare response is studied using only the time variation of WWLLN sferic propagation paths, while the EEP response is determined through spatiotemporal averaging of sferic dispersion. Chapter 5 reports on a stratospheric balloon campaign to test the long-standing hypothesis that the fair-weather return current density measured in the stratosphere is spatially invariant, and to gather high-quality measurements of this return current density for later comparison with estimates of global thunderstorm activity.

Chapter 2

Background information: the ionosphere, Earth-ionosphere waveguide, and overview of the World Wide Lightning Location Network

2.1 Earth's ionosphere

Earth's atmosphere, in simple terms, is a mixture of gases and vapor that surrounds the planet. Gravity pulls each molecule down towards the surface, resulting in increasing density at lower altitudes; collisions between particles within this density gradient buoy particles upwards. In the troposphere, these factors and surface interactions give rise to vigorous convection and dynamic weather, but at higher altitudes, the density of gas decreases exponentially with height. The precise altitude where Earth's atmosphere ends and space begins is therefore arbitrarily defined, at least by density of neutral gas.

Imposed at the top of Earth's atmosphere is solar radiation across much of the electromagnetic spectrum, from X-rays to microwave radio waves. The higher-energy portion of this spectrum, particularly X-rays and extreme UV photons, ionize any atmospheric particles they come across. This ionization process results in the photons' absorption, so less and less of this hard radiation makes it through the atmosphere to lower altitudes as the atmosphere becomes thicker.

The interplay between the exponentially-decaying altitude profile of atmospheric neutral density and the Sun's finite radiation arriving at the top of the atmosphere results in a region of plasma near the Earth known as the ionosphere. Since the ionosphere is generated by ionization of neutral atoms, and not by significant transport of plasma of a particular charge polarity from some other region, its overall charge is neutral, and the number of electrons in any given region should be equal to the sum of positive ion charge across whatever ion species are in that region. The ionosphere can then be conveniently represented by its electron density profile. In the upper ionosphere, ionization is primarily limited by the tenuous neutral density rather than radiation intensity, and the upper ionosphere electron density profile follows the same exponential decay as the middle atmosphere. The edge of the lower ionosphere is defined when the amount of hard solar radiation left to ionize the neutral gas becomes depleted by ionizing the plasma above, and the neutral density increases such that the electron density produced by photoionization here is quickly negated by recombination with positive ions, or else attachment to neutrals to form heavier negative ions. Between this lower boundary and the top of the ionosphere, there are several peaks formed by the interaction of solar radiation with different gas constituents.

Because the ionosphere is fundamentally generated by interaction of the neutral atmosphere with solar radiation, the ionosphere profile varies dramatically with the diurnal cycle. During the day, the lowest region

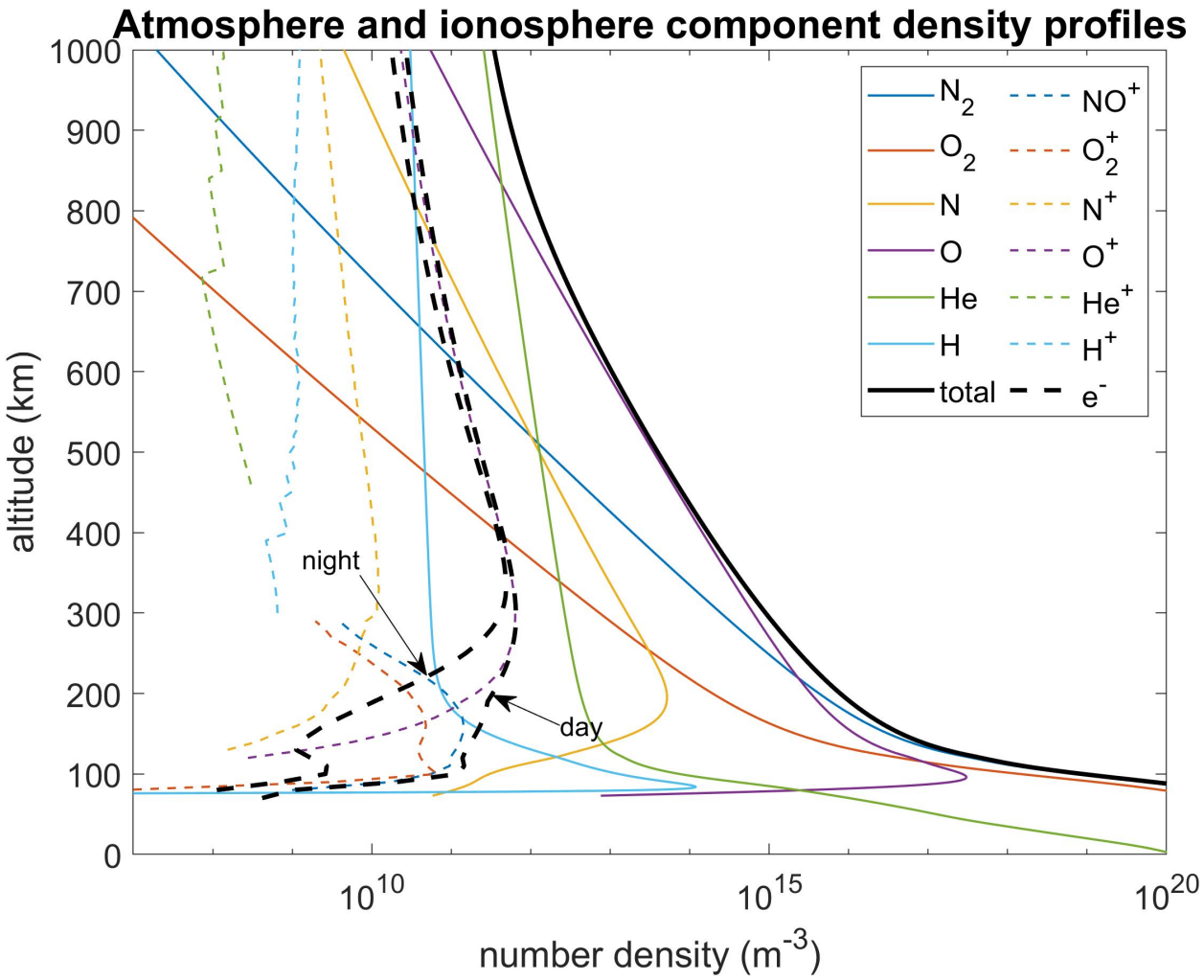

Figure 2.1: Neutral, ion and electron density profiles below 1000 km altitude. The black dashed lines show the electron density profiles during night- and day time; all other neutral and ion densities are daytime profiles.

of the ionosphere, called the D region, reaches between 60 and 80 km, with the E and F regions above. The D region disappears entirely at night, and the E region becomes the lowest layer of the ionosphere, at around 100 km. Sample daytime ionosphere and neutral atmosphere profiles, as well as the nighttime electron density profile, for nominal conditions over Seattle, WA are shown in figure 2.1. Neutral densities are calculated using the NRL MSISE-00 model [*Picone et al.*, 2002], and ion and electron densities are calculated using the International Reference Ionosphere (IRI) 2016 model [*Bilitza et al.*, 2022].

In its position as the region where space plasma and neutral atmosphere overlaps, the ionosphere exhibits variability driven from both above and below. The aurora, for example, is produced when magnetospheric

plasma precipitates down magnetic field lines and collides with neutral particles there, exciting electrons in these neutrals, which then emit photons at different wavelengths depending on the energized neutral species.

2.2 Radio wave reflection and the Earth-ionosphere waveguide

This dissertation will focus on variability that impacts very-low-frequency (VLF) radio wave reflection from the lower ionosphere. The key parameters determining how this reflection occurs are the electron and neutral density profiles. In the absence of neutrals, an electromagnetic wave incident on the lower ionosphere will reflect at an altitude where the wave frequency ω is equal to the electron plasma frequency ω_p, given by *Parks* [2019]:

$$\omega_p^2 = \frac{n_e e^2}{m_e \epsilon_0} \tag{2.1}$$

where n_e is the electron density, e is the electron charge, m_e is the electron mass, and ϵ_0 is the electric permittivity. For the F region of the ionosphere, which is mostly ionized, knowledge of the electron density profile $n_e(z)$ is sufficient to estimate the reflection altitude of an incident wave. Waves with frequencies greater than the plasma frequency at the peak ionosphere electron density will not be reflected when normally incident on the ionosphere.

In the D region, however, significant neutral density plays a role in wave reflection. Because electrons collide frequently with neutrals while responding to the incident wave field, lower electron densities are able to reflect waves in the presence of neutrals than would be required without neutrals. Reflection of VLF waves with frequency ω in the lower ionosphere occurs when [*Ratcliffe*, 1959]:

$$\omega = \omega_r = \frac{\omega_p^2}{\nu_{en}} \tag{2.2}$$

where ω_p is the plasma frequency defined in equation 2.1, and ν_{en} is the electron-neutral collision frequency.

This modification results in VLF waves typically being reflected by the lower ionosphere around 65 to $75\,\mathrm{km}$ during the day, and 85 to $100\,\mathrm{km}$ at night. Because this reflection occurs well before the electron density peak at $\sim 300\,\mathrm{km}$, the lower ionosphere is often characterized by the Wait 2-parameter electron

density model [*Wait and Spies*, 1964]:

$$n_e(z) = 1.43 \times 10^{13} \exp(-0.15h') \exp((\beta - 0.15)(z - h')) \tag{2.3}$$

with associated electron collision frequency:

$$\nu_{en}(z) = 1.816 \times 10^{11} \exp(-0.15z) \tag{2.4}$$

where the electron density profile is parameterized by height h' and sharpness β. The electron-neutral collision frequency is not parameterized.

EM waves with frequency ω incident on the lower ionosphere from below therefore reflect at an altitude where:

$$\omega_{\text{reflected}} = \left\{ \begin{array}{ll} \omega = \omega_r = \frac{\omega_p^2}{\nu_{en}}, & \nu_{en} > \omega_p \\ \omega = \omega_p, & \nu_{en} < \omega_p \end{array} \right\} \tag{2.5}$$

The altitude profile of this reflection frequency for example day and night ionospheres, derived from a combination of the Wait ionosphere and neutral density models and the IRI model, are shown in figure 2.2; with $\omega_{\text{reflected}}$ shown by the highlighted traces.

The lower ionosphere then serves as the upper reflector in a waveguide bounded on the lower side by the conducting ground, called the Earth-ionosphere waveguide (EIWG). VLF waves launched by terrestrial or atmospheric sources may propagate long distances in this waveguide. These include navigation and communication transmitters, and lightning, which emits radiation across the entire electromagnetic spectrum. Lightning, its emissions, and methods to detect lightning using these will be discussed in section 2.4.

The ionosphere properties discussed above result in two reflection characteristics that are important for VLF propagation in the EIWG. First, reflection altitude for a given wave frequency is a function of both electron density and the background neutral atmosphere. Since the lower ionosphere contains far more neutrals than plasma, neutral collisions are very important for the reflection process. However, neutral collisions also result in energy being lost during the reflection, leading to attenuation of the wave at each reflection. Processes that increase electron density in the lower ionosphere lower the reflection altitude for

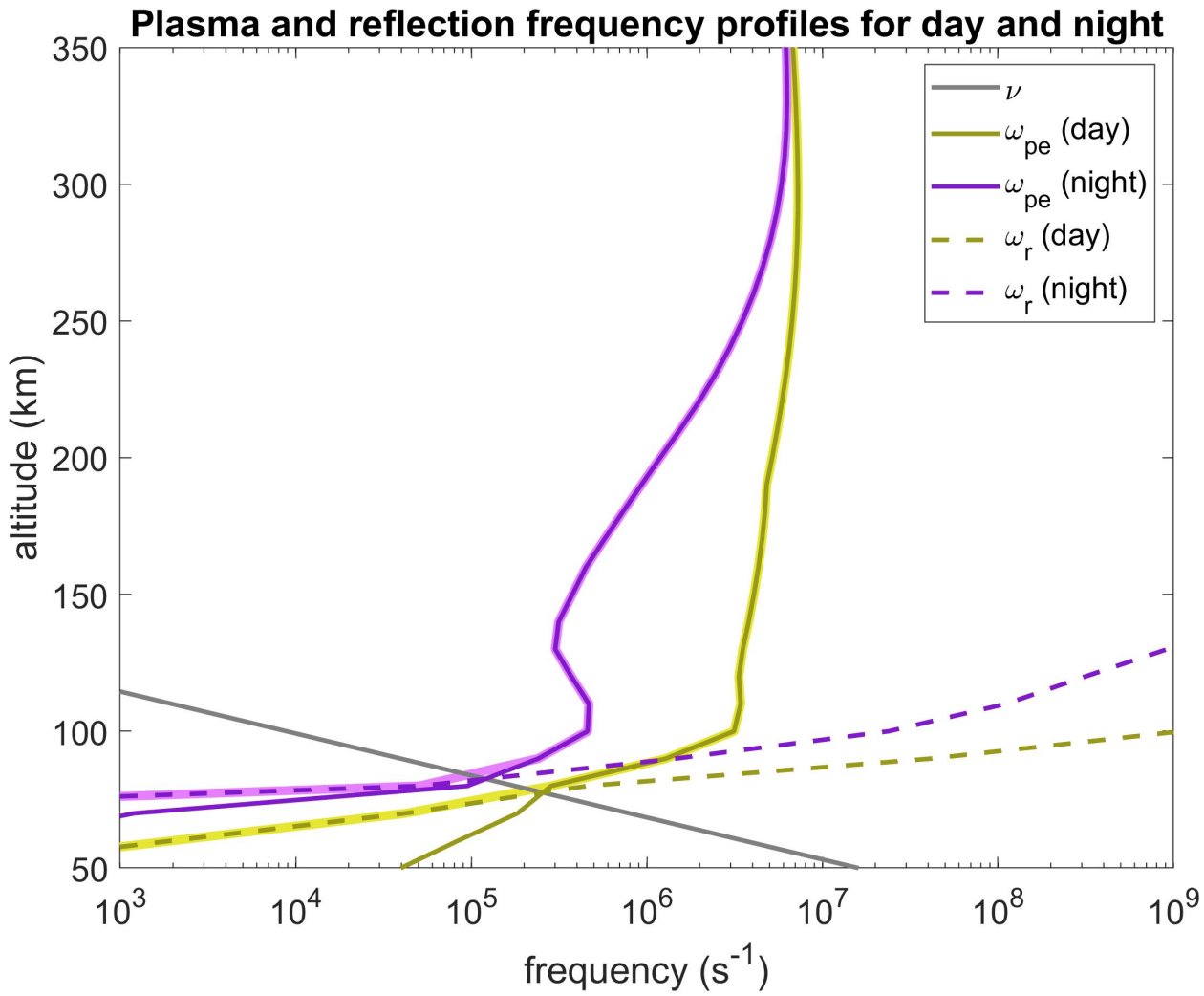

Figure 2.2: Reflected frequency resulting from plasma and electron-neutral collision frequencies. The highlighted traces shown profiles of $\omega_{\text{reflected}}$ determined from equation 2.5.

a given frequency, and the increased neutral density at lower altitudes gives rise to increased attenuation during reflections.

Second, reflection altitude for a given ionosphere and neutral profile is a function of frequency. Lower frequencies reflect at lower altitudes than higher frequencies, resulting in dispersion of broadband signals reflecting from the ionosphere. This dispersion can be significant over several reflections, and the amount of dispersion observed in a broadband wave packet depends on both propagation distance and ionosphere parameters. Lowering the reflection height necessarily increases the number of reflections needed for a wave to propagate long distances, increasing this dispersion over the path. Altering the sharpness of the ionosphere reflector also changes dispersion; a sharply-bounded reflector would result in each wave component reflecting at the same height, and therefore minimize dispersion; whereas a slowly increasing reflection height with frequency results in significant dispersion at each reflection.

In Chapters 3 and 4, we will study the impacts of space weather phenomena that lower the VLF reflection altitude, and how these processes may be investigated using VLF waves emitted by global lightning. The two space weather phenomena we will focus on are solar flares and energetic electron precipitation from the radiation belts, which are discussed in the introduction sections of the associated chapters.

2.3 The global electric circuit

The Earth-ionosphere waveguide (EIWG) is composed of the conductive lower ionosphere and ground, separated by the weakly conductive atmosphere; in this way, it resembles a leaky spherical capacitor [*Williams*, 2009; *Haldoupis et al.*, 2017]. This capacitor is home to a current system called the Global Electric Circuit (GEC), in which charge is driven upwards from the ground to the ionosphere, disperses horizontally there, and leaks downwards through the fair-weather atmosphere to the ground, where it may again disperse horizontally. The return current density is typically a few $\mathrm{pA\,m^{-2}}$.

The source current, which maintains the ionosphere at a 250 kV potential relative to the ground, was hypothesized by C. T. R. Wilson to be driven by global thunderstorm activity [*Wilson*, 1921]. This hypothesis was supported by measurements of vertical electric field over the oceans made on the research vessel Carnegie in 1910-29. These measurements, when heavily averaged, produced a curve showing the diurnal variation of the surface electric field that corresponds to the rotation of equatorial land masses into local afternoon; this curve is called the Carnegie curve. Whipple and Scrase argued in 1936 that, since thunderstorms were more frequent over land than over the oceans, and more likely to occur in local afternoon, global thunderstorms were almost certainly the driver of variations in the surface electric field, and hence the GEC [*Whipple and Scrase*, 1936].

The link between global thunderstorm activity and the GEC has been the subject of significant research effort over the past several decades. Here, we will describe prior work grouped into airborne measurements of the GEC return current, airborne measurements of thunderstorm currents, ground-based electric field measurements, and modeling efforts.

2.3.1 airborne measurements of the fair-weather return current

Several experimental campaigns have made measurements of the GEC return current density using stratospheric balloons. The Electrodynamics of the Middle Atmosphere (EMA) campaign in 1983-1984 measured the stratospheric vertical electric field and conductivity with a series of superpressure balloons launched from Christchurch, New Zealand. *Holzworth et al.* [1984] reported on the first two balloon flights (EMA 1 and 2), whose measurements were the first to show that (a) the GEC return current exibits short-term variability with time scales of tens of minutes to hours, and (b) despite the two balloons being separated by over 1000

km, the measured vertical electric fields agreed to within 20% for most of the flight. *Norville and Holzworth* [1987] presented results from EMA 7 and 8, confirming the earlier result that atmospheric electrical parameters were independent of balloon separation. The authors noted that the apparent spatial invariance of the GEC return current density, and that time variations in current density measured at any one balloon were most likely due to variations in global generators, not local electric disturbances. Therefore, a small number of instrumented balloon measurements should be sufficient to characterize the state of the global electrical environment, enabling the use of a geoelectric index to characterize the long-term variation in atmospheric electricity (see also *Holzworth and Volland* [1986]).

While the EMA campaign was successful in making simultaneous measurements of the GEC return current density at distant locations, it did not include an effort to measure the GEC source current. That was first attempted during the second Polar Patrol Balloon campaign, where two superpressure balloons launched from Syowa Station, Antarctica, measured vertical current density near 32 km, with 16 days of simultaneous measurements by both balloons [*Holzworth et al.*, 2005]. These measurements were compared with global lightning count rates from the World Wide Lightning Location Network (WWLLN). Although WWLLN detected only a small percentage of global lightning at the time [*Rodger et al.*, 2006], the authors found that the average vertical current density measured by the two balloons correlates with total lightning rate with a Pearson r-value of 0.46. However, the authors acknowledged both that WWLLN in its current state detected only a small percentage of global lightning, and that lightning rate was only a preliminary proxy for global thunderstorm activity.

2.3.2 airborne measurements of thunderstorm currents

Several experiments have also attempted to characterize the source current to the GEC by conducting instrumented overflights of thunderstorms with balloons or aircraft. *Thomas et al.* [2009] measured electric fields and conductivities above a thunderstorm in Brazil using a balloon carrying double Langmuir probe pairs. They measured an average vertical current density over the thunderstorm of $190\,\mathrm{pA\,m^{-2}}$ and a peak vertical current density of $365\,\mathrm{pA\,m^{-2}}$ due to the quasi-static charge of the thundercloud, corresponding to a quasi-DC $2.5\pm\,1.25\,\mathrm{A}$ contribution from the thunderstorm to the GEC over the 1-hour duration of the storm overflight. Additionally, they found that the total charge contributions of lightning transient currents

during the storm was insignificant compared to the quasi-static current.

Mach et al. [2009] reported on measurements of electric fields and conductivities made during 850 aircraft overflights of thunderstorms between 1993 and 2005, using electric field mills and Gerdien condenser probes. The authors measured a wide range of thunderstorm peak current densities, with the central 90% of the distribution ranging from about -0.13 to about $9.1\,\mathrm{nA\,m^{-2}}$. By assuming each thunderstorm is cynlindrically symmetric, produces a DC current during the overflight duration, and produces a vertical electric field that decays with radial distance from the center of the storm according to a median profile, the authors calculated a mean thunderstorm current contribution of $0.8\,\mathrm{A}$. The authors also found little correlation between estimated total thunderstorm current and lightning flash rate, and in particular found significant current contribution from storms with low or zero flash rate.

Mach et al. [2011] combined the overflight dataset with lightning detections from the Lightning Imaging Sensor (LIS) and Optical Transient Detector (OTD) satellite instruments (e.g. *Mach et al.* [2007]) to estimate the diurnal variation in the GEC generator current. By accounting for differences in land and ocean storm lightning rate and current contribution, and including electrified shower clouds (ESCs) as a current source, the authors were able to reconcile the UTC-averaged generator current with the diurnal variation in the Carnegie curve. Although this result is useful for constructing estimates of the thunderstorm generator circuit, it does not present a comparison of simultaneous source and return current of the GEC.

2.3.3 ground-based electric field measurements

Measurements of the fair-weather electric field at ground stations have also been compared with proxies of the GEC source current, with varying agreement. *Troshichev et al.* [2004] compared 10 days of vertical electric field measurements at the Vostok Antarctic station with simultaneous VLF lightning measurements made at Halley Bay, Antarctica, and found poor correlation in both the full time series and the mean diurnal variation of the data. The authors concluded that the vertical electric field in polar regions may be more influenced by magnetospheric effects than by lightning flashes.

Fang et al (in prep) compared vertical electric field measurements from Vostok and Utqiaġvik (Barrow) with several proxies of the GEC source current, derived from combinations of WWLLN lightning location data and IMERG precipitation data. They found that lightning rate alone correlated poorly with the vertical

electric field, in agreement with *Troshichev et al.* [2004], but that other proxies based on thunderstorm area, thunderstorm counts, and combined thunderstorm and precipitation area produced much better correlations with the vertical electric field.

2.4 The World Wide Lightning Location Network

The World Wide Lightning Location Network (WWLLN; pronounced "woolen") is a sensor network that detects lightning around the world by sensing very low frequency (VLF) radio waves emitted by the return stroke, the discharge of which accounts for the peak current in a lightning flash. These VLF atmospheric waves, or sferics, propagate long distances in the earth-ionosphere waveguide (EIWG) by reflection from the conducting lower ionosphere and ground. Although these waves are attenuated by electron-neutral collisions at each reflection, the attenuation coefficient, describing this attenuation as a function of propagation distance in the waveguide, is roughly constant for a significant portion of the VLF band, meaning the relative amplitudes of this portion of the VLF band will be preserved as the signal propagates in the waveguide [*Wait and Spies*, 1964].

WWLLN leverages long-range sferic propagation to detect global lightning with a relatively small number of receiving stations. There are currently about 80 WWLLN stations in operation around the world, as shown in the station map in figure 2.3. Each station searches for broadband sferics in the $6 - 18\,\mathrm{kHz}$ range, and determines the time of group arrival (TOGA) of each sferic by measuring the phase of each frequency component of the sferic and determining when the slope of this phase fit is zero [*Dowden et al.*, 2002]. Each station then sends the TOGA to a central server. By comparing the list of TOGAs from all stations, and considering the station locations and the sferic group velocity in the EIWG, we can find unique location solutions for lightning strokes.

An important aspect of WWLLN for this work is the types of data files that it can produce, and the subset of these that are typically archived. WWLLN produces several real-time or near-real-time data products, the most basic of which is the list of TOGAs and the station numbers that detected them, called Rfiles. The next is a list of lightning locations, called Afiles. With some additional processing, WWLLN also supplies this list of strokes with estimates of their VLF energy, which is related to return stroke peak current, called AEfiles. Alternatively, the Afiles can be supplied with a list of stations that contribute to this energy determination, and a list of those stations' uncalibrated VLF power estimates, called APfiles. Rfiles, Afiles, AEfiles, and APfiles are archived for the entire WWLLN time series.

However, there is an important set of files that are not typically archived, which are files containing wideband information. In order to detect sferics and make the TOGA determination, WWLLN records

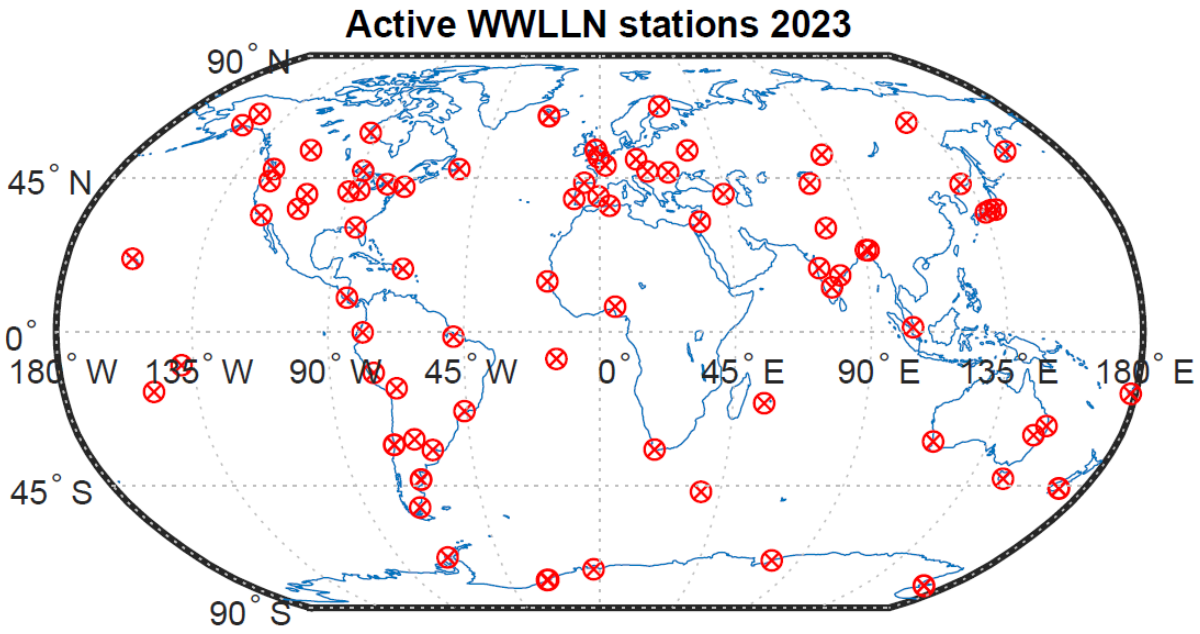

Figure 2.3: Map of active WWLLN stations in May 2023.

electric field information at either 48 or 96 kilosamples/second. Each 1-minute wideband file generated by a station sampling at 48 kilosamples/second is 11.5 MB , adding up to 17 GB per day, per station. In the process of checking sferic properties, stations also generate lists of sferics with timing, disperison and waveform information, called Sfiles. Sfiles are significantly smaller, at approximately 300 kB for 1-minute files, or 500 MB per day, per station. The full wideband electric field files and Sfiles are both temporarily saved on WWLLN stations, but are overwritten after a period of days to months, depending on the size of the station's local memory. Even if centralized storage were available for the roughly 5 petabytes of wideband data that WWLLN has generated over the years, transporting this data would be impractical; many stations are in remote locations, including Antarctic bases, and do not have access to sufficient internet bandwidth to transmit wideband files in real time.

Although WWLLN can detect lightning strokes all over the world, it only detects a moderate percentage of total lightning. This percentage of total lightning detected, called the detection efficiency, is an important parameter for assessing actual lightning rate based on detected lightning. Significant work has gone into quantifying the global, regional and time-varying detection efficiency [*Hutchins et al.*, 2012]. Because detection efficiency is variable, efforts to quantify thunderstorm activity using WWLLN typically rely on

spatial metrics of lightning regions, rather than simply lightning rate.

Chapter 3

VLF attenuation in the Earth-ionosphere waveguide during strong solar flares

This work was first published as Anderson et al. [2020]: Detection of VLF Attenuation in the Earth-Ionosphere Waveguide Caused by X-Class Solar Flares Using a Global Lightning Location Network, in Space Weather Journal. *It has been edited for clarity.*

Abstract: Solar flares, energetic particles and Earth-impacting coronal mass ejections enhance ionization in the lower ionosphere, inhibiting radio wave propagation in the Earth-ionosphere waveguide (EIWG). This enhanced ionization is observed locally by ionosondes and GPS/GNSS receivers, but spatial coverage of these observations is limited by receiver location. VLF propagation studies have previously been performed to assess the impact of space weather on the EIWG; however, these studies are typically limited by small numbers of fixed VLF transmitters and receivers, and observe only the region of the EIWG along propagation paths between transmitters and receivers. Here, we use global lightning as a VLF source, and an existing lightning detection network as a receiver. By mapping sferic propagation paths between lightning strokes and numerous network stations, and considering how this distribution of paths changes during solar events, we can identify attenuation regions in the EIWG caused by space weather. We describe the VLF response in the EIWG to two X-class solar flares, and compare mapped attenuation regions with those provided by the NOAA D-Region Absorption Prediction (D-RAP) model. The identified attenuation regions associated with these flares match the D-RAP-predicted regions well in both spatial extent and onset timing.

Measurements of VLF attenuation caused by solar flares can provide ground-truth confirmation of modeled attenuation, and can inform the detection efficiency of lightning location networks. This analysis also paves the way for real-time VLF attenuation mapping in the EIWG.

3.1 Introduction

Solar extreme ultraviolet (EUV) radiation generates most of Earth's ionosphere; and changes in the energetic particle and radiation output of the Sun can dramatically affect the Earth's ionosphere profile. Solar flares enhance ionization on short timescales, which significantly alter the ionosphere density profile throughout even the lowest layers (e.g. *Mitra* [1974]). This enhanced ionization in the D region can severely impact VLF radio wave propagation in the Earth-ionosphere waveguide (e.g. *Thomson and Clilverd* [2001]).

Mapping D-region ionosphere density at the global scale and with high time resolution is challenging and often involves using both ground-based radio propagation measurements and in-situ instrument campaigns. Ionosondes can produce accurate profiles of the E- and F-region ionosphere, but usually operate at frequencies well above the D-region plasma frequency; and GPS/GNSS TEC measurements are dominated by the much higher electron densities in the F region. Neither of these techniques can resolve D-region electron density and are effective only over regions near ground stations. Long-duration in situ measurements are difficult in this altitude band; the D region, at 50-80km altitude, is too high for stratospheric balloons, but thermosphere drag precludes long-duration orbital measurements there. VLF monitoring stations or networks can characterize propagation along transmitter-to-receiver paths; however, such networks operating today rely on a small number of transmitters and receivers (one to about 20 of each), and therefore suffer from poor spatial resolution of regional ionosphere features (e.g. *Chilton et al.* [1963]; *Crombie* [1965]; *Thomson and Clilverd* [2001]; *Bouderba et al.* [2016]). By using global lightning as a VLF source, we can detect regional VLF attenuation features with higher spatial and temporal resolution.

Previous work by other authors has shown that the Wait and Spies 2-parameter ionosphere (e.g. *Thomson* [1993]) can be inferred from measurements of lightning-launched sferics. *Cummer et al.* [1998] compared modeled and measured VLF and ELF sferics to infer nighttime D region electron density. *Jacobson et al.* [2007] demonstrated a method of lower-ionosphere sounding by opportunistic use of LF sferics launched by Narrow Bipolar events. *Jacobson et al.* [2010] reported on a steep-incidence VLF/LF sounding method

for studying transient, localized disturbances in the nighttime D region. *Carvalho et al.* [2017] presented a method to measure the ionospheric effective reflection height along 200-250km paths from VLF sferics launched by triggered lightning. *Gross et al.* [2018] used MSK transmitter stations as well as lightning sferics to infer ionosphere parameters from polarization of VLF signals, and *McCormick et al.* [2018] calculated ionosphere parameters using a comparison of simulated and measured sferics from several thunderstorms; both these techniques were presented for continent-scale regions, with possible extensions to global coverage in future work. A technique to provide a large-scale D region diagnostic using a small number of receivers to measure ELF sferic group velocity was presented by *Gołkowski et al.* [2018]. Thus far, a real-time global lower ionosphere monitor has not been demonstrated.

3.1.1 Lightning-generated sferics in the Earth-ionosphere waveguide

Cloud-to-ground lightning strokes typically discharge voltages of >1 MV over about 70 μ s, with peak current in the 10-100 kA range [*Uman and Krider*, 1982]. Each lightning stroke can be thought of as a short-lived transmission line antenna that emits broad-spectrum electromagnetic waves in a dipole-like radiation pattern. Radio waves with frequency ω are reflected by the lower ionosphere at an altitude where [*Ratcliffe*, 1959]:

$$\omega = \omega_r = \frac{\omega_p^2}{\nu_{en}} \tag{3.1}$$

where ν_{en} is the electron-neutral collision frequency, and ω_p is the electron plasma frequency:

$$\omega_p^2 = \frac{n_e e^2}{m_e \epsilon_0} \tag{3.2}$$

Where n_e is the electron number density, e is the electron charge, m_e is the mass of the electron and ϵ_0 is the permittivity of free space. The lower ionosphere acts as a reflector to radio waves in the ELF (3-3000Hz) and VLF (3-30kHz) frequency range. For a given frequency ω, the ionosphere can be thought of as a conductive spherical shell. Earth's surface, having electrical conductivity much greater than the intervening atmosphere, forms a conductive inner shell (e.g. *Siingh et al.* [2007]). Together, the lower ionosphere-atmosphere-Earth surface forms the Earth-ionosphere waveguide (EIWG), through which ELF and VLF

radio waves may propagate long distances. VLF waves launched by lightning strokes that propagate in the EIWG are called atmospheric waves, or sferics.

By detecting sferic wave packets that propagate large distances in the EIWG, we can observe global lightning with a relatively small number of observing stations. The World Wide Lightning Location Network (WWLLN) is a network of around 80 stations, distributed globally between ±80° latitude. Each station listens for sferics and reports the time of group arrival (TOGA) to a processing server; this server then combines TOGAs from each detecting station, and determines the location and time of the lightning stroke [*Dowden et al.*, 2002, 2008; *Hutchins et al.*, 2012].

3.1.2 Impact of solar flares on radio attenuation in the EIWG

Increased X-ray and EUV flux from solar flares has been shown to enhance ionization in the lower ionosphere (e.g. *Mitra* [1974]). This electron density enhancement at low altitudes lowers the reflection altitude of radio waves propagating in the EIWG, including lightning-launched sferics. Because of increased neutral particle density at lower altitudes, more energy is lost to electron-neutral collisions during radio wave reflection, and hence the wave is more attenuated while ionization in the lower ionosphere is enhanced.

Using near-real-time lightning location information from WWLLN, we can detect VLF attenuation in the EIWG caused by solar flares. By leveraging the spatial distribution of WWLLN network stations, we can approximately map VLF attenuation regions on timescales of about 10 minutes.

Detection of attenuation regions relies on differing timescales of solar flares and thunderstorms. Thunderstorm flash rate and geographic location typically vary on the order of hours [*Rakov and Uman*, 2003], while solar flare onset typically occurs in minutes and X-ray irradiance decays by an order of magnitude within about 1 hour [*Codrescu*, 2010]. Enhanced low-altitude ionization from solar flare activity will occur in a circular region centered on the Earth subsolar point [*Sauer and Wilkinson*, 2008; *Levine et al.*, 2019].

In addition to increased attenuation in the lower-frequency portion of the VLF band (<10 kHz), solar flares can cause enhancement of VLF signals in the higher-frequency VLF (>15 kHz) [*Volland*, 1995]. Such enhancements have been observed recently by *Wenzel et al.* [2016], which used four receivers in Europe and North America to measure amplitude and phase changes in VLF transmitter signals during M- and C-class flares; and *George et al.* [2019], which measured amplitude enhancements in the NPM 21.4 kHz

signal using a receiver at Scott Base, Antarctica, during several X-class solar flares. Since WWLLN uses the <16 kHz portion of VLF sferics to locate lightning strokes, it is sensitive to VLF attenuation caused by solar flares, but not enhancement in the higher-frequency VLF. The method presented here for detection of solar flare effects relies on the decrease of WWLLN detection efficiency near the subsolar point. This means the network, like other VLF lightning detection networks, is adversely affected by ionizing events from space, and these modifications to the network affect interpretations of lightning data. By studying the impact of solar flares on WWLLN lightning detection, we can improve our understanding of the effects of space weather on lightning detection networks and other technologies that rely on VLF reflection in the EIWG.

3.2 Methods

3.2.1 Global lightning stroke-to-station path distribution

WWLLN detects 0.5-1.5 million lightning strokes per day. These stroke locations are processed in real time, and by plotting great circle paths between stroke locations and the stations that detect each stroke, we can build a global stroke-to-station path distribution with a 10-minute timestep. A stroke-to-station path distribution for a 10-minute time window ending at time t is notated here as ss(t): a matrix of integers, where each element counts the number of stroke-to-station path crossings of the geographic area that element represents. We chose 1° latitude/longitude grid regions, such that ss(t) has 180×360 elements that cover the Earth and do not overlap. A sample stroke-station path distribution for a 10-minute time window is shown in Figure 3.1. Grid locations near high-quality WWLLN stations or active thunderstorm regions typically are traversed by 103-104 stroke-station paths every ten minutes, whereas locations near the poles or far from both WWLLN stations and active thunderstorms may be traversed by only a few stroke-station paths per day. Ground composition along the path is also important; since ice is much less conductive than dry land or ocean water, sferic propagation across the North pole is only possible via a few ocean routes, and propagation across Greenland and Antarctica is rare [*Westerlund and Reder*, 1973; *Barr et al.*, 2000].

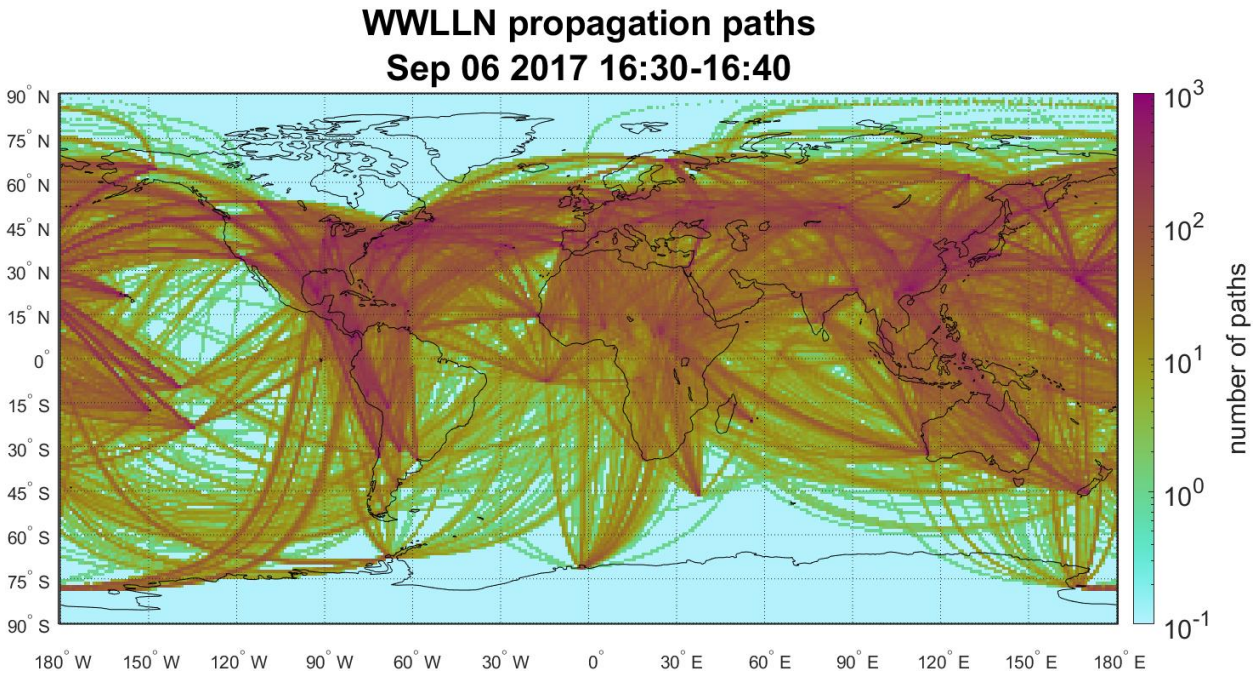

Figure 3.1: Sample WWLLN stroke-station path distribution for a 10-minute period. Stations contributing to this path distribution can be identified as points where many paths converge.

3.2.2 Model comparison: D-Region Absorption Prediction

We used the NOAA D-Region Absorption Prediction (D-RAP) model to inform our guess for VLF attenuation region geometry and timing [*Codrescu*, 2010]. The D-RAP model predicts HF radio attenuation using X-ray, electron and proton flux detected by the GOES constellation. Absorption at the subsolar point is calculated with an empirical relation between the highest affected frequency (HAF) and X-ray flux [*Sauer and Wilkinson*, 2008]:

$$\text{HAF (MHz)} = (65 + 10\log_{10}[\text{flux}(\text{W m}^{-2})])(\cos\chi)^{0.75}$$

Where χ is the solar zenith angle. For example, the HAF for an X9.3 flare (peak flux = 9.3×10^{-4} W m^{-2}) is about 35 MHz, decaying to 0 at the day/night terminator.

Although the D-RAP model addresses HF, not VLF, attenuation in the EIWG, it is still a useful comparison for a VLF attenuation analysis. HF and VLF attenuation in the EIWG during solar flares are both primarily caused by increased low-altitude ionization, and thereby increased electron-neutral collision frequency during wave reflection. Hence, both D-RAP and this VLF attenuation analysis are addressing changes in the lower ionosphere that should be approximately collocated and simultaneous.

3.2.3 Attenuation region visualization

We can gain insight into spatial and temporal variation in EIWG parameters by looking for changes in the global stroke-station path distribution through time. Energetic solar flares are particularly useful events to study, because of their predictable ionization enhancement in the lower ionosphere. With the assumption that far-field solar flare radiation can be treated as a planar radiation packet that is not appreciably distorted by Earth's magnetic field, nor does it contain fine structure relative to the size of the Earth, the pattern of enhanced ionization in the lower ionosphere is a circular region centered on the subsolar point [*Codrescu*, 2010; *Levine et al.*, 2019].

We can use the WWLLN stroke-station path distribution to look for VLF attenuation regions in the EIWG. First, we identify a background stroke-station path distribution at the time just before flare onset. Next, we measure the stroke-station path distribution immediately following flare onset, and calculate attenuation of stroke-station paths relative to the background distribution.

A background stroke-station path distribution is generated by taking the median of several consecutive stroke-station path distributions during a period of quiet solar activity. For any time t, a background distribution is constructed by taking the median of the previous hour's stroke-station path distributions,

$ss_b(t) = \text{Median}(ss(t_i)_{(i=1\rightarrow 6)})$

For a 1° latitude-longitude grid, ss_b is a 180 x 360 matrix, where each element is the median number of stroke-station paths crossing that grid location in the set of 10-minute time intervals ending at $t_i = (t - i10minutes)$. This time interval ranges from t-70 minutes to t-10 minutes; it is the hour preceding the 10-minute interval covered in ss(t). The 10-minute sample size is chosen because it is short enough to capture the onset of solar flare ionization, while still containing a large population of stroke-station paths. Additionally, WWLLN writes files containing stroke-station path and stroke power information every 10 minutes, so this is a convenient duration for a real-time analysis. A 1-hour median timescale was chosen to be shorter than typical mesoscale convective system lifetime [*Markowski and Richardson*, 2011], while acknowledging that individual thunderstorm flash rate can vary significantly minute-to-minute. A longer median timescale would reduce the median distribution's relevance to t as an immediate background, while a shorter median timescale would be more susceptible to varying thunderstorm flash rate.

Next, the 10-minute stroke-station path distribution immediately following a solar flare is compared to

the last hour's background stroke-station path distribution. Solar flare times are identified as peaks in GOES-13 X-ray irradiance data [*NCEI*, 2019]. VLF attenuation regions can be characterized by the logarithmic ratio of the current stroke-to-station path distribution to the median distribution for the previous hour:

$$A(t) = 10 \log_{10}(ss(t)/ss_b(t) \tag{3.3}$$

Note that $A(t)$ approximates VLF attenuation not by measuring the attenuation of VLF signals, i.e. sferics, but by comparing the number of received sferics transiting each grid location with the median number in the previous hour. Since we expect sferics transiting any grid location to be distributed in amplitude according to differences in source lightning parameters, path length, and waveguide characteristics over the path; and the lowest-amplitude sferics to be below the detection threshold of WWLLN stations; increasing VLF attenuation in a region of the waveguide should result in more of the lower-amplitude sferics transiting this region being attenuated below the detection threshold.

This measure of VLF attenuation is only accurately defined at matrix locations with sufficient counts in both matrices; it is most accurate at geographic locations near WWLLN stations and/or frequent thunderstorm regions. Additionally, we can validate attenuation region timing by computing the characteristic size of VLF attenuation region, and comparing the change of the size of this region with geostationary X-ray flux data [*NCEI*, 2019]. We compare X-ray flux recorded by the GOES-13 satellite with the size of the largest circular contour centered on the subsolar point within which the median logarithmic ratio of current to baseline stroke-station path traversals is less than -6. This threshold can be tuned to accept attenuation regions generated by lower-power flares, but is particularly useful for observing the onset timing of large attenuation regions and the radial change in stroke-station path attenuation within the region.

3.3 Results and Discussion

In this analysis, we considered the X9.3 and X8.2 solar flares of September 6 and 10, 2017. The solar events of this period are well-studied [*Yasyukevich et al.*, 2018; *Gary et al.*, 2018; *Qian et al.*, 2019; *Levine et al.*, 2019]. Sunspot group AR2673 produced several flares between late August and September 10, as well as solar energetic particles (SEPs) and coronal mass ejections (CMEs). Although these particle events had a

significant impact on the ionosphere, this was mostly contained in the polar caps, and solar flare ionization was still the primary effect on the lower ionosphere at low- to mid-latitudes. Among several powerful solar flares originating from this sunspot group, we chose the X9.3 flare at 12:10 UT on September 6, and the X8.2 flare at 16:10 UT on September 10, because radio propagation in the low-latitude ionosphere was expected to be nominal in the hours leading up to flare onset, as predicted by D-RAP.

Attenuation in the EIWG caused by the solar flares of September 6 and 10, 2017, was investigated by plotting the reduction in WWLLN stroke-station path crossings using a 10-minute timestep and 1-hour median baseline distribution. A comparison between the WWLLN response and the D-RAP predicted absorption is shown in Figure 3.2. A timing comparison between attenuation region radius and GOES-13 X-ray irradiance is shown in Figure 3.3. Finally, WWLLN stroke detection count rate for a sample 1000-km-radius region near the subsolar point during the September 10, 2017 flare is compared with GOES-13 X-ray irradiance in Figure 3.4.

Figure 3.2 shows comparisons between the D-RAP HAF maps and WWLLN-detected VLF attenuation. Figure times are chosen to reflect peak X-ray irradiance at flare onset; in the cases of both the September 6 and September 10 flares, maximum extent of both HF and VLF attenuation occurs within a few minutes of peak X-ray irradiance. The September 6 flare at around 12:00 UT is preceded by an X-class flare at around 9:00 UT, and solar energetic particles (SEPs) that enhance ionization near the poles. The HAF map at 12:10 UT shows the subsolar attenuation region produced by the solar flare, but also polar attenuation regions produced by earlier and ongoing particle effects. The September 10 flare at around 16:00 UT is not immediately preceded by other powerful flares or SEPs, but SEPs are launched at the same time as the flare and arrive at the Earth within an hour of the peak X-ray irradiance. These generate polar attenuation regions as well.

The VLF attenuation regions mapped using WWLLN stroke-station paths closely match D-RAP-predicted HF attenuation regions at flare onset. For both the September 6 and 10 flares considered, the extent of the stroke-station path reduction tracks that of 10MHz 1dB absorption predicted by D-RAP, with the exception of polar attenuations, which are not captured by the WWLLN stroke-station path difference. It should be noted here that both D-RAP-predicted HF attenuation and VLF attenuation mapped here extend nearly to the terminator, which is the expected limit for attenuation caused by solar EM radiation.

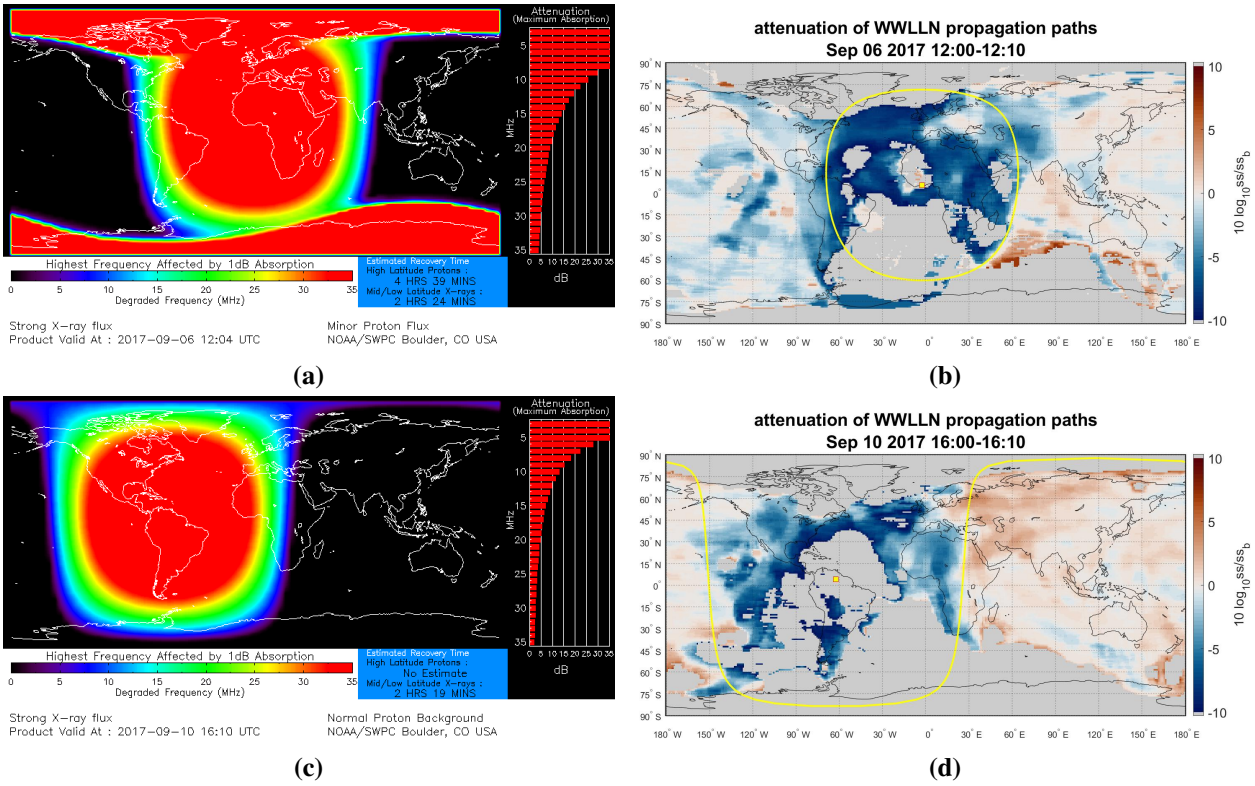

Figure 3.2: Comparison of DRAP with WWLLN path reduction.

Figure 3.3 shows that the onset timing of subsolar VLF attenuation regions occurs within this analysis' 10-minute time resolution of peak X-ray irradiance measured at GOES-13. X-ray irradiance peaked at 12:02 UT on September 6, 2017 and 16:03 UT on September 10; VLF-attenuation region radius on both these days peaked during the ten-minute intervals containing these times.

X-class flares have a significant impact on WWLLN detection of lightning strokes, as shown in Figure 3.4. Here, the WWLLN-detected occurrence rate of lightning strokes in 1000-km-radius region in the Caribbean is plotted for September 10, 2017. At the onset of the X8.2 flare at around 1600 UT, stroke rate drops 90% in a few minutes, and does not rise above the previous minimum recorded that day for several hours. We interpret this short-term decrease in stroke rate as sferics' inability to propagate out of the VLF attenuation region with sufficient power to be detected and used in lightning detection by WWLLN.

3.4 Summary

This analysis demonstrated the use of a global lightning detection network to map VLF attenuation in the EIWG caused by solar flares. Previous work has studied solar flare impact on low numbers of VLF transmitter-receiver paths, often only single paths (e.g. *Bouderba et al.* [2016]). More recently, lightning detection networks have been used in conjunction with fixed VLF transmitters to study multi-path flare effects [*Raulin et al.*, 2010], and small numbers of receivers have probed the D-region ionosphere using lightning sferics as a VLF signal [*Han and Cummer*, 2010; *McCormick et al.*, 2018]. This work demonstrates global VLF attenuation mapping using a lightning detection network, with the ability to resolve equatorial attenuation features associated with solar flares.

The VLF attenuation mapped in this study has significant implications for the detection efficiency of WWLLN and other VLF lightning detection networks. WWLLN requires a minimum of 5 stations to detect a sferic in order to locate a lightning stroke; therefore, if multiple VLF propagation paths between a thunderstorm and WWLLN stations are not viable due to increased low-altitude ionization, and the total number of WWLLN stations able to detect strokes from that thunderstorm falls below 5, WWLLN will be unable to detect those strokes. Strokes occurring inside VLF attenuation regions during X-class solar flares are unlikely to be detected, as demonstrated in Figure 3.4.

There are several shortcomings of this analysis that will be addressed in future work. First, the flares

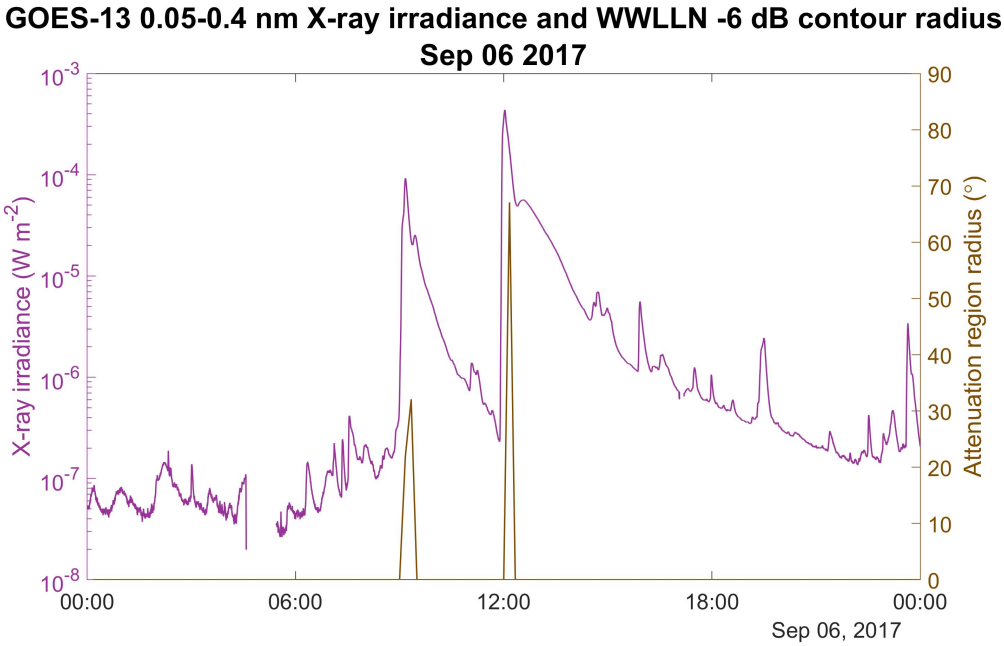

(a)

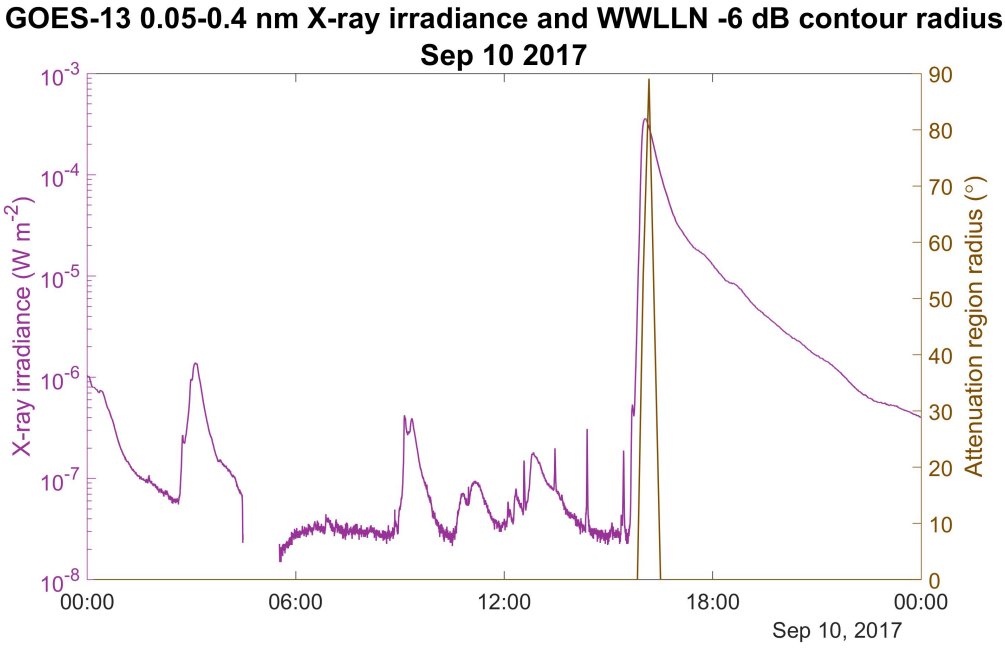

(b)

Figure 3.3: Comparison of VLF attenuation region radius (brown, right axis) and GOES-13 0.05- to 0.4-nm X-ray irradiance (purple, right axis), for 6 September (top) and 10 September (bottom). The blue curve is the radius, in degrees, of the largest circular subsolar region inside which the median log ratio of current to baseline stroke-station path traversals is at most -6. These regions are plotted as the yellow circles in Figures 3.2b and 3.2d, which correspond to the maxima of the brown curves in the upper and lower panels in this figure, respectively.

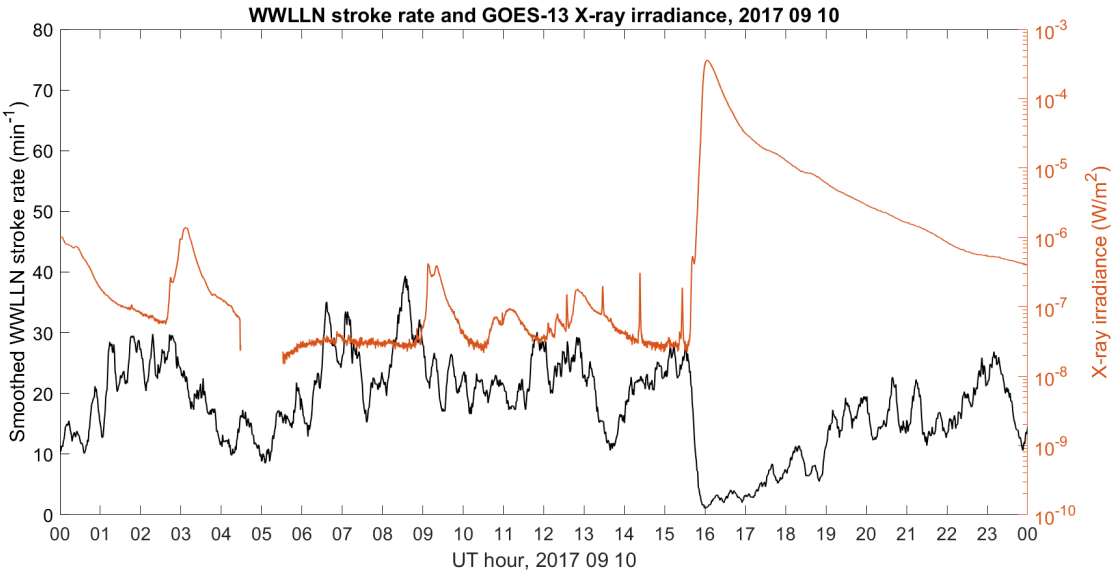

Figure 3.4: Comparison of WWLLN-detected lightning stroke count rate inside a near-subsolar region (black, left axis) and GOES-13 0.05- to 0.4-nm X-ray irradiance (orange, right axis). The region considered here is a 1,000-km radius area near the subsolar point and is plotted as a yellow circle in Figure 3.2d. WWLLN detections of lightning strokes occurring within this region are plotted as the black curve. Stroke rate has been smoothed with a 10-min moving average. At the onset of the X8.2 flare at around 16:00 UT, WWLLN stroke rate inside this near-subsolar region drops an order of magnitude from around 25 to 2 strokes per minute.

considered here are relatively "clean" and temporally isolated events; that is, there are no flares of any significant magnitude preceding or following them by less than 1 hour, nor any other obvious sources of lower-ionosphere ionization enhancement [*NCEI*, 2019]. Additionally, they are both very powerful, X-class events. As such, we expect them to produce a predictable and significant attenuation region on the day side lower ionosphere [*Sauer and Wilkinson*, 2008]. Less powerful events may not produce attenuation that is as evident in a WWLLN stroke-station path analysis. So far, analyses of recent C-class flares (2 orders of magnitude less irradiance than X-class) have not shown an obvious attenuation effect on WWLLN sferics. Future work should address the lower limit on flare irradiance that is detectable as a single-event attenuation region, and perhaps the lower limit that is detectable in a superposed epoch analysis.

Second, this analysis relies on a 1-hour averaging threshold, chosen to fall between the timescales of flare onset (1-10 minutes) and thunderstorm lifetime (hours) [*Rakov and Uman*, 2003]. This threshold is effective at detecting attenuation produced at flare onset, especially when the hour preceding flare onset has relatively constant, low levels of X-ray irradiance. As soon as the flare occurs, however, the 1-hour average of stroke-station path crossings is disturbed, and as such the ionosphere recovery after peak flare irradiance cannot be effectively characterized by stroke-station path crossing differences. This could potentially be addressed with multiple averaging thresholds with different periods, or with the development of a no-flare path distribution prediction, which guesses the stroke-station path crossing distribution based on the pre-flare distribution of stroke-station paths and lightning, and a predicted lightning distribution that accounts for lightning strokes inside the attenuation region.

Finally, this work takes advantage of the globally-distributed nature of lightning strokes and WWLLN stations to provide adequate stroke-station path coverage over regions of interest. Unfortunately, sferic propagation is sparse over polar regions, due in part to the concentration of global lightning near the equator and mid-latitudes. Without increasing the number of stations in polar regions, this technique will be far more effective at characterizing equatorial VLF attenuation regions caused by solar flares than polar events associated with SEPs and CMEs.

In addition to addressing the shortcomings detailed above, this work has the potential to be developed into a real-time monitor of VLF attenuation in the EIWG. The WWLLN files needed for this analysis are available every 10 minutes, and the software used here runs in less than that time.

Chapter 4

Resolving energetic electron precipitation signatures in the mesosphere-lower thermosphere using sferic dispersion statistics

4.1 Introduction

The Earth's Van Allen radiation belts are roughly toroidal regions of high-energy plasma between $L = 1.1 - 2$ and $L = 3 - 10$. Radiation belt electrons typically have energies in the hundreds keV to tens of MeV [*Jaynes and Usanova*, 2020], presenting significant hazard to spacecraft or astronauts transiting through the radiation belts. These electron populations are maintained by a balance of source and loss mechanisms, and the outer belt in particular has been observed to be highly dynamic, with electron lifetimes there often under one day [*Millan and Thorne*, 2007]. Some outer belt loss is attributed to outward radial diffusion or inward movement of the magnetopause, resulting in electrons drifting from closed to open field lines and being lost to the magnetopause; but the majority of loss processes result in electron precipitation into the upper atmosphere and scattering loss there.

Understanding the dynamics of radiation belt precipitation is important not only for assessing risk to humans and infrastructure inside the radiation belts, but also to quantify the impact of energetic electron precipitation (EEP) on atmospheric chemistry. EEP has been shown to generate odd-nitrogen (NO_x) and odd-hydrogen (HO_x) in the mesosphere and upper stratosphere; both of which catalytically destroy ozone there. Further, polar upper stratospheric NO_x may persist for many months and be circulated downward in the winter polar vortex, allowing it to reduce ozone concentration in the middle and lower stratosphere as well. The specific impact of EEP on Earth's climate is still a matter of debate [*Andersson et al.*, 2014; *Arsenovic et al.*, 2016; *Meraner and Schmidt*, 2018], but as the polar stratosphere represents an outsized uncertainty in whole-atmosphere circulation models [*Sinnhuber et al.*, 2012], quantifying temporal, spatial, and energy distribution of EEP is important in order to characterize the relationship between polar atmospheric chemical dynamics, solar forcing, and surface climate.

Energetic electron precipitation can be measured directly with in-situ particle detectors, or remotely via a number of means. The standard for direct particle measurements has long been the US NOAA Polar Operational Environmental Satellites (POES) and EU Meteorologial Operational Satellites (MetOp), two series of satellites in sun-synchronous orbits around 800 km altitude, which each carry identical Space Environment Monitor (SEM-2) instrument packages, among other instruments. The SEM-2 package includes two suites of particle detectors, the omnidirectional Total Energy Detector (TED), and the Medium Energy Proton and Electron Detector (MEPED). MEPED consists of two particle telescopes, oriented at 0- and 90-degrees to

the local zenith, which detect electrons with trajectories within 30° of the telescope look direction in several integral energy bands.

Much work has been devoted to estimating the full energy and pitch angle spectra of electrons based on MEPED measurements. *Nesse Tyssøy et al.* [2016] demonstrated methods to estimate the pitch angle distribution between the bands measured by the MEPED telescopes, and *Nesse Tyssøy et al.* [2022] compared different methods for estimating the total ionization rate in the mesosphere/lower thermosphere based on MEPED measurements. Several authors have presented methods to correct for proton contamination and long-term sensor degradation [*Yando et al.*, 2011; *Lam et al.*, 2010; *Peck et al.*, 2015; *Rodger et al.*, 2010a,b] and have created new datasets that attempt to circumvent this contamination [*Asikainen and Ruopsa*, 2019; *Nesse Tyssøy et al.*, 2016; *Pettit et al.*, 2019, 2021; *van de Kamp et al.*, 2016, 2018] , enhancing the accuracy of MEPED measurements for use as a "ground truth" comparison with models and remote sensing estimates. However, the sparse spatial distribution of the POES/MetOp spacecraft limit their usefulness in quantifying the spatial extent and structure of specific precipitation events.

A range of techniques have been used to estimate the spatial, temporal and energy distribution of EEP. Beyond POES, in-situ X-ray detectors on balloons *Millan et al.* [2007] and particle detectors on spacecraft (e.g. FIREBIRD II [*Capannolo et al.*, 2019, 2021]) provide precipitating energy spectra above and below the mesosphere, but suffer the same spatial limitations of any sparse in-situ measurement scheme. Remote-sensing means to estimate EEP flux in the mesosphere span the electromagnetic radiation spectrum, from X-ray bremsstrahlung sensing or imaging, to VHF incoherent scatter radar profiling, HF SuperDARN backscatter *Bland et al.* [2021, 2022], and subionospheric VLF propagation studies. Such methods typically compare remote sensing measurements of EEP with either spacecraft particle data from POES MEPED or another in-situ instrument, or geomagnetic substorm indices such as the D_{st} and A indices. A review of these methods can be found in *Jaynes and Usanova* [2020]; impacts of EEP on the upper atmosphere, and methods for sensing these impacts, are discussed in *Marshall and Cully* [2020] and *Sinnhuber and Funke* [2020].

Subionospheric VLF techniques measure properties of VLF radio waves propagating in the Earth-ionosphere waveguide. The most famous example of subionospheric VLF propagation analysis used in space physics is the Antarctic-Arctic Radiation-Belt (Dynamic) Deposition - VLF Atmospheric Research

Konsortia (AARDDVARK), a network of about 20 receivers distributed globally that measure the amplitude and phase of narrowband VLF transmitter signals *Clilverd et al.* [2009]. Because the transmitter carrier signals are nominally constant in time, they are well-characterized sources, and subtle variations in the received signals can be used to infer changes in waveguide conditions with high time resolution. Each transmitter-receiver pair forms a 1D great circle propagation path, and the received signal represents the propagation conditions of the Earth-ionosphere waveguide integrated along this path.

Despite the global coverage of VLF transmitters and AARDDVARK receivers, the network still suffers from widely varying spatial resolution. Regional networks, such as the ABOVE and AVID have been deployed in attempts to resolve smaller spatial-scale structures in EEP. These networks used arrays of receiver stations deployed in Canada and/or the northern United States to achieve denser propagation path coverage over this region, enabling studies of smaller-scale EEP events such as electron microbursts (e.g. *Anderson et al.* [2017]). For studies of hemisphere-scale precipitation, however, subionospheric VLF measurements would benefit from increased propagation path density over the entire auroral and subauroral regions.

Such coverage may be achieved by utilizing existing VLF lightning detection networks. These networks locate lightning by detecting broadband VLF atmospheric wave pulses, or "sferics", with multiple stations. By comparing the timing of sferic arrivals at each station, a unique solution for the source lightning stroke location can be found. Similar to transmitter-receiver pairs in the aforementioned VLF transmitter-receiver networks, each stroke-station pair forms a propagation path, over which the integrated waveguide propagation conditions impact the sferic received at the station.

Unlike VLF transmitter-receiver networks, lightning location networks use transient sources that occur over predictable but inconstant regions of the Earth. This source variability results in two potential advantages for using lightning as a probe signal for resolving EEP signatures at higher spatial resolution. First, the global distribution of lightning covers more of the Earth than that of VLF transmitters, resulting in an overall denser propagation path distribution for a typical lightning daily lightning distribution. Second, lightning tends to occur in spatial and temporal clusters–thunderstorms–in which tens to thousands of lightning strokes may occur within the span of tens of minutes and an area of tens or hundreds of kilometers across. The sferics launched by a single thunderstorm, then, generate a swath of propagation paths to each detecting station, resulting in far greater spatial resolution perpendicular to the propagation direction than a

single VLF transmitter-receiver pair would provide.

Prior efforts by several authors have used lightning sferics to study ionosphere variability. *Shao et al.* [2013] and *Lay et al.* [2014] demonstrated a technique for estimating the D-region electron density profile at one-hop sky wave reflection location by comparing a model of the ground wave and first sky wave with the recieved pulses, and showed that this technique could be used to measure the reduction in electron density over thunderstorms when these storms coincided with the skywave reflection point. *Cummer et al.* [1998] modeled received sferics over >1000 km paths under different waveguide conditions, and successfully extracted nighttime D-region height from measured sferics by comparison to these models. *McCormick et al.* [2018] compared measured sferics to simulations and estimated amplitude and phase changes due to solar flare ionization. Although successful at accurately determining ionosphere characteristics using sferics, these analyses were greatly constrained by spatial requirements. The technique presented by Shao and Lay required the presence of thunderstorms within about 1000 km of the receivers, and only estimated ionosphere parameters at the location of the first sky wave reflection. *Cummer et al.* [1998] and *McCormick et al.* [2018] do not locate their ionosphere parameters at all, instead presenting the best-fit parameters integrated over the entire propagation path.

In this chapter, we present a new technique for resolving spatial signatures of energetic electron precipitation in the mesosphere-lower thermosphere using sferics detected by a lightning detection network. We examine the lower ionosphere information contained in sferics; develop a method for mapping sferic information to spatial and temporal bins; and compare variations in sferic dispersion with in-situ measurements of EEP by POES-MEPED.

4.2 Methods

The chapter utilizes an extension of the technique presented in Chapter 3. That work used the stroke-to-station path distribution, obtainable from lightning locations and the list of receivers that contributed to each stroke's location. Very powerful solar flares cause such enhanced ionization in the lower dayside ionosphere that many sferics are unable to propagate through this portion of the waveguide, so the waveguide attenuation region is clearly visible as a rapid decrease in the number of stroke-to-station paths transiting the subsolar region.

Except for the highest-flux events, energetic electron precipitation (EEP) is unlikely to cause such a reliable signal in the path distribution. Although EEP occurs in a predictable latitude range corresponding to the outer radiation belt L shells ($L \approx 2.5 - 7$), the local time location and extent of precipitation regions is unpredictable. Additionally, because WWLLN has few high-latitude stations, and lightning tends to occur most frequently at low- and mid-latitudes, the WWLLN stroke-to-station path distribution does not always cover most of the auroral and subauroral regions with an adequate number of paths for temporal statistics of the path distribution to be effective. The combination of these factors means that sensing EEP regions with WWLLN requires a technique using fewer propagation paths to sample smaller and weaker regional effects, compared to sensing X-class solar flares.

We approach these difficulties by utilizing the waveform information contained in WWLLN sferics. Each sferic exhibits dispersion–higher-frequency components arrive before lower-frequency components–and this dispersion is related to parameters of the Earth-ionosphere waveguide (EIWG), particularly the ionosphere effective height, which is lowered by EEP ionization. This section describes the technique used to integrate sferic waveform information into the spatiotemporal statistics presented in the previous chapter, as well as a method to qualitatively compare these statistics with satellite measurements of EEP.

4.2.1 WWLLN stroke-to-station path distribution

The World Wide Lightning Location Network (WWLLN) is a network of over 100 VLF receiver stations distributed around the world. WWLLN locates lightning using the time of group arrival (TOGA) technique: each station records the arrival times of atmospheric waves, or "sferics"; by comparing the arrival times recorded at each station with speed of VLF propagation in the Earth-ionosphere waveguide, a central server

can identify unique locations for lightning strokes detected by at least five stations. In recent years, WWLLN has typically located between 0.5-1.5 million lightning strokes per day.

Each lightning stroke-station pair forms a great circle path, along which the lightning sferic propagates to the station. Since each lightning stroke located by WWLLN is detected by at least five stations, daily lightning produces a distribution of > 2.5 million transient stroke-to-station paths. Each received sferic samples properties of the Earth-ionosphere waveguide integrated along the entire propagation path.

Subionospheric VLF transmitter-receiver networks, such as AARDDVARK , ABOVE , and AVID measure the amplitude and phase of narrowband VLF signals emitted by high-power transmitters used for long-distance communication purposes. As such, these networks sample waveguide conditions continuously on relatively small number of fixed propagation paths. In contrast, WWLLN sferic propagation paths are transient, and determined by the locations of WWLLN lightning stations and global lightning.

4.2.2 Perpendicularity of path azimuths

Since each received sferic contains information about waveguide conditions integrated along the entire path, a perturbation in the waveguide (e.g. an ionospheric irregularity) somewhere along the path cannot be located in the along-path direction. In order to locate a waveguide perturbation in both horizontal dimensions, the perturbation must be measured on multiple, non-parallel paths. The spatial and temporal resolution of any subionospheric VLF network covering a given region of the Earth-ionosphere waveguide is therefore determined by (a) the density of network paths covering the region, (b) the degree to which these paths are perpendicular, and (c) the cadence at which these paths can be sampled, or the time variation of (a) and (b) if the path distribution is transient, and (d) the number of samples required to differentiate a perturbed signal from noise.

The spatial and temporal resolution of transmitter-receiver networks is simple to quantify: since the path distribution is fixed, the path segments surrounding each path intersection form a "pixel" in the network's imaging capability. Computing these pixel sizes and locations for N paths scales as $O(N^2)$, which is not a problem for a fixed path distribution like that from a transmitter-receiver network with tens or hundreds of paths. WWLLN's transient stroke-station path network, however, requires that this calculation be made for each time period over which paths are binned, resulting in a calculation scaling as $O(B_t(N/B_t)^2 = N^2/B_t)$,

where B_t is the number of time bins. For time bins large enough to accumulate significant numbers of paths over regions of interest, this calculation quickly becomes untenable.

In order to estimate the spatial coverage of a distribution of transient propagation paths, we define the perpendicularity $P(\Theta)$ of a set of azimuths $\Theta = \{\theta_j\}_{j=1}^{N}$ with N members:

$$P(\Theta) = 1 - \frac{1}{N}\left|\sum_{j=1}^{N} \exp(i2\theta_j)\right| \tag{4.1}$$

Note that the perpendicularity of a set of azimuths is equal to the circular variance [*Fisher*, 1995] of the set of doubled azimuths. Perpendicularity varies between 0, when all azimuths in the set are parallel or antiparallel; and 1, where the set of azimuths consists of pairs of perpendicular azimuths.

Perpendicularity can also be used as a weighting function to approximate the number of perpendicular paths in a distribution. For a set of azimuths Θ made up of n_1 elements of azimuth $\theta_1 = 0$ or π, and $n_2 < n_1$ elements of azimuth $\theta_2 = \pm\pi/2$, the resulting perpendicularity is:

$$\begin{aligned} P(\Theta) &= 1 - \frac{1}{n_1 + n_2}\left|\sum_{1}^{n_1} \exp(i2\theta_1) + \sum_{1}^{n_2} \exp(i2\theta_2)\right| \\ &= 1 - \frac{|n_1 - n_2|}{n_1 + n_2} \\ &= \frac{n_1 + n_2}{n_1 + n_2} - \frac{|n_1 - n_2|}{n_1 + n_2} \\ &= \frac{2n_2}{n_1 + n_2} \\ &= \frac{2n_2}{N} \end{aligned}$$

For this set of perpendicular paths, the total number of paths $N = n_1 + n_2$ multiplied by the perpendicularity of the azimuths P gives the number paths in perpendicular pairs:

$$\frac{NP}{2} = n_2 \leq n_1 \tag{4.2}$$

Thus, perpendicularity can be used to find the number of perpendicular pairs in a path distribution comprised of two perpendicular components. For realistic path distributions with multiple non-perpendicular

components, perpendicularity can be used to estimate the directionality of path coverage of a region, which can be compared to a threshold based on a theoretical perpendicular distribution. In this work, we use the threshold $NP/2 = 1$ to determine whether a grid location has been traversed by a sufficient number of paths with sufficiently different azimuths to be included in our analysis, which has the effect of eliminating grid locations traversed by paths associated with only one storm-station pair.

4.2.3 Sferic dispersion

Each WWLLN station detects VLF sferics as broadband spikes in amplitude with positive dispersion, i.e. lower frequencies at advanced phase relative to higher frequencies. An arrival time can be assigned by determining the slope of phase ϕ as a function of frequency ω; the time t_0 when $\frac{d\phi(\omega)}{d\omega} = 0$ evaluated over the WWLLN VLF frequency band is called the time of group arrival, or TOGA. An example sferic received by a WWLLN station is shown in Figure 4.1.

A broadband signal propagating in a 1D stratified Earth-ionosphere waveguide will experience dispersion arising from several effects: structural dispersion of frequency-dependent waveguide modes; frequency-dependent reflection altitude, resulting from the altitude variation of plasma frequency and electron-neutral collision frequency (see equation 2.2); and propagation through the dispersive matter, that is, frequency-dependent phase velocity within the waveguide dielectric medium. The latter effects are eliminated by approximating the waveguide upper and lower boundaries as perfect conductors ($\sigma = \inf$), and the intervening atmosphere as a perfect dielectric ($\sigma = 0$), removing the frequency dependence of reflection altitude and the dispersive effects of the dielectric. If the curvature of the waveguide is small relative to the propagation distance, the sferic dispersion is found from the parallel-plate dispersion relation [*Zangwill*, 2013]:

$$k^2 = \frac{\omega^2 - \omega_0^2}{c^2} \tag{4.3}$$

where ω_0 is the waveguide angular cutoff frequency, related to cutoff frequency f_c and waveguide height h:

$$\frac{\omega_0}{2\pi} = f_c = \frac{c}{2h} \tag{4.4}$$

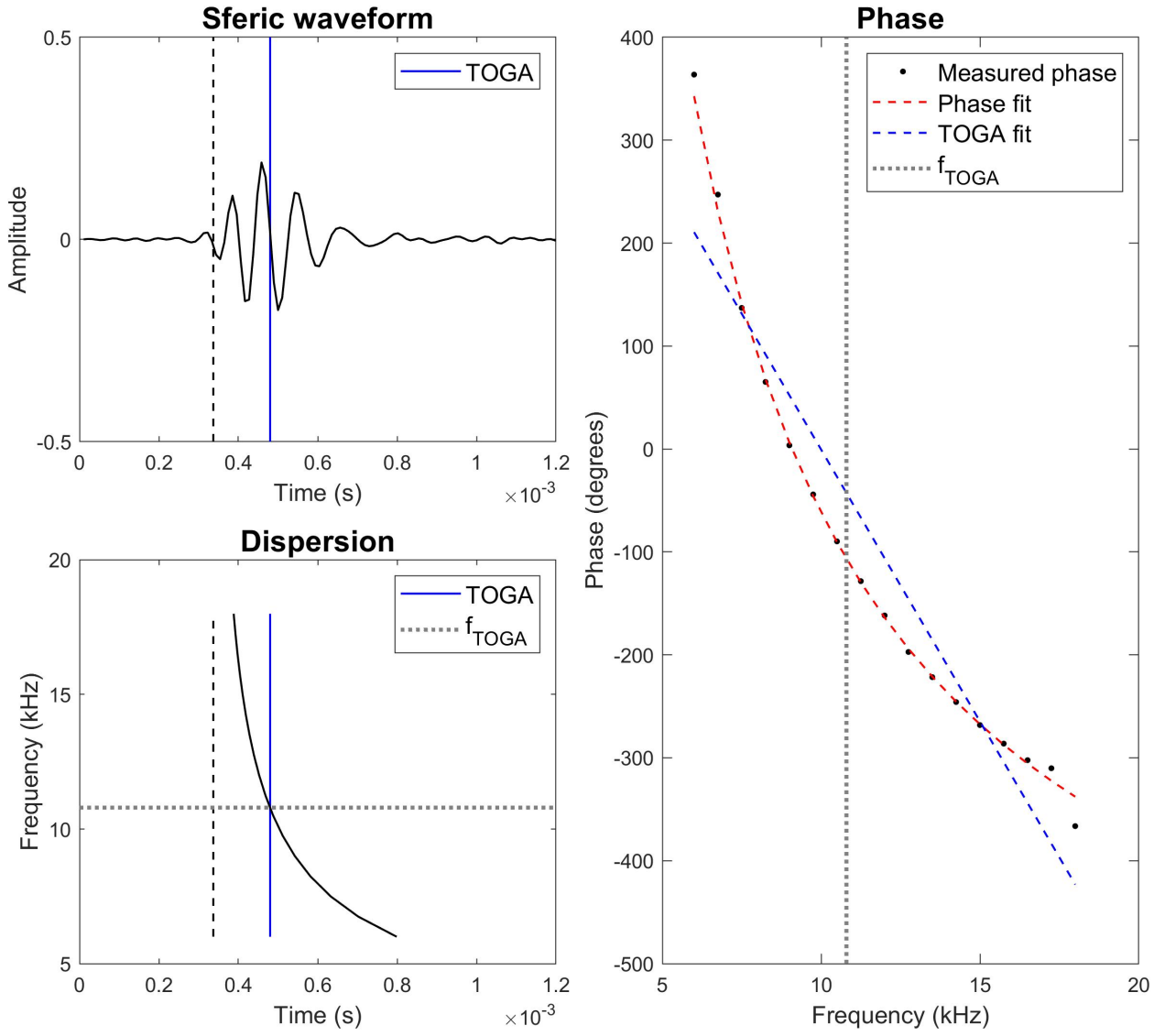

Figure 4.1: An example sferic detected by the Seattle WWLLN station. The time of group arrival (TOGA) is marked by the blue line in the left two panels, and is defined as the arrival time of the frequency at which the slopes of the phase fit (equation 4.9) and a linear phase fit over the WWLLN VLF frequency band are equal.

The waveguide cutoff frequency is the lowest frequency at which waves can propagate in the EIWG; at lower frequencies, half the wavelength is too long to fit in the waveguide. Previous estimates of the ionosphere cutoff frequency estimate it to be $f_c = 1.67\,\mathrm{kHz}$ in the nightside ionosphere [*Cummer*, 2000; *Dowden et al.*, 2002; *Toledo-Redondo et al.*, 2012], corresponding to an ionosphere effective height around $h = 90\,\mathrm{km}$, in agreement with a typical nightside height in Wait's classic 2-parameter ionosphere [*Wait and Spies*, 1964]. Studies of the D-region ionosphere response to various drivers often measure this height under various ionosphere conditions, and report dayside ionosphere height of around $65{-}75\,\mathrm{km}$ and nightside height around $85{-}95\,\mathrm{km}$ [*Cummer et al.*, 1998; *Marshall and Inan*, 2010; *Gołkowski et al.*, 2018; *McCormick et al.*, 2018].

The phase ϕ of each frequency component ω of a sferic is given by [*Dowden et al.*, 2002]:

$$\phi(\omega) = \omega t + \phi_0 - k(\omega) r \tag{4.5}$$

where t is time, ϕ_0 is the initial phase at $t = 0$, k is the frequency-dependent wavenumber, and r is the propagation distance. We can approximate k using a Taylor series expansion:

$$\begin{aligned} k &= \sqrt{\frac{\omega^2 - \omega_0^2}{c^2}} \\ &= \frac{\omega}{c}\sqrt{1 - \frac{\omega_0^2}{\omega^2}} \\ &\approx \frac{\omega}{c}\left(1 - \frac{1}{2}\frac{\omega_0^2}{\omega^2}\right) \\ k &\approx \frac{\omega}{c} - \frac{\omega_0^2}{2c\omega} \end{aligned} \tag{4.6}$$

Inserting 4.6 into 4.5 yields:

$$\begin{aligned} \phi(\omega) &= \omega t + \phi_0 - \left(\frac{\omega}{c} - \frac{\omega_0^2}{2c\omega}\right) r \\ \phi(\omega) &= \omega\left(t - \frac{r}{c}\right) + \phi_0 + \frac{\omega_0^2 r}{2c}\frac{1}{\omega} \end{aligned} \tag{4.7}$$

The first term of equation 4.7 accounts for travel time in the waveguide, where the wave propagates at speed c, and the second term gives the frequency-independent phase offset that may be introduced during wave emission–in this case, the lightning return stroke. The third term accounts for properties of the waveguide, in particular ω_0, the waveguide cutoff frequency.

The cutoff frequency determines the sferic's dispersion, i.e. difference in arrival times of different frequency components, for a given distance. For a known propagation distance r, the cutoff frequency ω_0 determines the dispersion of a sferic propagating in the waveguide. For arbitrary high- and low-frequency components of the sferic ω_H and ω_L, the group time difference $\Delta t_g(\omega_H, \omega_L)$ between these components' arrival at the receiver is:

$$\begin{aligned} t_g(\omega) &= t - \frac{d\phi}{d\omega} = \frac{r}{c} + \frac{\omega_0^2 r}{2c}\frac{1}{\omega^2} \\ \Delta t_g(\omega_H, \omega_L) &= \frac{\omega_0^2 r}{2c}\left(\frac{1}{\omega_L^2} - \frac{1}{\omega_H^2}\right) \end{aligned}$$

and the average group time difference per unit propagation distance is:

$$\frac{\Delta t_g(\omega_H, \omega_L)}{r} = \frac{\omega_0^2}{2c}\left(\frac{1}{\omega_L^2} - \frac{1}{\omega_H^2}\right) \tag{4.8}$$

Since light speed c, the propagation distance r, and the arbitrary high- and low-frequencies ω_H and ω_L are known, the group time difference for a dispersed broadband sferic propagating in a 1D stratified, horizontally homogeneous waveguide yields the cutoff frequency ω_0 of the waveguide.

The cutoff frequency can be estimated by fitting the function (4.7) to received phase data, as in the right panel of Figure 4.1. The WWLLN sferic detection algorithm fits a hyperbolic function to each sferic candidate, of the form:

$$\phi(\omega) = a_1\omega + a_2 + a_3/\omega \tag{4.9}$$

where the coefficients are interpreted as $a_1 = (t - r/c)$, $a_2 = \phi_0$, and $a_3 = \omega_0^2 r/2c$. The coefficient a_3 divided by the sferic propagation distance r can then be used as a single-variable diagnostic of dispersion in the Earth-ionosphere waveguide. By considering how the parameter a_3/r varies in space and time, and

comparing this variation with the expected diurnal and geographic dependence of the Earth and ionosphere conductivities, we can investigate the spatial and temporal structures in waveguide perturbations that may be associated with EPP signatures. We refer to this dispersion diagnostic as the range-normalized dispersion. This analysis will present variations in this range-normalized dispersion, which is estimated from the phase fit function directly, and subsequently compute the range of waveguide cutoff frequency ω_0 and ionosphere effective height h.

4.2.4 Sfiles

WWLLN stations measure time-varying field information with a 2 meter electric monopole antenna, and sample at either 48 or 96 ksamples/second; resulting in time series measurements of the electric field from 0 Hz up to the Nyquist frequency of 24 or 48 kHz. Each station records the full waveform time series information–commonly referred to as "wideband data" in WWLLN operation terms–for a period of days to months depending on the size of the station's storage disk. Each day, stations sampling at 48 ksamples/second generate 16.6 GB of wideband data. This data volume is too large either for stations to store for long periods of time, or to transmit in real time to WWLLN servers, so several processing steps are needed in order to make the problem of locating lightning from wideband VLF data tractable. Each of the following steps are done continuously at every WWLLN station.

First, sferics are identified in the wideband data. Sferics appear as wave pulses with amplitude exceeding a noise threshold over most of the 6-24 kHz band, with total duration under 2 ms, and "positive" dispersion; that is, the high frequency components arrive before the low frequency components. The time of group arrival (TOGA) of this wave pulse is determined as the time when the slope of the phase curve as function of frequency near the center of the sferic bandwidth is 0. Each station reports TOGAs to WWLLN servers as soon as they are determined; lightning locations are then solved by comparing lists of TOGAs from all stations and finding locations that, were lightning to have occurred, sferics would have reached contributing stations at the TOGA determined by those stations. A more detailed description of this process is given in [*Dowden et al.*, 2002].

Information from each sferic is saved to 10-minute files, called Sfiles, on every station. Each line of an Sfile refers to a sferic detected by that station, and contains time, fit coefficients for the phase function given

column number	quantity	example
1	magic header	W210
2	station ID	10
3	UT file time	2021-07-08T04:01:00
4	UT TOGA offset (μs)	85 788
5	RMS waveform amplitude (SCU)	2709
6	TOGA offset from start of waveform (s)	0.000 389 205
7	Dispersion fit parameter a_1 (s)	$8.188\,06 \times 10^{-6}$
8	Dispersion fit parameter a_2 (rad)	2.655 66
9	Dispersion fit parameter a_3 (rad^{2}s^{-1})	380 397
10	Dispersion fit OK flag (0 or 1)	1
11	Sampling frequency (Hz)	95 991.635 41
12	N: number of waveform samples	128
13 to (N+12)	Waveform samples (normalized)	−0.001 410 68

Table 4.1: Contents of each line of an Sfile. Sfiles are in ASCII format, and columns are comma-separated. Sfiles are generated by each station, with filenames corresponding to the date and time of the file, with one-minute precision. The example values above are from an Sfile generated by the Seattle station (station ID = 10) with the filename S202107080401, meaning it contains sferics received between 2021-07-08 4:01 and 4:02 UT.

in equation 4.7, as well as electric field samples in a 1 ms window beginning at the trigger time. The full structure of each Sfile line is given in Table 4.1. WWLLN's sferic detection algoritm is given in *Dowden et al.* [2002], and reproduced here.

Each WWLLN station continually samples the electric field E at either 48 or 96 kHz. The moduli of the differences between subsequent electric field samples $E(i)$ is given by $|\Delta E(i)| = |E(i) - E(i-1)|$. The mean of every second of these moduli is computed, and every modulus that exceeds a thresold set at N times this mean triggers the capture of the subsequent 1.3 ms of E (64 or 128 samples). N is continually evaluated at each station in order to maximize detection efficiency.

Once waveform samples associated with a sferic are captured, the fast Fourier transform (FFT) of the samples is taken to determine the frequency content of the sferic. Although the Nyquist frequency associated with each station is either 24 or 48 kHz, only frequencies between 6 and 18 kHz are used to determine sferic dispersion. The phase of each frequency component is measured, and the phase function in Equation 4.7 is fit to phase as a function of frequency. The sferic is then checked for positive dispersion; that is, that higher frequencies are phase-advanced relative to lower frequencies. If the sferic passes the dispersion fit check, its time, phase fit, and waveform samples are recorded in a new line of the current Sfile.

column number	quantity	example
1	stroke time	7.3883×10^5
2	stroke latitude	4.9120
3	stroke longitude	-65.7302
4	station latitude	35.8721
5	station longitude	-106.3280
6	station ID	8
7	stroke ID	$76\,333$
8	a_1	5.3907×10^{-5}
9	a_2	-0.4223
10	a_3	$384\,413$

Table 4.2: Contents of each line of a pathlist.

4.2.5 Sferic matching and pathlist generation

Because Sfiles are recorded at the station level, they contain no information about the time or location of the lightning they eventually locate. However, associating lightning locations with Sfiles is relatively straightforward. Far-field VLF peak power estimates are recorded, along with lightning locations, and a list of stations that participating in the power estimation for each stroke, in WWLLN APfiles. For each station contributing to the Sfile archive, we extract all strokes in a daily APfile located by that station. For each of these strokes, we search that station's Sfiles for sferics that satisfy:

$$t_{\text{stroke}} - \left(t_{\text{sferic}} + \frac{r}{c_{\text{eiwg}}} \right) < \epsilon \tag{4.10}$$

where ϵ is the maximum acceptable timing error of $100\,\mu$s. This process is performed in `getsferics.m`.

Once stroke locations are matched with Sfile information, a list of stroke-station pairs is generated. This list contains stroke time, stroke latitude and longitude, station latitude and longitude, station ID, stroke ID, and the three phase fit coefficients. Because the stroke and station locations in the list are the endpoints of sferic propagation paths, we refer to this list as a "pathlist". An annotated excerpt from a pathlist is given in Table 4.2

This list represents the timing, start and end points of propagating sferics recorded by WWLLN, and includes their dispersion information. Once this list is generated, sferic information can be mapped onto a spatial grid, and spatial and temporal statistics of sferics can be calculated.

4.2.6 Spatial and temporal statistics of sferic properties

In order to investigate the spatial and temporal variation in WWLLN's sferic distribution, we use the pathlist described in the previous section to generate maps of sferic characteristics in latitude-longitude and time bins. This is performed for each day in the sferic dataset using the following procedure:

1. Define time bin width and bin edges. For a day beginning at time t_0, bin edges are then defined as $t_k = t_0 + k\Delta t$, where Δt is the time bin width, and k is an integer in the range $1 : \frac{\text{dataset time span}}{\Delta t}$. In this work, time bins have been fixed at 10 minutes, so a daily subset of sferic data is divided into 144 evenly-spaced time bins.

2. Initialize an empty 3-dimensional cell matrix, G, with dimensions $m \times n \times p$, where m and n are the number of latitude and longitude bins, and p is the number of time bins. For a $1^\circ \times 1^\circ$ latitude-longitude grid and 10-minute time bins, G has size $180 \times 360 \times 144$.

3. For each time bin k:

   (a) Find the subset of the pathlist with stroke times in $[t_{k-1}, t_k)$.

   (b) For each of these paths:

      i. Compute the set of waypoints lying on the great circle path between the stroke and station. This is done with the MATLAB `track2` function, which computes a set of evenly-spaced points along a geodesic. MATLAB `track2` performs this computation by first solving the inverse geodesic problem between the stroke and station locations to determine the distance between them and azimuths from one to the other; then solving the forward geodesic problem from the stroke location and starting azimuth to find path waypoints at evenly-sapced fractions of the total distance from the stroke location towards the station.

      The next step will be to find the unique latitude-longitude bins traversed by this path, and waypoint spacing determines which bins along the path are correctly identified. Since spatial bins defined by longitude will narrow in physical width with increasing latitude, a set of waypoints evenly-spaced in distance may "skip" narrow spatial bins at high latitudes when a fixed number of waypoints is used regardless of total path length. In this work, we use 400

points per path, corresponding to a 50 km spacing between points for a $20\,000\,\mathrm{km}$ path between two antipodes on a spherical Earth, which begins to skip over spatial bins at roughly $63°$ latitude. Since the majority of WWLLN paths are significantly shorter, and this work is primarily searching for auroral and subauroral impacts, 400 points was deemed a sufficient path spacing.

ii. Round each path waypoint to the nearest spatial bin center, and find unique values of these. This is an approximation of the list of spatial bins traversed by the sferic propagating between the stroke and station. Bins may not be detected if the spacing between path waypoints is larger than the path length inside the bin, as may be the case with long paths traversing narrow high-latitude bins as discussed above, or with paths that "cut the corners" of bins.

iii. Convert the list of unique, rounded waypoints to spatial bin indices by adding the offset between each bin's center latitude/longitude and latitude/longitude index; i.e. add 91 to each latitude, and 181 to each longitude. For a path traversing j unique spatial bins, this results in a list of indices $(\mathrm{lat}_i, \mathrm{lon}_i)|_1^j$.

iv. Append sferic information from the pathlist to each cell $G(\mathrm{lat}_i, \mathrm{lon}_i, k)$. We add the index of the stroke in its parent AP file, stroke time, azimuth between the center of the stroke's spatial bin and the current spatial bin, the three sferic dispersion fit coefficients, and the stroke-to-station distance, as a new row in this cell. When multiple paths cross a given latitude-longitude bin within the same time bin, the resulting entry in the 3D cell array will be a matrix whose rows each correspond to these multiple paths.

4. We now have a cell matrix G, of size $180 \times 360 \times 144$, where each element is a list of information related to sferics that traversed that latitude-longitude-time bin. G is a cumbersome variable to hold in memory because each of its elements has a variable size, resulting in huge memory overhead, so to speed up computation and save smaller files we can compute G and its products for each time bin k and concatenate these into 3D arrays. This means we sacrifice the ability to store G for future analyses, so it is important to determine which quantities are required for the analysis. We will compute the following derivative products from G:

(a) Number of path traversals: By counting the number of rows in each cell of G, we find the number of paths traversing each latitude-longitude-time bin.

(b) Perpendicularity of path azimuths: For each cell in G, we compute the perpendicularity of path azimuths as described in section 4.2.2. Since the azimuths are computed between the centers of the latitude-longitude bins containing the stroke and station locations, rather than these locations themselves, paths attributed to a single station detecting several strokes inside the same latitude-longitude bin result in a perpendicularity of 0.

(c) Mean and standard deviation of the range-normalized dispersion, a_3/r: the third dispersion fit coefficient, $a_3 = \frac{\omega_0^2 r}{2c}$, contains the waveguide cutoff frequency ω_0. Since we have already associated each sferic with a lightning location, we know its propagation distance r, and by dividing the fit parameter a_3 by the propagation distance we arrive at a measure of waveguide properties

Once we estimate the range-normalized dispersion a_3/r in each spatiotemporal bin, we can calculate the quiet-day average range-normalized dispersion by averaging in UT days with low EEP activity as measured by POES-MEPED. The determination of active vs. quiet days will be discussed in section 4.2.7. We will then investigate the difference between each active day's dispersion distribution and the quiet day distribution in northern-hemisphere nightside auroral and subauroral magnetic latitude bins.

As seen in Figure 4.2, WWLLN has more stations in the northern hemisphere than the southern, resulting in more propagation paths there. The nightside should have a greater ionosphere height, and therefore less dispersion; therefore, we expect enhanced dispersion from EEP to be more clear in the nightside. To obtain time series of dispersion in the nightside northern hemisphere, we find the spatiotemporal bins with local time within ± 5 hours of 0 LT, calculate the magnetic latitude at each of these bins, and find the average dispersion inside 5° bins between 50° and 70° magnetic latitude. The time series of dispersion averaged over each magnetic latitude bin can then be compared to energetic electron flux measured by POES satellites on field lines with footpoints inside these magnetic latitude bins.

4.2.7 Comparison with electron precipitation: the POES MEPED and MPE datasets

This work will use in-situ measurements of precipitating particles by the MEPED instrument suite on all POES satellites as a basis for comparison. POES-MEPED has clear shortcomings, described in the introduction of this chapter, but remains a useful tool for measuring subsets of the bounce loss cone. In particular, we will use integral electron flux in the E3 channel on the 0-degree telescope. The E3 channel is sensitive to electrons with energies greater than 300 keV, and the 0-degree telescope measures electrons with trajectories near antiparallel to the local zenith direction; thus, at high latitudes, these data should reflect precipitating (rather than trapped) electrons that will deposit their energy in the range of altitudes where subionospheric VLF waves reflect [*Peck et al.*, 2015; *Jaynes and Usanova*, 2020].

Because there are only five POES satellites spread over 3 sun-synchronous orbit planes, POES data alone cannot resolve local time structure in electron precipitation. In this work, we will assume electron precipitation is invariant in magnetic local time, and therefore the timing and magnetic latitude of POES observations may be used to determine whether EEP might occur at any local time.

POES-MEPED data will be used to determine whether each day in the sferic dataset contains radiation belt particle precipitation in excess of an arbitary threshold, separating "quiet" days and "active" days. We used set this threshold at $10^4 \mathrm{cm}^{-2}\,\mathrm{sr}^{-1}\,\mathrm{s}^{-1}$ in the 0-degree E3 channel, based on an inspection the MEPED data over the entire time series. This threshold was chosen in order to balance the number of quiet and active days, to ensure that averaging techniques would not be reliant on a very small dataset.

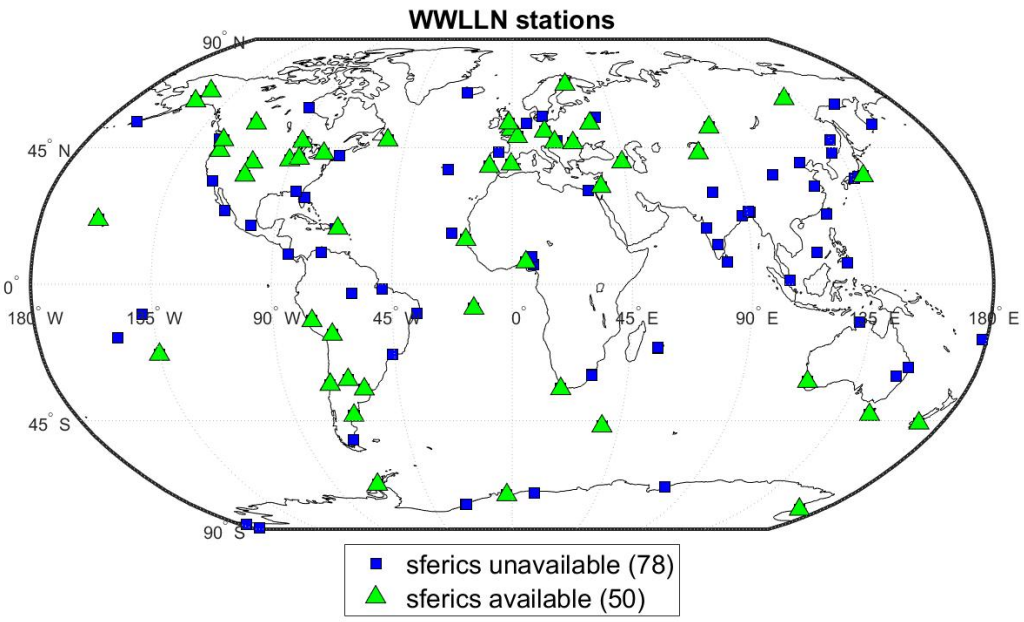

Figure 4.2: Map of WWLLN stations which contributed sferics to the dataset used in this work (green triangles), as well as non-participating stations (blue squares).

4.3 Observations

4.3.1 WWLLN sferic dataset: October-December 2022

As described in section 4.2.4, WWLLN does not typically archive wavefrom information. Sfiles are saved on each station for days to months, but are typically not collected on a server and are overwritten during the course of normal WWLLN operations. For this work, we copied Sfiles from stations to a WWLLN server for a period of about in late October-early December 2022. Because some stations' internet connections could not support the added bandwidth of transmitting Sfiles in addition to TOGAs, Sfiles were only archived from 50 stations. A map of the stations that contributed to this analysis is shown in Figure 4.2, and a list of these stations is presented in Table 4.3.

The process of setting up Sfile capture, as well as terminating Sfile capture, on the 50 stations used here required several days of work, resulting in uneven start and end times for each station's Sfile datasets. To

Table 4.3: Stations that contributed Sfiles to this analysis.

station	latitude (°)	longitude (°)
Anchorage	61.189	-149.8
Ascension	-7.9501	-14.378
Bayamon	18.372	-66.144
Bend	44.048	-121.2
Boulder	40.173	-105.24
Bryansk	53.299	34.246
BuenosAires	-34.554	-58.507
Chile	-33.027	-71.639
Chofu	35.657	139.54
Cordoba	-31.438	-64.193
Dakar	14.682	-17.468
Dunedin	-45.864	170.51
Edmonton	53.351	-112.97
Fairbanks	64.874	-147.86
FUTA	7.2982	5.1358
Gasu	51.961	85.97
Hermanus	-34.425	19.224
Honolulu	21.299	-157.82
Kazakhstan	43.255	76.856
Kingston	-42.986	147.29
LANL	35.872	-106.33
LaPaz	-16.539	-68.066
Lisbon	38.776	-9.1257
MarionIsland	-46.877	37.855
Milesovka	50.555	13.931
⋮	⋮	⋮
Monmouth	40.913	-90.639
MSSL	51.172	-0.42075
MTU	47.12	-88.546
Paris	48.713	2.2318
Perth	-32.066	115.84
Peru	-12.042	-75.321
Rikitea	-23.13	-134.97
Rochester	43.126	-77.63
Rothera	-67.569	-68.124
SANAEBase	-71.674	-2.841
ScottBase	-77.828	166.66
ScottBaseEz	-77.849	166.76
Seattle	47.654	-122.31
Sheffield	53.381	-1.4779
Sodankyla	67.37	26.623
StJohns	47.596	-52.678
TelAviv	32.113	34.806
Tihany	46.9	17.888
Transylvania	46.644	25.568
Trelew	-43.25	-65.308
USM	-33.036	-71.596
Valencia	39.514	-0.4257
Valparaiso	41.464	-87.039
Yakutsk	62.017	129.7
Yerevan	40.205	44.486

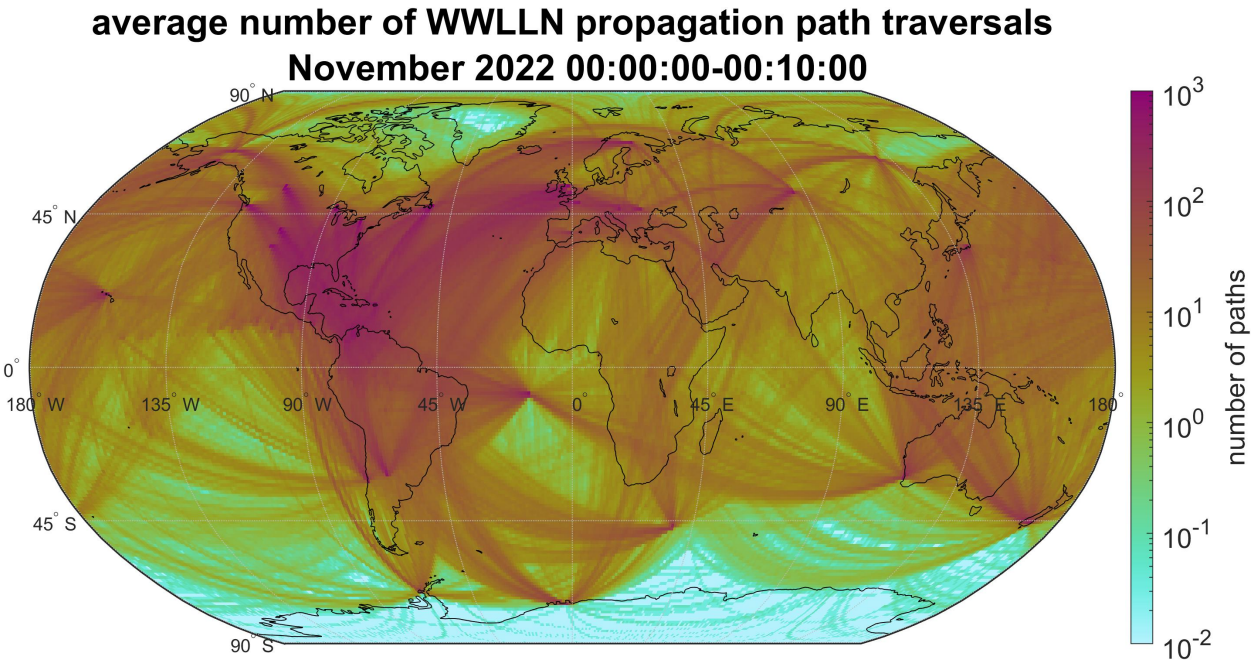

Figure 4.3: Number of paths in a sample 10-minute time bin in the average day in November 2022.

simplify the use of all stations in this work, we will use Sfiles from November 1 to November 30, inclusive, in the subsequent analysis.

4.3.2 Sferic propagation path distribution, perpendicularity, and perpendicularity-weighted path distribution

Sferic propagation paths were calculated for each day in the sferic dataset using the method described in section 4.2.6. Daily path distributions for the month of November 2022 were then averaged together to determine a nominal path distribution; a sample 10-minute time bin from that path distribution is shown in Figure 4.3. The path perpendicularity and perpendicularity-weighted path distribution for the same time bin in the nominal distribution are shown in Figures 4.4 and 4.5. Since the quantities plotted in each figure are averaged across multiple days in UT, the number of path traversals may fall below 10^0 in spatial bins which experienced relatively few path traversals in the plotted 10-minute time bin over much of November 2022. The distribution of stroke-to-station paths is best visualized in animations, which will be available in supplementary information.

It is immediately apparent from Figures 4.3, 4.4 and 4.5 that the WWLLN propagation path distribution

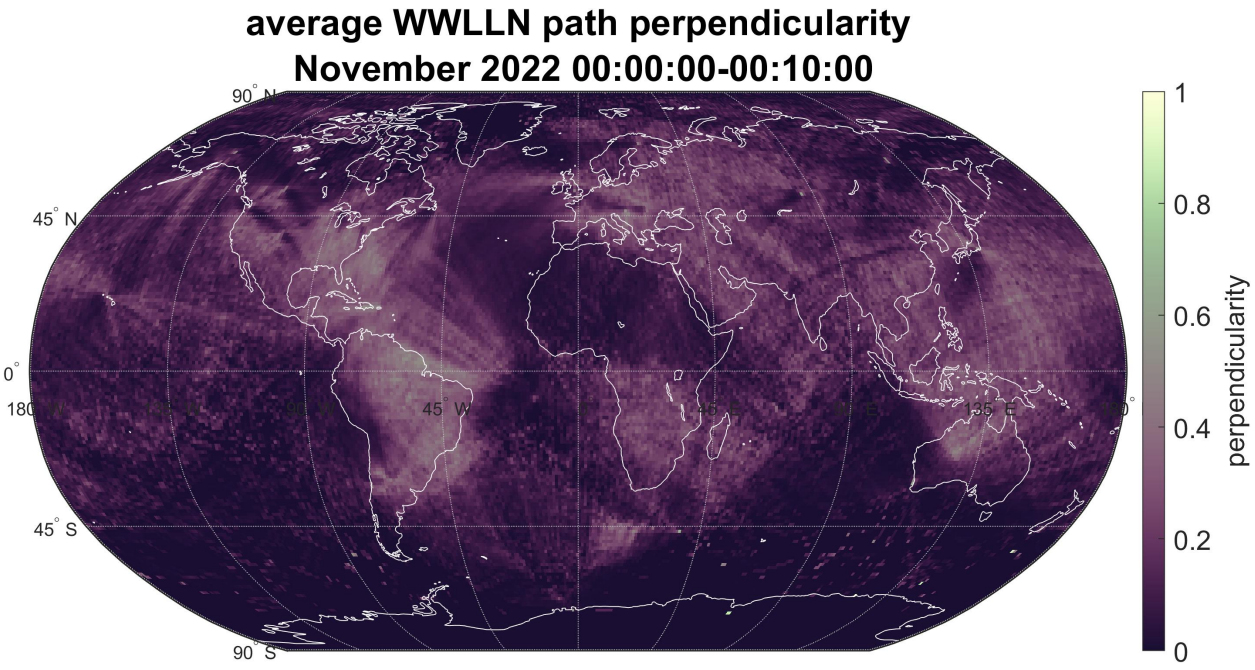

Figure 4.4: Path perpendicularity in a sample 10-minute time bin in the average day in November 2022. The same time bin is used as in Figure 4.3.

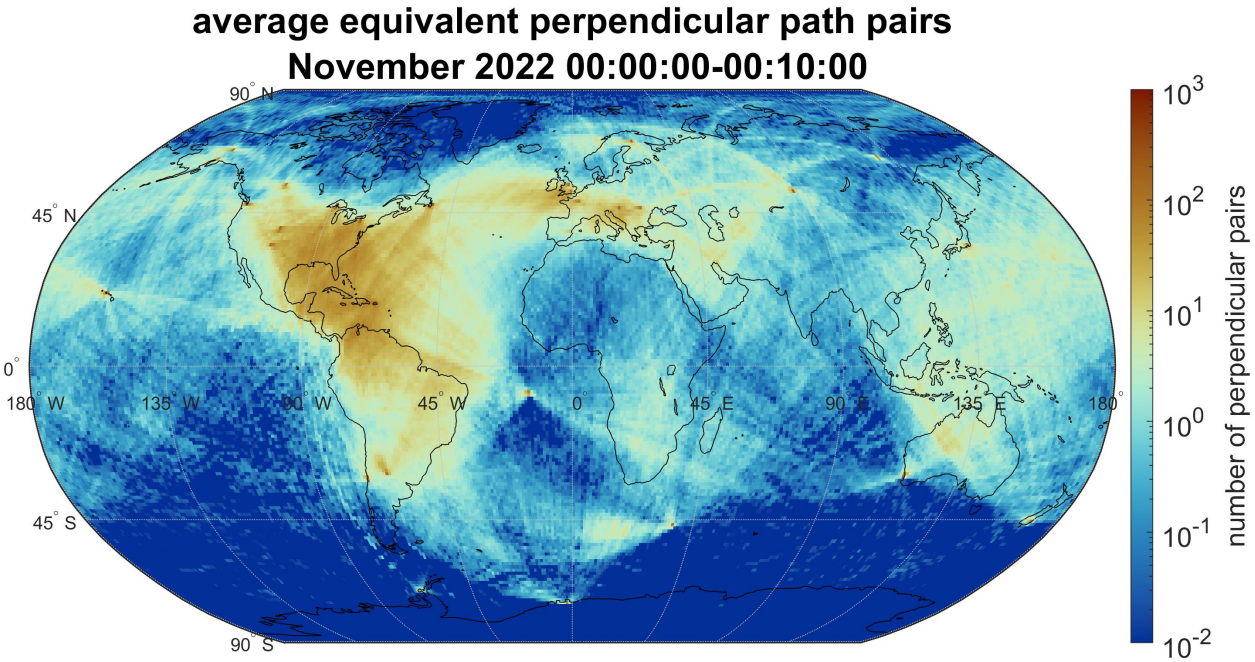

Figure 4.5: Number of equivalent perpendicular path pairs in a sample 10-minute time bin in the average day in November 2022. The same time bin is used as in Figures 4.3 and 4.4. Perpendicularity is used as a weighting factor to the number of path traversals to determine the equivalent number of perpendicular path pairs. See section 4.2.2 for more information.

does not evenly cover the Earth. Some regions, such as the North Atlantic and low- and mid-latitude Americas, are traversed by large numbers of paths from multiple storm-station pairs. Other areas, including the South Pacific and the Southern Ocean, as well as both Antarctica and the high Arctic, are traversed by very few paths, and these tend to result from single high-latitude stations. When the perpendicularity weighting is applied, these high-latitude paths disappear entirely. Our analysis of EEP regions will be confined to areas that are traversed by multiple intersecting paths, and significant portions of the auroral and subauroral region will not be adequately covered.

4.3.3 POES-MEPED 0-degree E3 flux

Precipitating electron data were obtained for the month of November 2022 from two sources: the POES-MEPED dataset, and the MEPED Precipitating Electron (MPE) dataset. To select EEP-active and -quiet days, we look for days with significant E3 flux measured by the 0-degree detector on any POES satellite in excess of $10^4\,\mathrm{cm}^{-2}\,\mathrm{sr}^{-1}\,\mathrm{s}^{-1}$ on field lines with foot points between $50°$ and $70°$ magnetic latitude. This threshold is chosen somewhat arbitrarily, as different authors have estimated different ionization rates from precipitating electron flux. Equally important to ionization in threshold choice was the need for sufficient days of data to be averaged into a quiet-day distribution. This threshold results in 12 days–November 6, 10, 12, 14, 15, 16, 17, 19, 21, 22, 23, and 24–contributing to the quiet-day average distribution. The magnetic latitude range, corresponding to $L = 3-7$ was driven by the need to search for primarily outer belt electrons, and reject enhanced flux at the South Atlantic Anomaly.

The 0-degree E3 flux for the month of November 2022 between $50°$ and $70°$ magnetic longitude is shown in Figure 4.6.

4.3.4 Spatial averages of sferic dispersion: quiet-day mean, active days, and nightside magnetic latitude binning

Sferic dispersion, represented as the range-normalized dispersion parameter $a_3/r = \omega_0^2/2c$ (see equation 4.7), is averaged at every space and time bin. An example map of the range-normalized dispersion is shown in Figure 4.7. To compare time variations in dispersion averages, we average in UT all the EEP-quiet days in the sferic dataset determined from the POES-MEPED 0-degree E3 flux. An example time bin of this

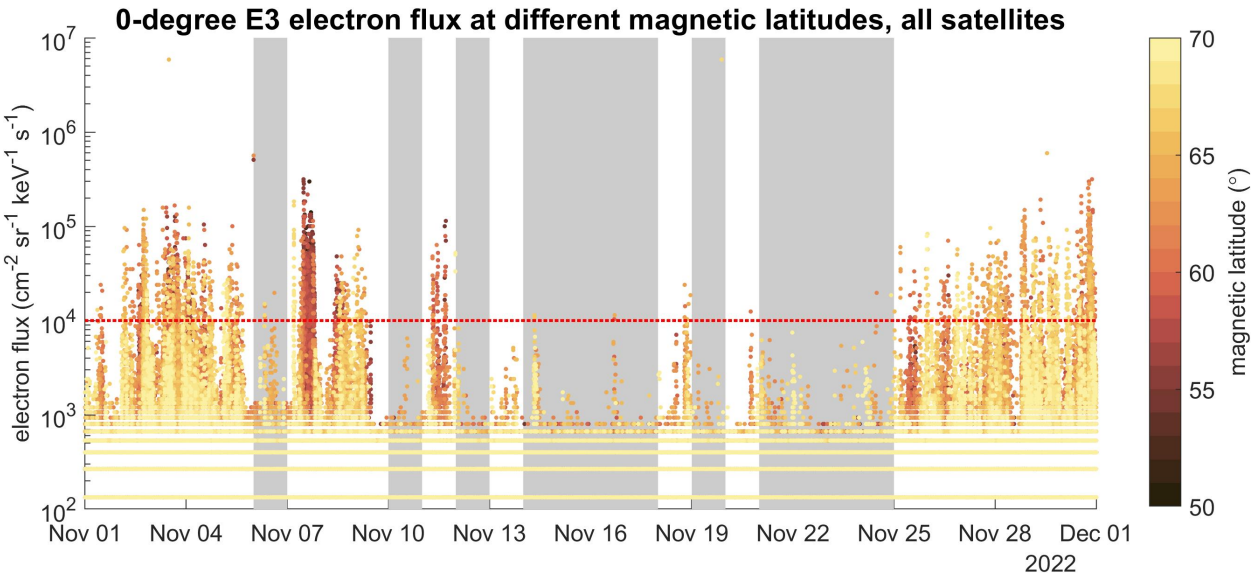

Figure 4.6: POES MEPED 0-degree E3 flux recorded by all satellites during the month of November 2022. The color of each point represents the magnetic latitude of the satellite when the measurement was taken; only magnetic latitudes between $50°$ and $70°$ are shown.

nominal distribution is shown in Figure 4.8. Dispersion values on the nightside are typically $0.06 - 0.08$ (median: $0.07\,\mathrm{rad}^2\,\mathrm{s}^{-1}\,\mathrm{m}^{-1}$), and $0.07 - 0.12$ (median: $0.09\,\mathrm{rad}^2\,\mathrm{s}^{-1}\,\mathrm{m}^{-1}$) on the dayside. Statistics of night- and dayside dispersion are shown in Figure 4.9. Note that spatial bins within 1 LT of the terminator are excluded for night- and dayside distributions, but included in the total distribution.

In addition to the enhanced dispersion on the dayside compared to the nightside, some paths in the South Atlantic Anomaly (SAA) region show high dispersion. We expect electron precipitation in the SAA to result in enhanced dispersion over the entire SAA region; it is unclear why this is not reflected in our observations.

Dispersion from EEP-active days–November 1-5, 7-9, 11, 13, 18, 20, and 25-30–is assessed by subtracting the quiet-day dispersion distribution from each of these active-day distributions. We then average this dispersion difference for all grid elements inside nightside northern-hemisphere magnetic latitude bins traversed by at least 1 equivalent perpendicular pair of paths, as described in section 4.2.6. Time series of the average and standard deviation of dispersion inside these nightside magnetic latitude bins are shown for example active days November 3 and 11, 2022, in Figures 4.10 and 4.11. These observations will be discussed in depth in section 4.4.

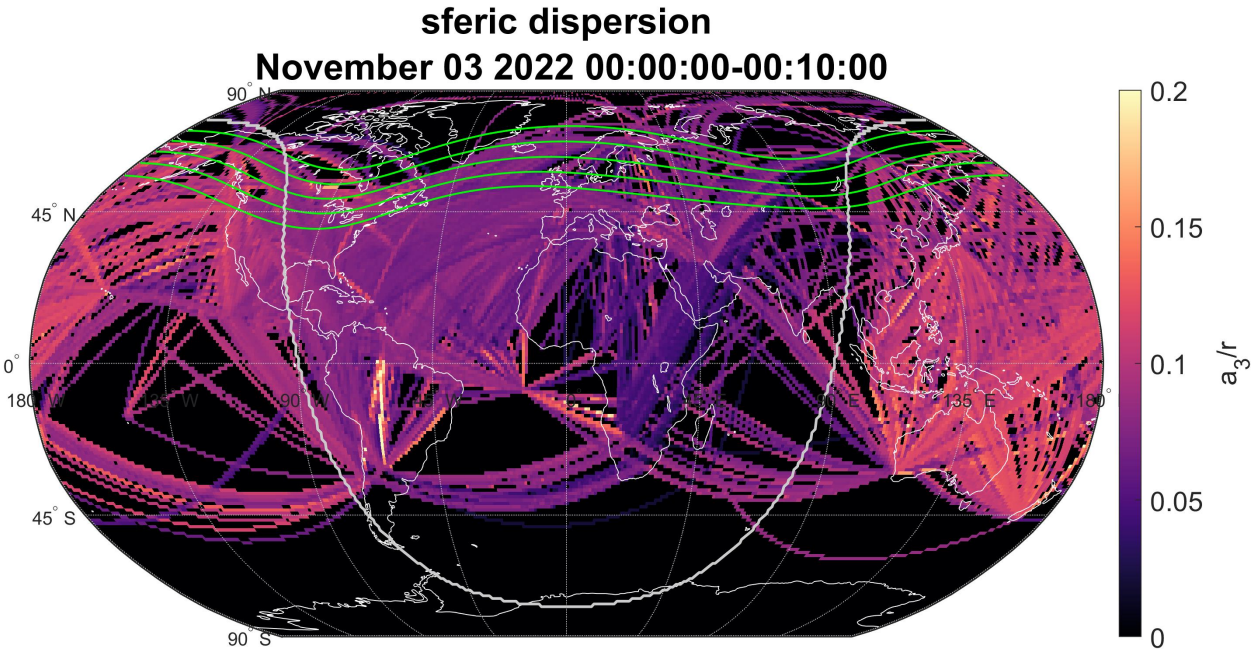

Figure 4.7: Range-normalized dispersion averages in spatial and temporal bins for a sample 10-minute time bin. The light gray contour marks the day/night terminator, and the green contours show magnetic latitudes of 50°, 55°, 60°, 65°, and 70°.

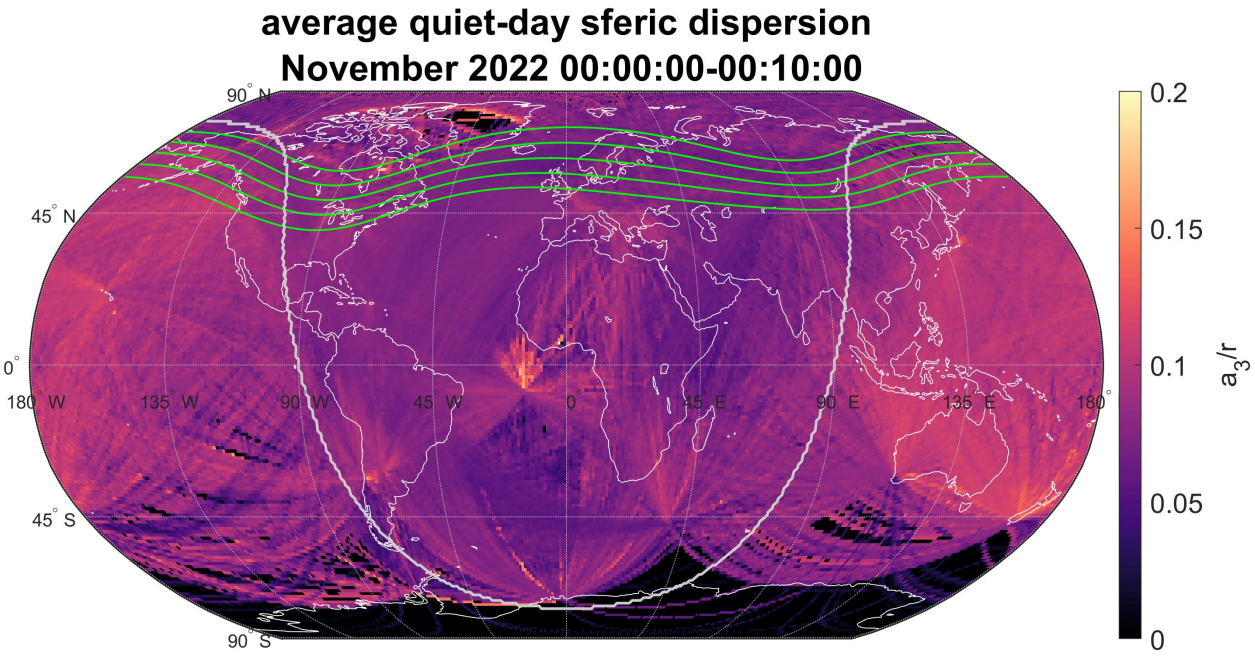

Figure 4.8: Average range-normalized dispersion for an example 10-minute time bin in the nominal quiet-day distribution, constructed by averaging in UT days with low POES MEPED 0-degree E3 flux. The same time bin is used as in Figures 4.3, 4.4 and 4.5. The light gray contour marks the day/night terminator, and the green contours show magnetic latitudes of 50°, 55°, 60°, 65°, and 70°.

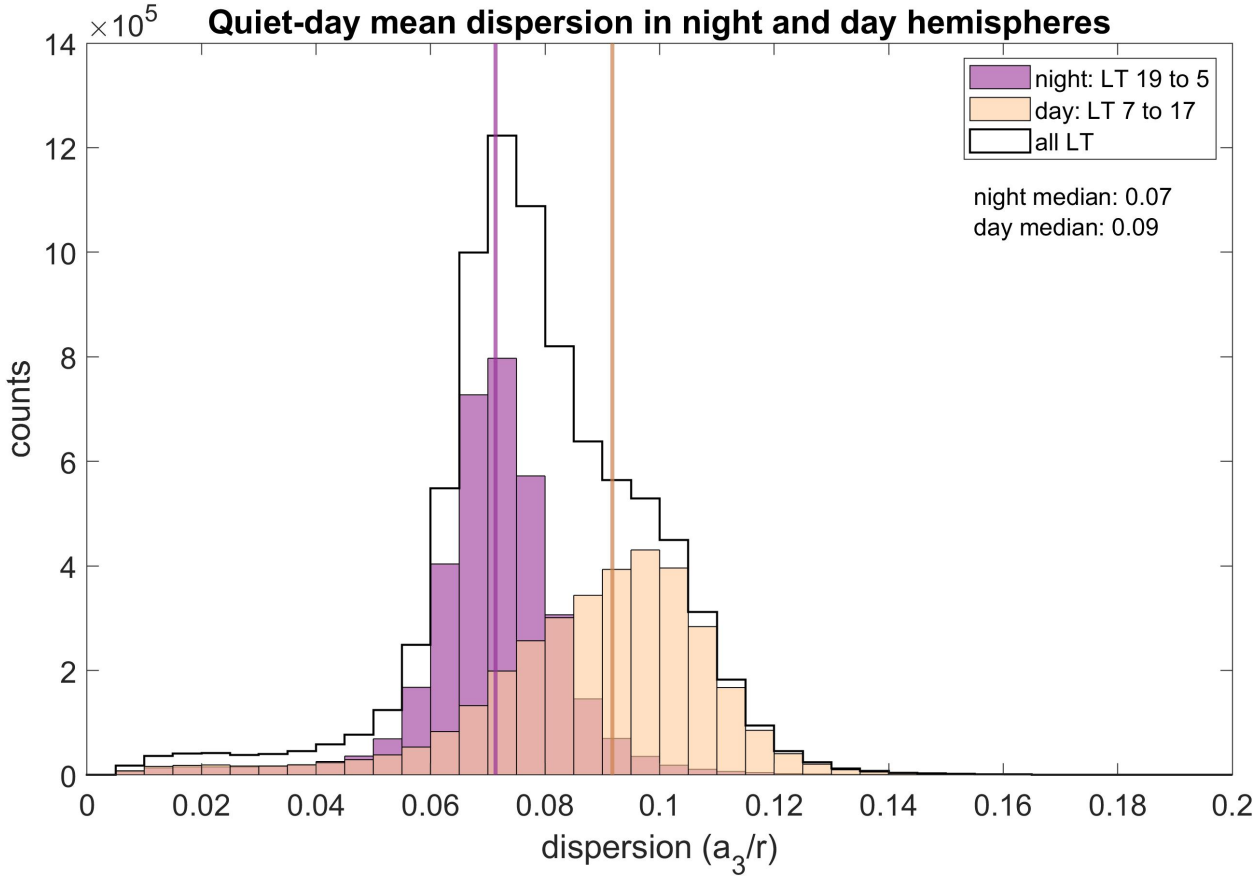

Figure 4.9: Dispersion in night and day hemispheres for the entire quiet-day mean distribution.

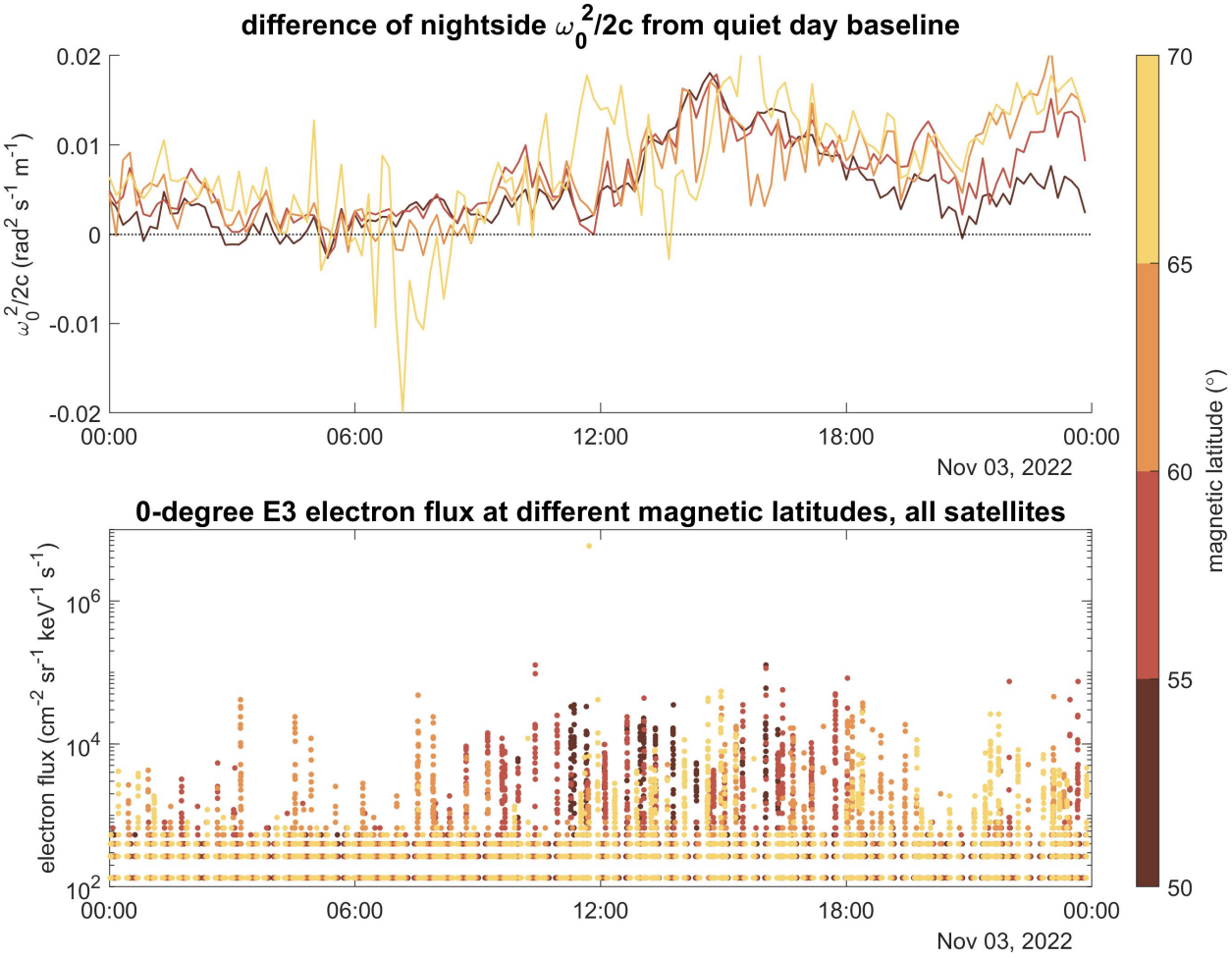

Figure 4.10: Difference in dispersion on active days vs. the quiet-day nominal distribution averaged within in nightside northern-hemisphere magnetic latitude bins for November 3, 2022.

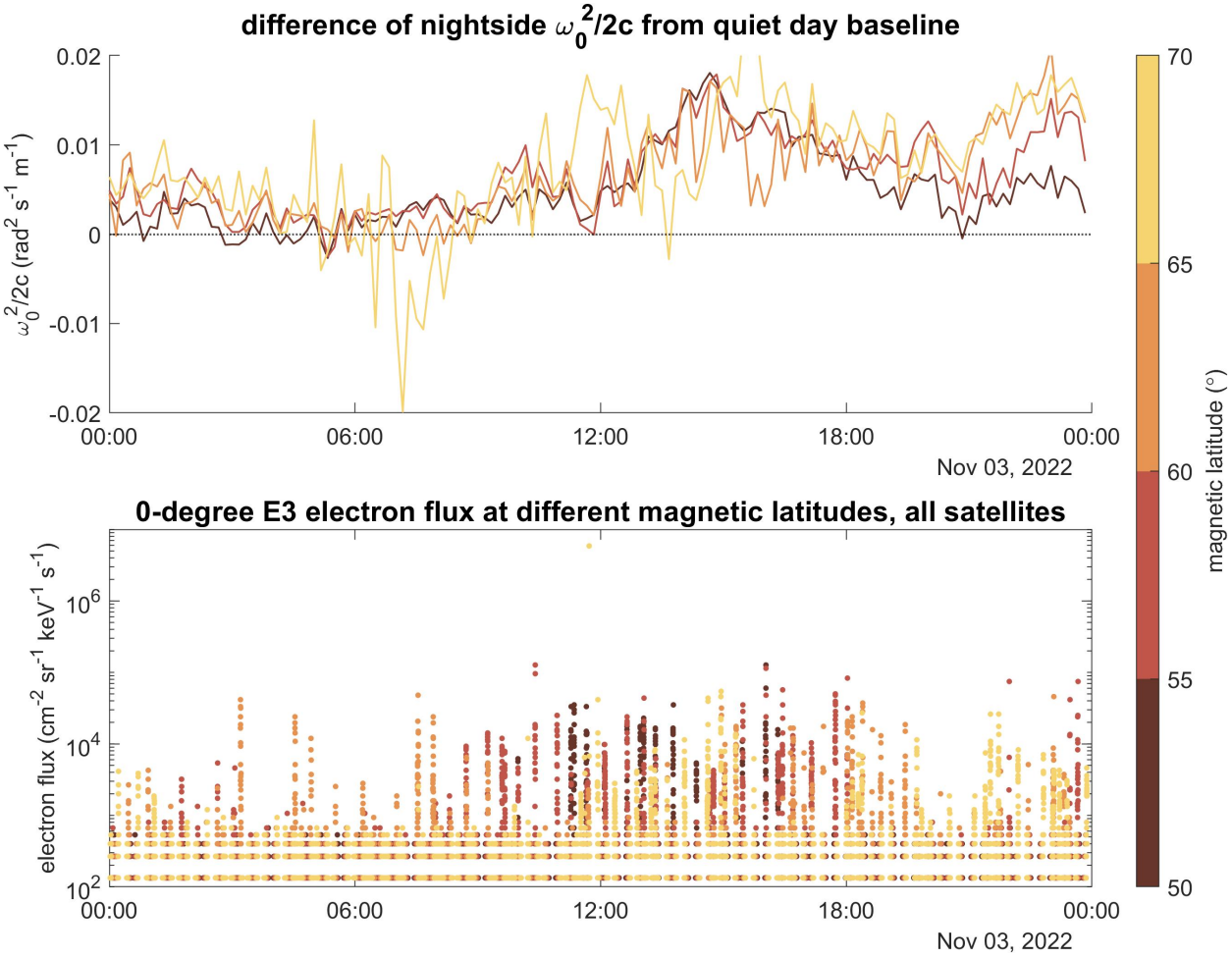

Figure 4.11: Difference in dispersion on active days vs. the quiet-day nominal distribution averaged within in nightside northern-hemisphere magnetic latitude bins for November 11, 2022.

4.4 Discussion

4.4.1 Expected and estimated dispersion

Qualitatively, we can see that mean dispersion varies as predicted in the nightside subauroral zone during EEP: as POES satellites detect increased precipitating electron flux at energies sufficient to penetrate to VLF reflection altitudes, sferic dispersion increases. Per equations 4.7 and 4.4, increasing dispersion is consistent with increasing waveguide cutoff frequency and decreasing ionosphere effective height, which is to be expected from increased low-altitude ionization by EEP. However, there are several issues with these observations.

Up to now, we have chosen to characterize the Earth-ionosphere waveguide with the range-normalized dispersion, a property of broadband sferics that we estimate with a hyperbolic fit to measured phase as a function of frequency. However, using equations 4.7 and 4.4, we can convert this dispersion parameter into estimates of the cutoff frequency and ionosphere effective height. The typical quiet-day nightside dispersion of $0.06-0.08\,\mathrm{rad}^2\,\mathrm{s}^{-1}\,\mathrm{m}^{-1}$ works out to cutoff frequencies of $f_c = 0.95-1.1\,\mathrm{kHz}$, and ionosphere effective heights of $140-160\,\mathrm{km}$; significantly lower cutoff frequencies and higher ionosphere effective heights than are realistic. In fact, these estimates appear to be off by a factor of $\sqrt{2}$ ($1/\sqrt{2}$ in the case of ionosphere height). A sample distribution of ionosphere effective height derived from the quiet-day dispersion relation is shown in Figure 4.12a, and the height estimate with this $1/\sqrt{2}$ correction factor is shown in Figure 4.12b. Applying this correction factor results nominal nightside cutoff frequencies of $f_c = 1.4-1.6\,\mathrm{kHz}$, and ionosphere effective heights of $95-110\,\mathrm{km}$; ranges much closer to previous measurements.

The source of this discrepancy between expected and measured waveguide conditions remains unclear, but is likely related to the use of the parallel-plate dispersion relation (equation 4.3) in formulating the dispersion parameter. The parallel-plate dispersion relation requires several approximations:

1. the radius of curvature of the waveguide is large relative to the waveguide height,

2. the waveguide height is large relative to the wavelength, and

3. the wave reflects from waveguide boundaries specularly, that is, with a reflection depth in the boundary much smaller than the wavelength.

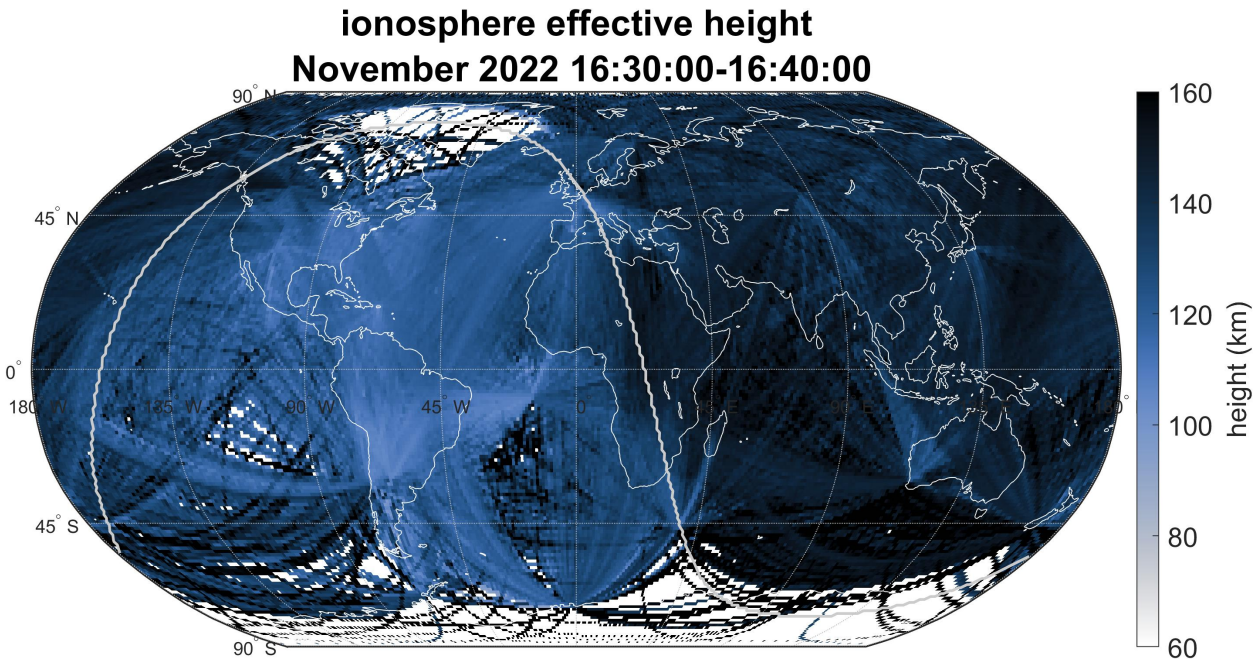

(a)

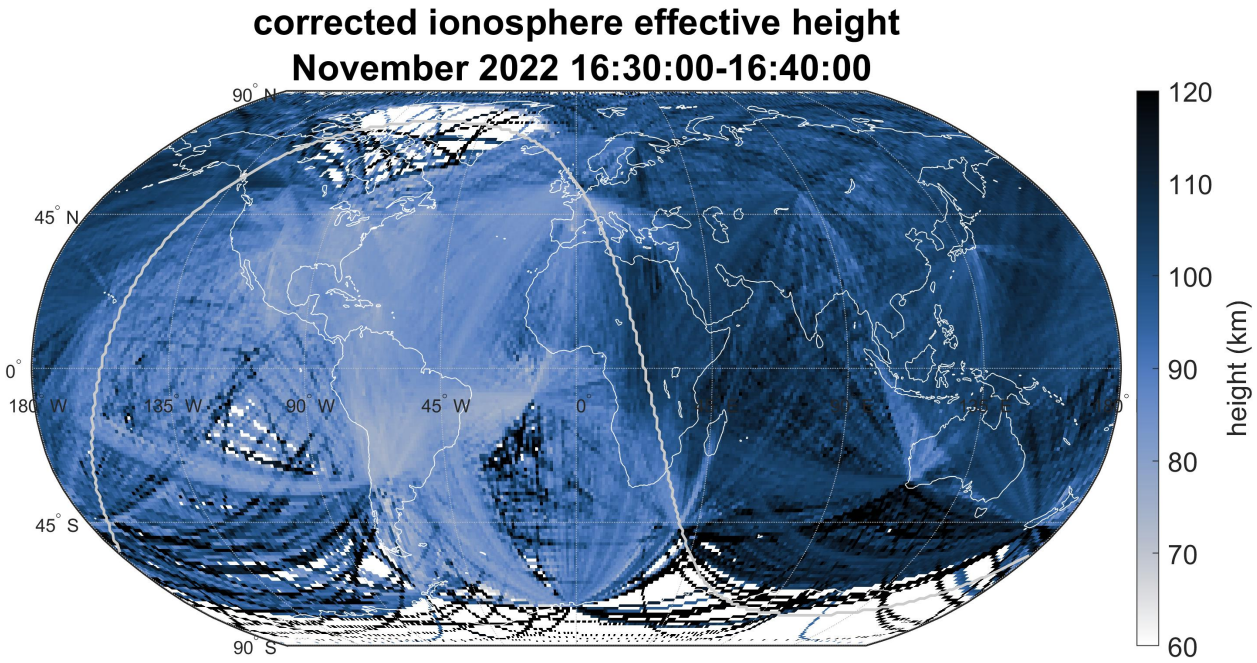

(b)

Figure 4.12: Ionosphere effective height derived from the quiet-day mean dispersion distribution for a sample 10-minute time bin. The height is calculated directly from the range-normalized dispersion according to equations 4.7 and 4.4 (a), and with a $1/\sqrt{2}$ correction factor (b). Note the change in color scale.

For our purposes, the first approximation is likely valid; the Earth's radius ($6371\,\mathrm{km}$) is more than ten times the ionosphere height at the VLF reflection altitude ($65 - 100\,\mathrm{km}$). However, the VLF wavelength is similar to the the waveguide height, with wavelengths in our $6 - 18\,\mathrm{kHz}$ window equal to $16 - 50\,\mathrm{km}$. Perhaps more significantly, the ionosphere is not a sharply-bounded reflector; a feature which may explain the the difference in measured dispersion from the expected value.

Radio waves incident on the lower ionosphere from below undergo frequency-dependent refraction, so different frequency components of a broadband sferic incident on the same region of the lower ionosphere will be dispersed in space when they are refracted and exit the ionosphere; the higher-frequency component will penetrate deeper into the ionosphere, and exit the ionosphere further down-range, than the lower-frequency component. This results the two frequency components propagating with different eigenangles in the waveguide, and ultimately a receiver detecting a sferic some distance from the source lightning will receive high-frequency components of this sferic that have traveled longer path lengths than lower-frequency components. Figure 4.13, adapted from *Shao et al.* [2013], shows these paths for a single ionospheric reflection. This geometrical effect should result in higher frequencies being phase delayed relative to lower frequencies, reducing the measured range-normalized dispersion that results from fitting equation 4.9 to sferic phase measurements.

We can check our estimate of sferic dispersion against a propagation model to test whether our measurements of sferic phase, and estimate of range-normalized dispersion, compares well with the same treatment on a synthetic sferic. To do this, we will investigate the relative phase of frequencies propagating in a realistic Earth-ionosphere waveguide, fit equation 4.9 to the measured phases at a range of propagation distances from the signal source, and calculate the variation of range-normalized dispersion, cutoff frequency, and effective ionosphere height with distance. The Longwave Mode Propagator (LMP) code, a mode solver developed by *Gasdia and Marshall* [2021], is a straightforward model similar to the LWPC [*Ferguson*, 1998] that lends itself to such investigation. A sample LMP simulation is shown in Figure 4.14; note that the final waveguide height calculated based on the phase fit is in a similar range to that estimated from actual WWLLN sferics.

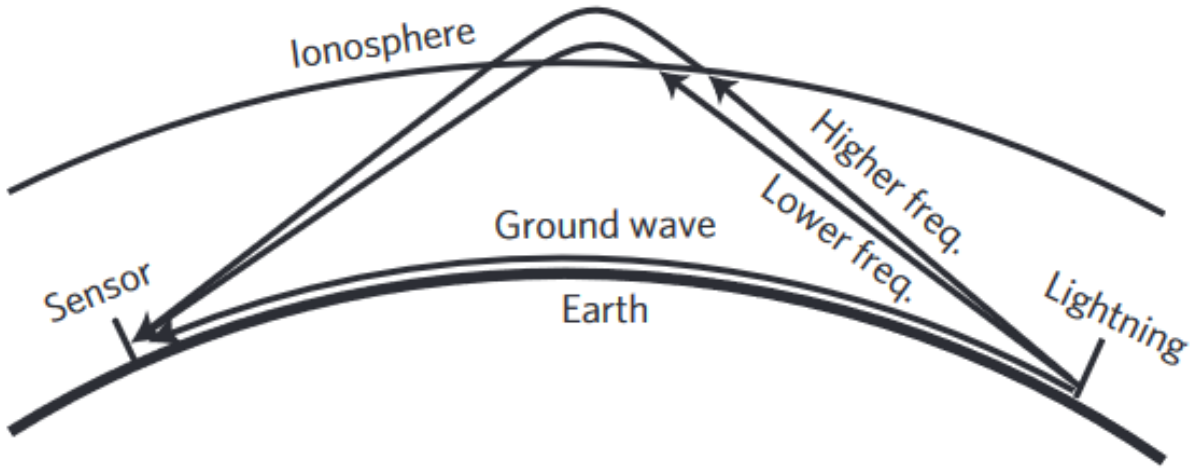

Figure 4.13: Ionospheric reflection of higher- and lower-frequency components of a VLF sferic, adapted from *Shao et al.* [2013]. Note the higher-frequency component penetrates further into the ionosphere, and hence travels further than the lower-frequency component between the lightning stroke and the receiving station.

4.4.2 Relationship between POES precipitating electron flux and increased dispersion

We highlighted two days in Figures 4.10 and 4.11 during which increased precipitating electron flux measured by POES agrees well with increased dispersion, both in timing and magnetic latitude. However, the month of November 2022 contains numerous examples where either WWLLN sees significant dispersion increases and POES does not observe increased precipitating flux, or the inverse occurs. The first case is consistent with precipitation occuring in discrete local time regions, rather than accross all local times; since POES spacecraft only occupy three unique orbital planes and therefore only sample a small subset of local times, precipitation occurring in regions outside this coverage could result in enhanced WWLLN sferic dispersion without an accompanying enhancement in POES precipitating electron flux. Alternatively, enhanced dispersion in the absence of EEP may be due to ionospheric variability from other sources, including thunderstorms.

The inverse case, where POES measures enhanced flux but WWLLN does not see enhanced dispersion, could be a result of poor propagation path coverage in precipitation regions. As Figures 4.3-4.5 and 4.7 show, WWLLN's path coverage varies dramatically across the globe. Where a small number of path swaths–that is, storm-station pairs–is responsible for the coverage of a geographic area, deficiencies in this station's

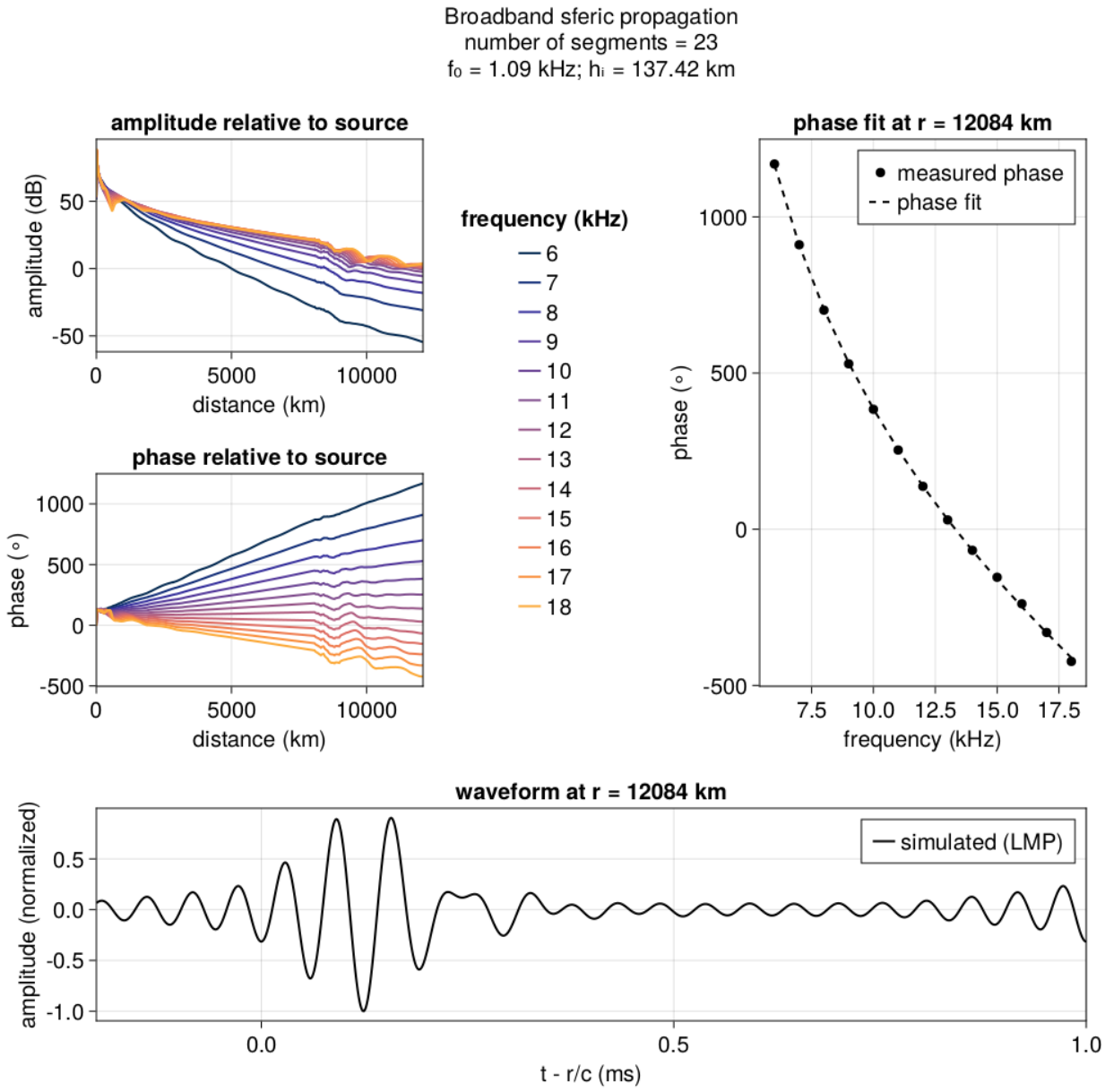

Figure 4.14: Sferic dispersion simulation experiment with the Longwave Mode Propagator code [*Gasdia and Marshall*, 2021].

ability to accurately measure sferic phase result in dispersion errors that are mapped to the entire geographic region. This analysis has not attempted to remove outlier sferics from the distribution, relying instead on the averaging technique to minimize the influence of any erroneous dispersion measurements. However, the WWLLN path distribution makes it clear that estimating waveguide conditions at auroral and subauroral latitudes using this technique would benefit greatly from more WWLLN stations at high latitudes, in order to increase path coverage in EEP regions.

4.4.3 Weaknesses in spatiotemporal grid averaging method and path distribution

Statistics of range-normalized dispersion and other sferic properties were sufficient to qualitatively observe increased dispersion at subauroral latitudes during EEP times measured by POES. This method was chosen for its computational simplicitity, allowing for runtimes approaching real time and relatively low memory requirements. However, this method had several shortcomings that should be addressed.

Sferic paths were gridded using a fixed number of waypoints on a latitude-longitude grid. This technique results in some grid cell traversals being missed at higher latitudes, when 1° longitude is significantly narrower than at the equator, and for longer paths, where waypoint spacing was increased. These shortcomings could be addressed using a different gridding scheme that assigns path traversals to grid center locations that are within a set distance of the path in question. This technique, while more computationally challenging, would eliminated missed path traversals.

The importance of weighting of path traversals must also be investigated. As implemented in this work, all paths receive equal weight for each averaging step, potentially resulting in large and redundant path populations overpowering smaller path populations carrying important information. This issue could be easily investigated if the full distributions of sferic information in each spatiotemporal cell were retained, rather than relying only on statistics of these distributions.

Finally, the dataset in this work is not sufficiently large for long-term or multi-event statistical statistical studies of EEP impacts on sferic dispersion. WWLLN also measures few paths at subauroral and higher latitudes, which are further reduced when a minimum perpendicularity-weighted path threshold is included. This work would benefit from longer-term archiving of Sfiles, and from deployment of more WWLLN or similar stations at higher latitudes.

4.5 Summary and conclusions

We presented a new technique for detecting signatures of energetic electron precipitation using broadband WWLLN sferics by calculating the range-normalized dispersion of these sferics, mapping that dispersion parameter to propagation paths, and comparing spatial statistics of sferic dispersion with electron precipitation measured by the POES spacecraft. Estimated dispersion was shown to decrease at during periods of enhanced precipitating electron flux for several cases in the sferic dataset, qualitatively agreeing with expectation. The use of sferic propagation paths, rather than VLF transmitter-receiver propagation paths, represents a promising advancement in using transient and spatially distributed sources for lower ionosphere studies. The broad global distribution of lightning results in propagation paths sampling waveguide conditions in swaths, potentially enabling far greater horizontal resolution of lower ionosphere perturbations than is possible with a network of static transmitters and receivers.

However, there are several important shortcomings of this technique that must be addressed if it is to be successfully used to study EEP ionization in the mesosphere-lower thermosphere. First, the discrepancy between estimated and expected waveguide conditions, namely the waveguide cutoff frequency and the ionosphere effective height, must be resolved. This discrepancy is likely the result of the VLF reflection process in the ionosphere, which is non-specular and results in significant path differences between different frequency components of individual sferics. Future work will seek to either replace the parallel-plate dispersion relation (equation 4.3) with a more accurate model, or estimate a correction factor based on a range of ionosphere profiles.

If this discrepancy is resolved, waveguide cutoff frequency and height can be directly calculated from the range-normalized dispersion parameter. An alternative method of estimating waveguide parameters, however, is to compare each measured dispersion with that calculated from a longwave propagation model. Current simulations with such a model reproduce dispersion estimates in the same range as the technique presented here, suggesting that waveguide conditions could be obtained by finding the conditions producing the best fit between the simulated and measured sferic dispersion. This technique has the glaring disadvantage of adding significant computation time by requiring multiple runs of the mode-solver code for each of the several million sferics in a single-day sferic dataset. Some of this computation time could be saved by bundling sferics into groups according to spatiotemporal proximity and averaging them before performing

the simulation; such a modification might reduce the spatial resolution that is one of the most compelling features of the sferic propagation path distribution.

Finally, it is impossible to escape the fact that WWLLN does not detect many sferics traversing high latitudes. Although the frequency of lightning at high latitudes is increasing [*Holzworth et al.*, 2021], the vast majority of lightning occurs at tropical and midlatitudes. The efficacy of this technique to study high-latitude phenomena is therefore limited by the spatial distribution of WWLLN stations. Although high-latitude sites are unlikely to markedly increase WWLLN detection efficiency, their usefulness for space physics investigations has now been demonstrated. Alternative station models, such as co-hosting with AARDDVARK sites, remotely-deployable non-telemetered stations, and ridealongs on Arctic scientific cruises or Antarctic instrument campaigns may provide a way forward to fill this measurement gap. Since sferic measurements for space physics investigations need not be telemetered in real time, deliberate high-latitude deployment campaigns and collaborations with citizen-scientist hosts in Arctic communities are promising ways forward to address science questions in the high-latitude lower ionosphere using measurements of lightning sferics.

Chapter 5

Investigating spatial inhomogeneity in the global electric circuit with simultaneous stratospheric balloon measurements

This chapter contains significant contributions from Michael P. McCarthy, especially in the description of the balloon instruments.

5.1 Introduction

The global electric circuit (GEC) is a current system that linking the lower ionosphere and ground, which form the upper and lower conducting boundaries on which the current may close. Charge is driven upwards by thunderstorms and other drivers, such as electrified shower clouds, maintaining a 250 kV ionospheric potential relative to the ground. Charge then leaks downward through the weakly-conducting fair-weather middle atmosphere until reaching the ground. This circuit carries roughly 1 kA of current, resulting in a fair-weather return current density of around $1\,\mathrm{pA\,m^{-2}}$[*Rycroft et al.*, 2000; *Williams*, 2009; *Siingh et al.*, 2007]. As GEC model development has progressed, the influences of various drivers on the return current density have been studied, including solar and cosmic dynamics [*Rycroft et al.*, 2007; *Jánský and Pasko*, 2014; *Borovsky*, 2017].

One of the key assumptions in GEC models today is the invariance of the return current density in fair-weather regions. This assumption is supported by data from the EMA balloon campaigns *Holzworth et al.* [1984], which measured vertical electric field and conductivity using several long-duration stratospheric balloons, and found that simultaneous measurements of the return current density made by balloons over 1000 km separated agreed to within 20% while both balloons were over fair weather. This invariance is implied in a simple 1D GEC model, where the symmetry of the lower ionosphere and ground conductors demand an equal ionosphere potential everywhere. Building on this simple model, studies on the impacts of various drivers on atmospheric electricity and elements of the GEC can proceed by comparing measurements of source effects with the fair-weather response.

One promising direction of work is to establish the relationship between global thunderstorm activity and the fair-weather return current. If measurements of the fair-weather return current could be used as a proxy for global thunderstorm activity, studies into the long-term variability of thunderstorm occurrence, and the impacts of global lightning and thunderstorms on the atmosphere and beyond, could be undertaken using fair-weather return current measurements from a small number of instrumented observatories.

Such work is only possible if the spatial invariance of the fair-weather return current is a reasonable assumption; otherwise, these studies will measure local effects on atmospheric electricity rather than the impacts of global drivers. In order to investigate this invariance, we flew two simultaneous stratospheric balloons, carrying instruments to measure electric fields and conductivity, in June 2021. This chapter will

report on those instrument packages and flights, present atmospheric electrical measurements, and discuss these data in the context of previous expectations.

5.2 Balloon-borne instrument design and methods for comparison with other data sources

5.2.1 Experiment overview and implications for payload design

The goal of the balloon campaign was to make simultaneous measurements of the stratospheric electric field and electrical conductivity with at least two balloons, separated by at least several hundred kilometers, for at least 24 hours. Additionally, because thunderstorms are more common over land than over the ocean, measurements taken over the ocean would be less likely to be contaminated by nearby thunderstorms.

In order to achieve the desired spacing between balloons and make measurements over the ocean, we chose to launch from central Oregon, USA, during the northern hemisphere summer, when the stratospheric zonal wind is consistently westward. Carried by this wind, the payloads would traverse the Pacific Ocean in 4-5 days, which set our maximum flight time. This short flight duration, as well as the relative light weight (45 lbs/15 kg) of the payloads allowed the use of hand-launched zero-pressure balloons, which are significantly smaller, easier, and faster to launch than superpressure balloons of equivalent free lift. Zero pressure balloons also achieve higher peak altitudes, at the expense of longevity and diurnal altitude stability. Because of this, the electric field and conductivity instruments were required to be effective between $15 - 40\,\mathrm{km}$ altitude.

Each balloon payload would continually measure the vector electric field and conductivity until the flight was terminated. In order to verify each balloon was in fair weather, we compared balloon position with lightning locations, nearby cloud-top temperature, and nearby precipitation.

Each balloon payload carried two Langmuir probe pairs, with one pair oriented vertically and the other horizontally. A central housing consisted of insulating foam walls fixed into an electrically isolated aluminum frame. The housing was surrounded on its four sides by metal plates, isolated from the frame with ceramic standoff, and electrically connected to instrument ground. Each probe was made from a 0.8 mm thick by 0.30 m diameter spun aluminum sphere attached near the end of a 1.50 m fiberglass tube. The upper vertical sphere was mounted 1.50 m along a 2.0 m boom, with the free end of that boom attached to the load line. The probe spheres and ground plates were coated with Aerodag in order to raise and uniformize the work function of these metallic surfaces.

By measuring the potential of each probe sphere relative to payload ground, and taking the differences of the vertical and horizontal potentials, we could determine the potential difference in the vertical and horizontal directions; since the distance between each probe is known and fixed, the electric field in the vertical and horizontal directions is obtained. Additionally, the payload was rotated at about 2/3 RPM by an electric motor mounted at the tip of the upper vertical boom. The rotating horizontal probes allow a vector measurement of the electric field, provided the electric field varied slowly relative to the spin period.

5.2.2 Gains and measurement resolution

Earlier measurements of fair-weather electric fields are near 0.1–1 V/m at altitudes of 20–35 km *Holzworth et al.* [1984]; *Thomas et al.* [2009], corresponding to potential differences of 0.3–3 V measured by Langmuir probes separated by 3 meters. In order to measure either direction of vertical electric field, and fit the expected range of fair-weather electric field into an analog-to-digital converter (ADC) range of 0–4.096 V, the potentials on the vertical and horizontal probes were subject to two different gains, as shown in Table 5.1, with an added 2.048 V offset voltage before the ADC. Probe potentials were sampled every 5 seconds.

We designed the sampling scheme to measure conductivities from 10^{-13} to 10^{-10} S/m, covering the values expected over the 15–35 km altitude range. Conductivity was measured over 15 second intervals every 10 minutes. At the beginning of each conductivity measurement, the vertical probes were first connected via a low leakage reed switch to electrical ground for one second, and were then oppositely biased to one of ± 5 V, with bias voltages alternated on successive conductivity measurements. After one second at the bias voltage, the switches were opened, and the probes were allowed to relax to the potentials set by the ambient electric field. Each probe potential was sampled 10 times per second for 15 seconds, including the two seconds of probe biasing. Conductivity σ is measured by fitting an exponential decay model $V(t) = V_0 \exp(-t/\tau)$ to the potential times series, where the time constant τ is related to the conductivity σ with $\sigma = \epsilon_0/\tau$, where ϵ_0 is the vacuum electrical permittivity.

5.2.3 Telemetry

Each payload used a RockBLOCK 9603 short burst modem to send and receive data using the Iridium satellite network. Data was transmitted in 340-byte packets every minute, which were then sent as email

channel	gain	input range (V)
V_1, V_2	$-1/2$	± 4.096
V_{diff}	$1/7$	± 14.4
H_1, H_2	$-3/2$	± 1.37
H_{diff}	15	± 0.140

Table 5.1: Gains and saturation voltages for the potential measurements

messages to designated addresses for monitoring and archiving. Commands for dropping ballast or cutdown could be sent via email to the RockBLOCK system using groundstation software, which would be received at the addressed payload upon the next attempted packet transmission. This telemetry scheme allowed monitoring of instrument data, as well as payload location, environment variables and health, once per minute. During a test campaign, only about 65% of packets were successfully received. Packet buffer and retry functions were added to improve on this, and the science flights saw data throughput increased to 93–94%.

Electric and magnetic field measurements, collected every 5 seconds, were reported in the next transmitted packet after collection. The conductivity measurements from two vertical spheres, taken at 10 samples per second, accounted for significantly more data, but only one set of these was undertaken in a 10 minute interval. The conductivity measurements were split into 10 groups of 30 interleaved measurements, with one group assigned to each of the 10 packets sent over a 10 minute interval between conductivity measurements. This interleaving allowed that if one packet is dropped, 15 non-contiguous measurements, rather than a contiguous run of measurements, out of 150 measurements are lost from the relaxation time series for each vertical sphere.

A GPS module provides precise latitude, longitude, and altitude information for the payload. Other information, such as payload ID, timestamp, sequence number, voltages, currents, temperatures, error and status flags comprise the remaining content of each packet. Such information provides assurance that the electronics are working nominally, that is, not contributing errors to the measurements.

5.2.4 Calibration

A calibration procedure was used to estimate any systematic errors in the electric potential and conductivity measurements, and to ensure that each instrument was functioning according to design. For the electric

potential measurements, voltages from a calibration source were applied to the inputs or directly to the probes, and measurements were taken from different points in the signal chain: at the preamp, where the output should equal the input; and at the outputs of the inverting and differential amplifiers (gains in Table 5.1). By taking measurements at multiple points, the effects of different sections of the electronics were isolated and verified to be within specifications.

The conductivity measurement process was validated through two procedures. The first procedure checked the signal processing and proper framing of the data. In place of a vertical probe, a small resistor-capacitor testing box, configured with a 3 second relaxation time, was applied to the input connector. After a bias voltage momentarily charged the capacitor, charge would leak away through the resistor as the capacitor voltage decayed towards ground. This procedure simulates a conductivity probe at high altitude. The second procedure checked for current leakage paths at the probe and front end electronics. After cleaning the boom and input circuitry, the probe was charged and allowed to float. The probe must hold its charge for several minutes, demonstrating no significant leakage paths. Since we expect leakage times at altitude to be of order seconds, leakage times more than two orders of magnitude longer are acceptable.

After the probes and analog board were integrated with the ADC and microcontroller board, the probe measurements were tested again, but this time, data in the transmitted packets were extracted and displayed. This allowed us to check that the measurements were propagated through the entire system correctly.

5.2.5 Ballast and cutdown systems

Zero-pressure stratospheric balloons experience significant altitude variability during a diurnal cycle, as they follow the diurnal expansion and contraction of the atmosphere. Differential heating of the balloon gas relative to the surrounding atmosphere causes the balloon to vent helium at each apogee, leading to a decrease in apogee and perigee altitude on each subsequent day.

In order to counteract altitude lowering due to daily helium loss, the balloon payloads in this campaign carried 16 lbs (7.3 kg) of steel shot ballast in eight different tubes attached to the central payload gondola. Ballast could then be dropped from individual tubes by uploading ballast "arm" and "fire" commands, which would fire pyrogen ignitors that would burn through a gunpowder-coated cellophane layer at the base of each ballast tube.

Additionally, the balloons had several redundant cutdown systems to ensure the flights could be terminated if the balloons approached restricted commercial or foreign airspace, or if there was a problem early in the flight and a recovery on land was desired. A terminate block, containing a loop of load line through two parallel squibs, was tied into the load line between the balloon and the instrument payload; one of these squibs could be fired via a series of commands, and both were connected to separate timers that would fire them a set time after the board was powered on. Since the terminate block was located well away from the main payload gondola, and wires connecting the two could disrupt the upper vertical probe measurements, communication between the terminate board and the main payload was achieved with an XBee S-band radio link.

5.2.6 Lightning, cloud and precipitation data sources

Because it is vital to know when measurements are taken under fair-weather conditions, we used additional datasets to assess meteorological conditions near each payload. Thunderstorm regions were located by the World Wide Lightning Location Network (WWLLN) *Dowden et al.* [2002], which senses lightning sferics in the VLF frequency band, and the Geostationary Lightning Mapper (GLM) instrument on the GOES-17 satellite [*Goodman et al.*, 2013; *Peterson*, 2019], which senses lightning flashes at 777.4 nm. Because neither lightning detection method has 100% detection efficiency, and to check for the presence of non-thunderstorm weather that could cause electric field disturbances, we also checked for the presence of nearby convection and precipitation. We used infrared imagery from the Advanced Baseline Imager (ABI, C13 product) on GOES-17 to look for nearby vigorous convection activity. Cold brightness temperature in the images indicates high-altitude cloud tops, often an indicator for convective clouds [*Lindsey et al.*, 2012]. In order to identify nearby precipitation, which is frequently associated with electrified clouds that do not produce lightning, we used the Integrated Multi-Satellite Retrievals for GPM (IMERG) dataset[*Huffman et al.*, 2020].

5.3 Observations

5.3.1 2021 science flights

The balloon instruments, telemetry and trajectory plan were validated with test flights conducted in July and September 2019. Due to the onset of the COVID-19 pandemic in early 2020, no flights were possible that year; but science flights were successfully launched in June 2021.

The first balloon, hereafter referred to as Flight 1, was launched at 05:27 UT on June 25 (June 24 22:27 PDT). Once Flight 1's altitude exceeded about 30 km, it was carried generally westward at $10\text{-}20\,\mathrm{m\,s^{-1}}$. Flight 1 lost GPS lock for much of its initial ascent, but its latitude and longitude could be determined with significantly greater uncertainty (around $\pm 10\,\mathrm{km}$) from the Iridium network, and its altitude was estimated with an uncertainty of $\pm 1\,\mathrm{km}$ using a pressure altimeter. Once GPS lock was reestablished at 15:24 UT on June 25, altitude could be measured with an uncertainty of $\pm 0.1\,\mathrm{km}$.

Flight 2 was launched nearly 24 hours after Flight 1, at 04:47 UT on June 26 (June 25 21:47 PDT). Due to erratic surface wind, the lower vertical probe sphere on Flight 2 impacted a ground structure during launch, and became detached from the payload soon after. Vertical field measurements on Flight 2 could still be made by comparing the upper vertical probe potential to the mean of the horizontal probe potentials, but conductivity measurements by the lower probe were not possible. Flight 2 followed a similar trajectory to Flight 1 during its initial ascent. Both flights continued westward for several days.

By June 29, both flights were nearing the altitude floor below which they could not safely fly without interfering with commercial airline traffic, and the decision was made to terminated the flights. Flight 2 terminated successfully at 06:16 UT and splashed down at 06:40 UT. Flight 1 acknowledged the terminate command sequence, but its altitude following this time did not indicate a successful termination. Once the balloon dipped below the tropopause at about 11.8 km 13:40 UT, it quickly descended to sea level.

Electric fields and conductivities measured by both flights are presented along with their altitude profiles in Figure 5.1.

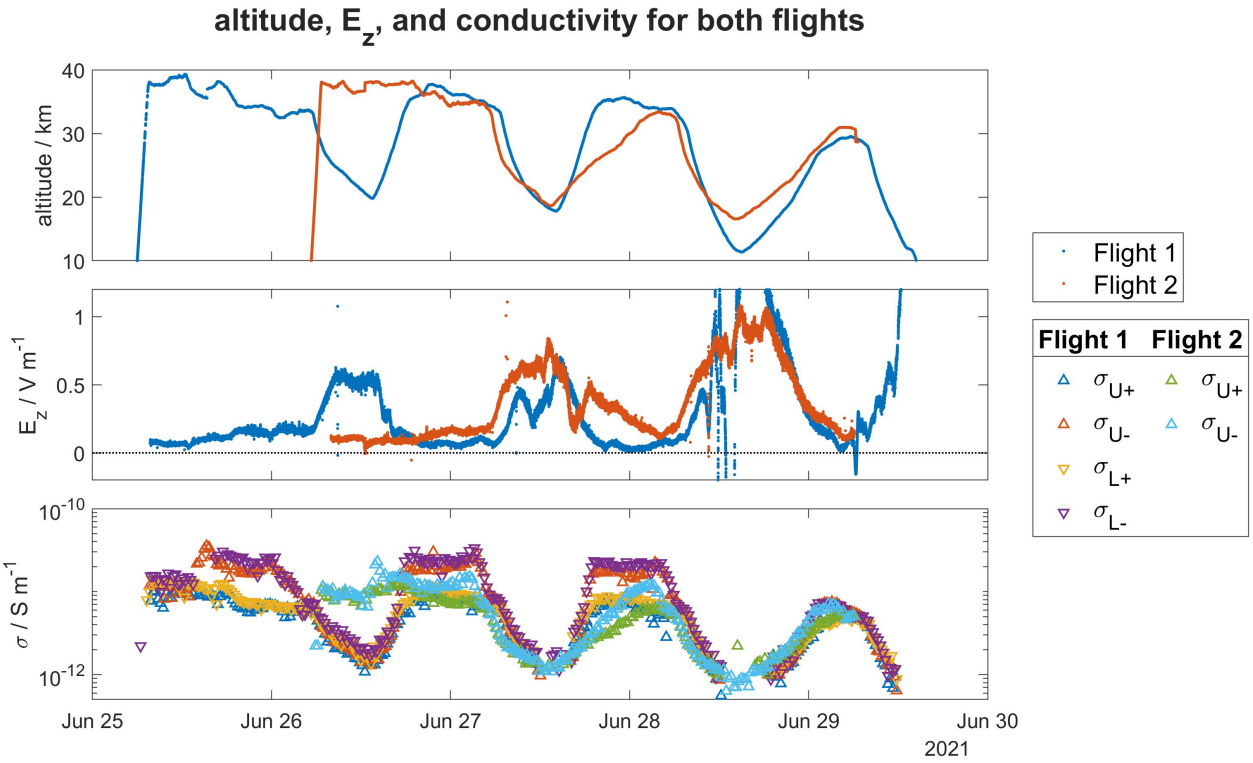

Figure 5.1: Vertical electric field (middle) and conductivity elements (bottom) measured by the two 2021 balloon flights, compared with altitude (top). Positive electric field values indicate the field oriented downwards, the expected fair-weather field direction.

5.3.2 Electric fields

Both flights measured electric fields that varied between 0.05 and 0.2 $\mathrm{V\,m^{-1}}$ at ceiling altitudes greater than 30 km, and up to 1 $\mathrm{V\,m^{-1}}$ at nightly altitude minima below 20 km. At these lower altitudes, the electrical conductivity was small enough (around $10^{-12}\,\mathrm{S\,m^{-1}}$) that the vertical probes were not able to relax to potentials dictated by the ambient field within the conductivity measurement time, and relaxation artifacts are seen in the subsequent electric field measurements.

Flight 1, which carried two vertical and two horizontal probes, was used to compare different measures of the vertical electric field. Each probe potential was measured relative to the gondola ground plates, and the differences between the vertical probes and the horizontal probes was also measured directly. Hence, the following measurements of the vertical electric field are possible:

1. upper vertical to gondola ground: V_1/L
2. lower vertical to gondola ground: $-V_2/L$
3. upper vertical minus lower vertical: $(V_1 - V_2)/2L$
4. vertical difference: $(V_{\mathrm{diff}})/2L$
5. upper vertical minus the average of the horizontals: $(V_1 - (H_1 + H_2)/2)/L$
6. average of the horizontals minus the lower vertical: $((H_1 + H_2)/2 - V_2)/L$

where L is the distance between the center of either vertical probe and the center of the gondola, equal to 1.56 m. Several of these vertical electric field measurements are compared in Figure 5.2.

While the first two vertical field measurement techniques are the simplest, any common-mode charging of the gondola relative to the probes (e.g. from electron photoemission or vertical air motion during ascent and descent) will result in a gondola ground potential that is not halfway between the upper and lower probe potentials. The potential difference between the upper vertical probe and gondola (1) will then not be equal to the difference between the gondola and lower probe potentials (2), and neither of these will produce an accurate representation of the vertical electric field. Common-mode charge effects can be eliminated by using the potential difference between the two vertical probes, obtained either by differencing the two probe potentials (3) or directly from the differential amplifier (4).

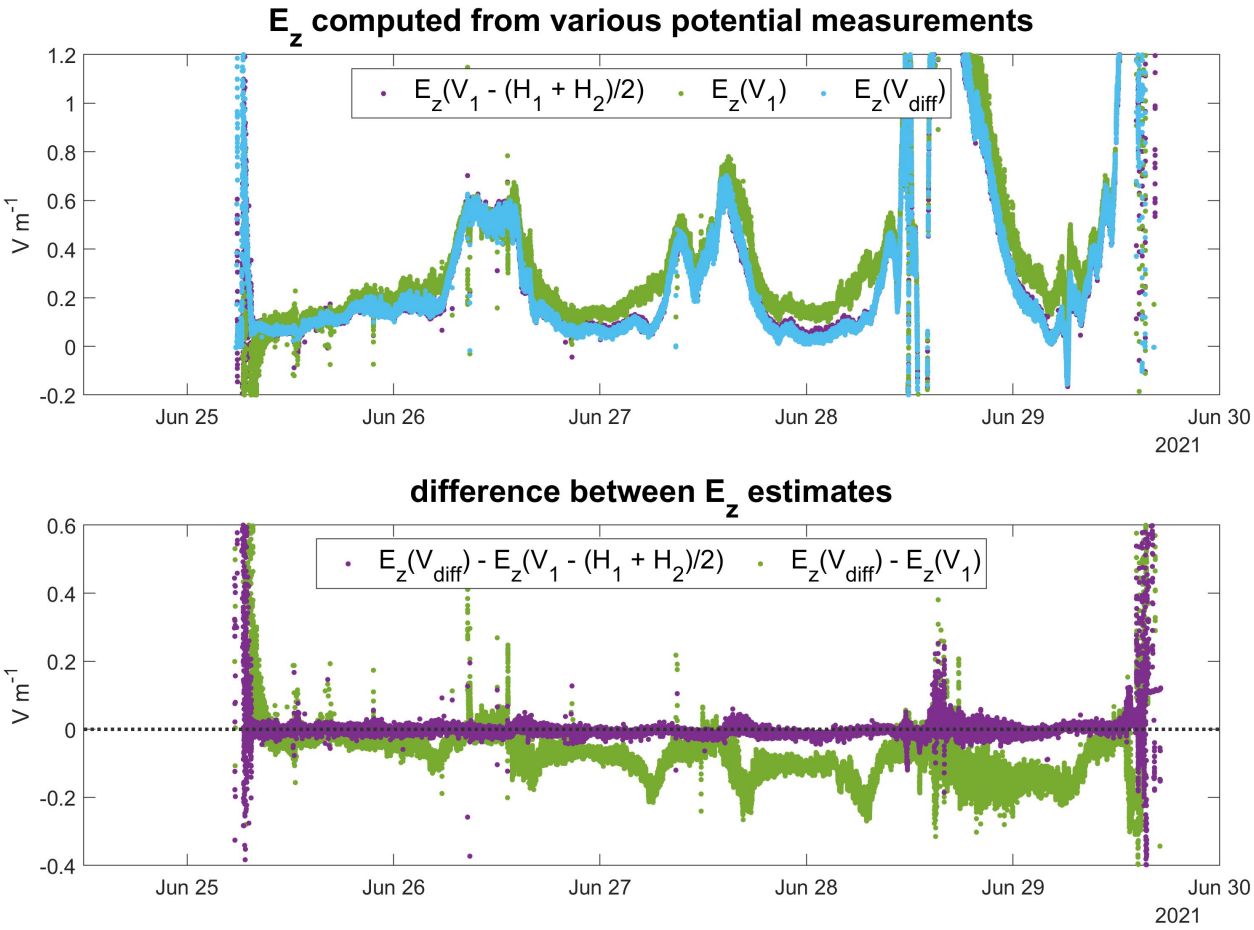

Figure 5.2: E_z estimates from different potential measurements (top), and the difference of the electric field computed using the upper vertical probe and the average potential of the horizontal probes, and just the upper vertical probe, from the electric field computed using the potential difference from the upper and lower vertical probes.

For the purposes of calculating the vertical electric fiend and vertical current density on Flight 2, which was missing its lower vertical probe, the potential difference between the upper probe (V_1) and the average of the horizontal probes ($(H_1 + H_2)/2$) was used (5). This field estimate was found to agree well with that found using either of the difference techniques, as shown in Figure 5.2. Electric field and vertical current densities for Flight 1 were determined using the (V_{diff}) potential difference.

Electric field data were filtered to remove contamination by recent conductivity bias relaxation measurements. Because the conductivity varied exponentially with altitude, the impacted data were altitude dependent: below 20 km, the long relaxation time constant resulted in conductivity measurements impacting electric field measurements up to three minutes after the conductivity measurement. These contaminated

data were removed using the following procedure:

1. At altitudes above 20 km: E_z measurements made immediately after conductivity measurements were removed, defined as being within the same packet as the conductivity measurement ($\mod$ (sequence number, 10) = 0) AND index in packet > 3

2. At lower altitudes: E_z measurements with $\mod$ (sequence number, 10) $= 0, 1, 2$ were removed.

The only known electric field measurement errors resulted from the measurement precision of the probe and difference op-amps. After calibrating each payload's set of instruments with known probe and gondola potentials as inputs, and correcting for systematic errors that impacted the output reading when $0\,\mathrm{V}$ was applied across the probes, each payload was determined to measure probe potentials accurate to about $1\,\mathrm{mV}$, and therefore electric fields to within about $1\,\mathrm{mV\,m^{-1}}$.

5.3.3 Conductivity

The payloads measured conductivity using both positive and negative bias potentials, for which the charge carriers are negative and positive ions, respectively. We will refer to these conductivity elements by their bias potentials. Conductivity elements measured by both the upper and lower probes of Flight 1, and the upper probe of Flight 2, are shown in the bottom panel of Figure 5.1. Conductivity varied exponentially with altitude. Additionally, measured positive and negative conductivity differed during the day. This difference is due to photoemission of electrons from the metal probe spheres, which enhances the apparent negative conductivity, as photoelectrons are repelled by the negative potential of the probe sphere. Photoemission does not significantly impact the positive conductivity, photoelectrons are immediately drawn back to the positively-charged probe sphere after being emitted.

Noting that conductivity should primarily depend on altitude, and not change quickly in time otherwise, we fit an altitude profile to the nighttime conductivity measurements, which should not have been impacted by electron photoemission. Conductivity could then be estimated directly from the altitude of each payload. Conductivity elements are plotted with altitude, along with the profile fit functions, in Figure 5.3.

Conductivity elements were filtered to remove outliers and errors using the following procedure:

1. Remove conductivity measurements that satisfy any of the following:

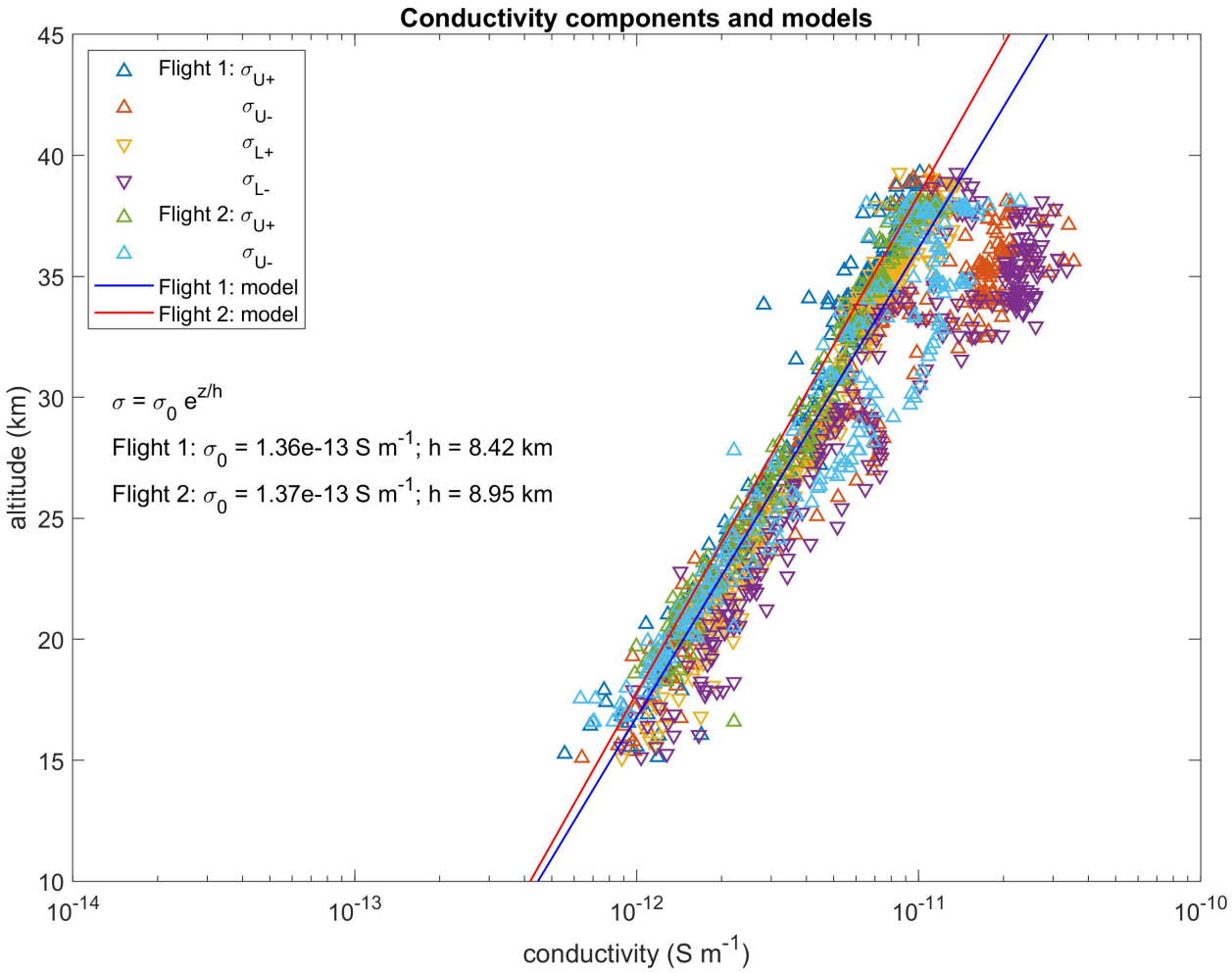

Figure 5.3: Conductivity elements as a function of altitude, and profile fit functions. Note the separation between positive- (blue, yellow, green) and negative-bias (red, purple, cyan) conductivity elements at higher altitudes, which were typically achieved during the day.

(a) exponential fit root-mean-squared error (RMSE) > 0.05

(b) altitude below 14.9 km

(c) conductivity below 5×10^{13} S/m

2. Remove from altitude model fit measurements that satisfy any of the following:

(a) altitude below 20 km, or above 30 km

(b) solar elevation angle > horizon elevation angle - $0.83°$, that is, any part of the solar disk above the horizon.

Note that Figure 5.3 does not include conductivity elements that were removed in step 1, but includes elements not used to generate the altitude fit profiles, in order to show separation of positive and negative conductivity elements due to photoemission.

There are two important factors to consider that impact the error in conductivity element estimates: the error in each relaxation curve fit, and the difference in each conductivity measurement from the altitude-derived model. Estimates of each of these error factors are given in Figure 5.4. Conductivity measurement outliers previously filtered as described above are not included in this figure. The error in each relaxation curve fit, defined as the width of the 95% confidence bounds of the conductivity element relative to the element estimate itself, typically varies between 10 and 20%. The difference of each conductivity element estimate from the altitude model, relative to the conductivity element estimate, is typically between 10 and 30% for nighttime and positive-bias conductivity elements, but may be significantly larger for daytime negative-bias conductivity elements due the effect of photoemission.

5.3.4 Vertical current density

Vertical current density is obtained by multiplying the vertical electric field by the total electrical conductivity. For each payload, we took the ten-minute moving mean of the vertical electric field measurements, and multiplied this by the estimated conductivity at the payload altitude based on the conductivity profiles described in section 5.3.3. The resulting estimates of vertical current density measured by both Flight 1 and Flight 2 are shown in Figure 5.5. Vertical current density at each payload varied between 0.5 and $2.5\,\mathrm{pA\,m^{-2}}$.

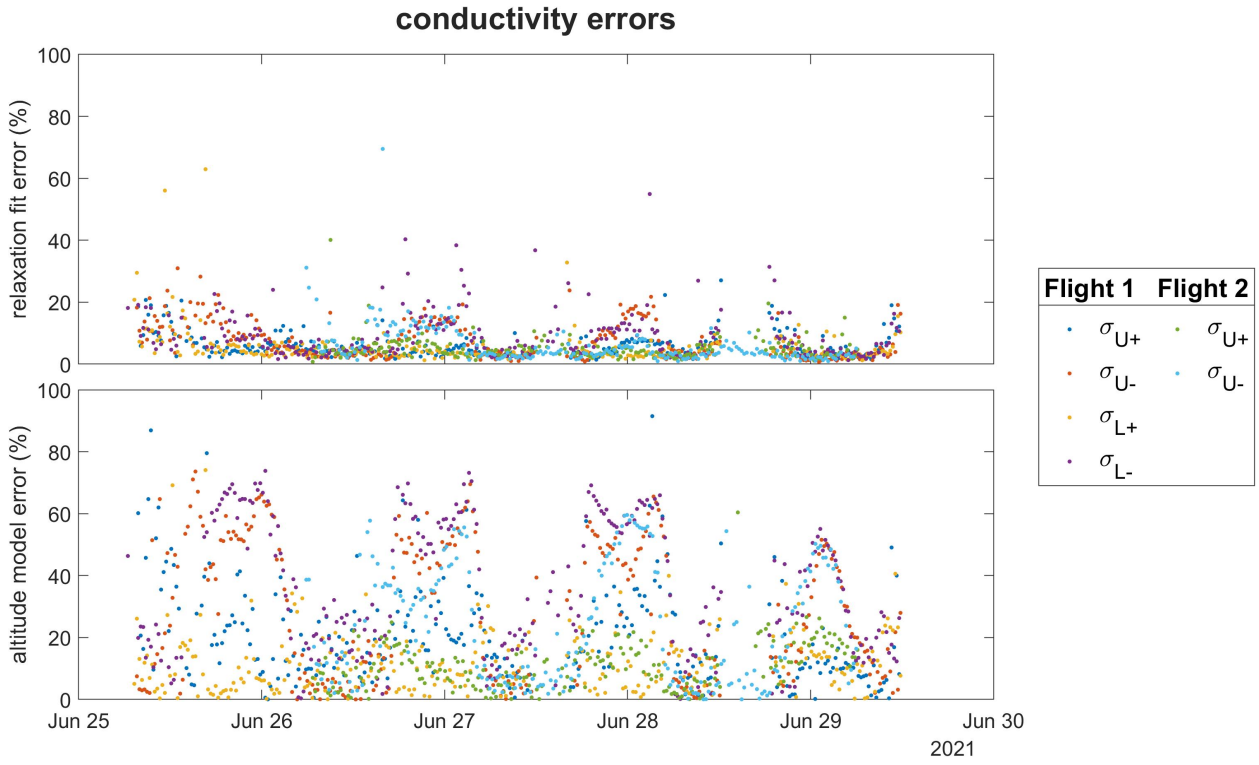

Figure 5.4: Conductivity error from relaxation curve fits (top) and relative to the altitude-derived conductivity model (bottom). The relaxation curve fit error is defined as the width of the 95% confidence interval of the conductivity element, relative to the conductivity element estimate. The error from the altitude-derived conductivity model is the absolute value of the difference between the conductivity element estimate and the altitude model of this element, divided by the conductivity element estimate.

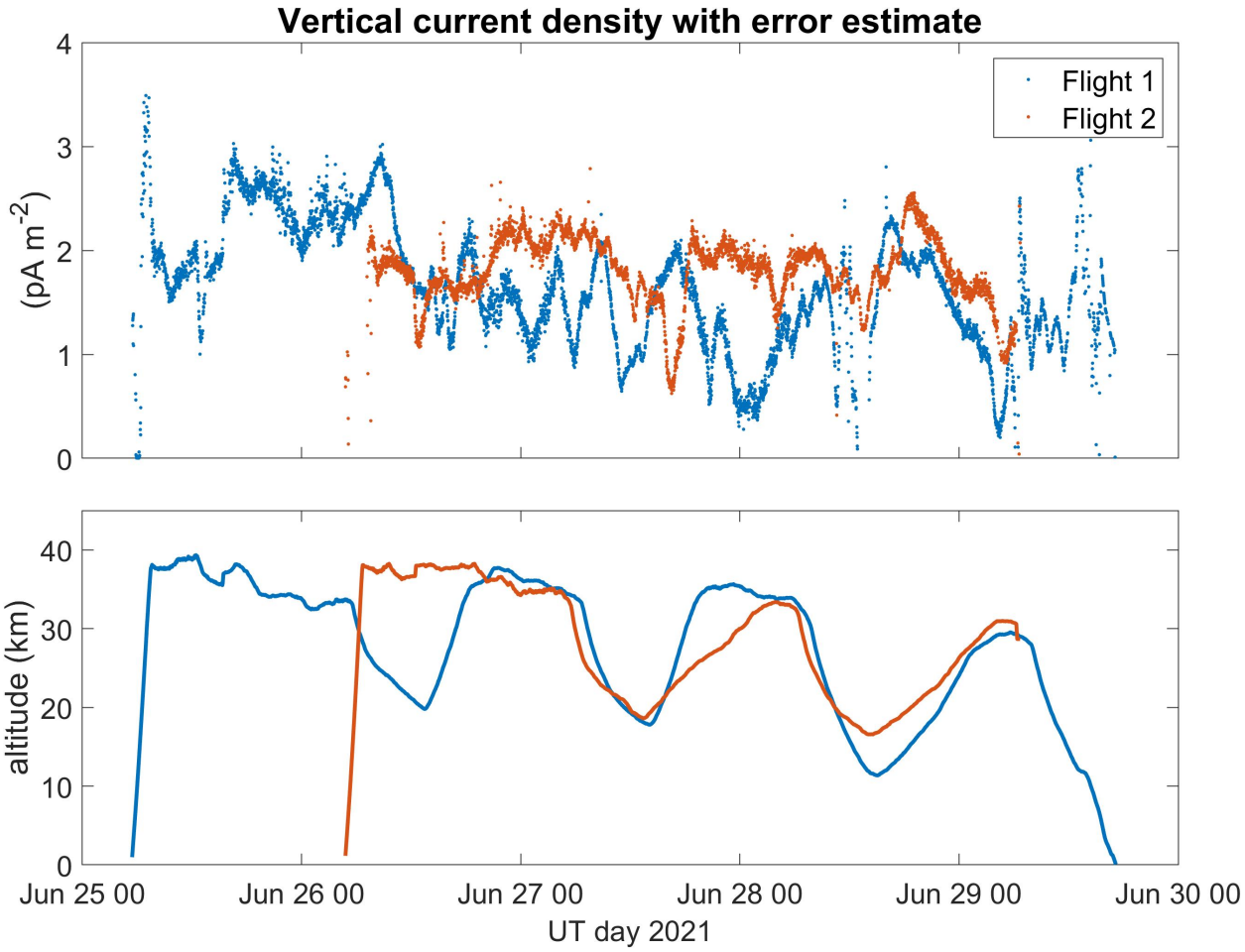

Figure 5.5: Vertical current density estimates from Flight 1 and Flight 2, obtained from 1-minute averages of vertical electric field and altitude-derived conductivity estimates.

Errors in the electric field and conductivity measurements add to give the vertical current density error. However, as the conductivity relative error is significantly greater than the electric field relative error (about 20-30% vs. about 0.1-1%), most of the error in the current density is due to errors in the conductivity measurement and model. We therefore expect the current density relative error to be comparable to that of the conductivity measurements, of around 20-30%; for a nominal current density of $2\,\mathrm{pA\,m^{-2}}$, this corresponds to about $0.5\,\mathrm{pA\,m^{-2}}$.

5.4 Discussion

Both Flight 1 and Flight 2 measured electric fields and conductivity that followed expectations. Vertical electric field decreased exponentially with increasing altitude between 0.1-$1\,\mathrm{V\,m^{-1}}$, except during launch and at very low altitude. Conductivity increased exponentially with increasing altitude, and generally varied between 10^{-12} and $10^{-11}\ \mathrm{S\,m^{-1}}$, although conductivity fits were less accurate at lower altitudes. The resulting vertical current density, obtained by multiplying vertical electric field with total conductivity, varied between 0.5 and $2\,\mathrm{pA\,m^{-2}}$, in agreement with previous work *Roble* [1991]; *Williams* [2009]; *Siingh et al.* [2007]. That the measurements from each payload agreed with previous work, and also agreed with input potentials during the calibration process and during conductivity measurements, suggests the instruments were functioning as designed.

However, although the vertical current estimates from each payload fall within the expected range, simultaneous measurements by the two payloads show significant differences, contrary to expectations. Previous work *Holzworth et al.* [1984] suggested that simultaneous measurements of the GEC vertical return current density made by distant stratospheric balloons would agree to within 20%, so long as neither balloon were near a thunderstorm or other atmospheric electric field disturbance. That work used long-duration superpressure balloons, which had a lower peak altitude than our zero-pressure balloons, but were able to persist at more constant altitudes than our balloons. Nevertheless, even at times when both our balloons were at similar altitudes (such as June 26 19:00 UT to June 27 05:00 UT, during which both balloons had stable altitude near 35km), one payload might measure as much as double the vertical current density measured by the other payload.

We can confirm that neither balloon flew near thunderstorms by comparing the balloon trajectories with lightning strokes recorded by WWLLN. Figure 5.6 shows the balloon tracks plotted with WWLLN lightning strokes and GLM groups, colored according to time. Note that the only storm near the balloon tracks began in the last hours of June 27 (UT), by which time both balloons were at least 1500 km to the west. Sparse lightning is seen within 1000 km of balloon locations at several times during the flights, but significant lightning is not observed within 1000 km of either balloon for most of the flights.

Neither GLM nor WWLLN detects the presence of electrified shower clouds (ESCs), which do not produce lightning, but may impact the stratospheric current density. We can check for the presence of

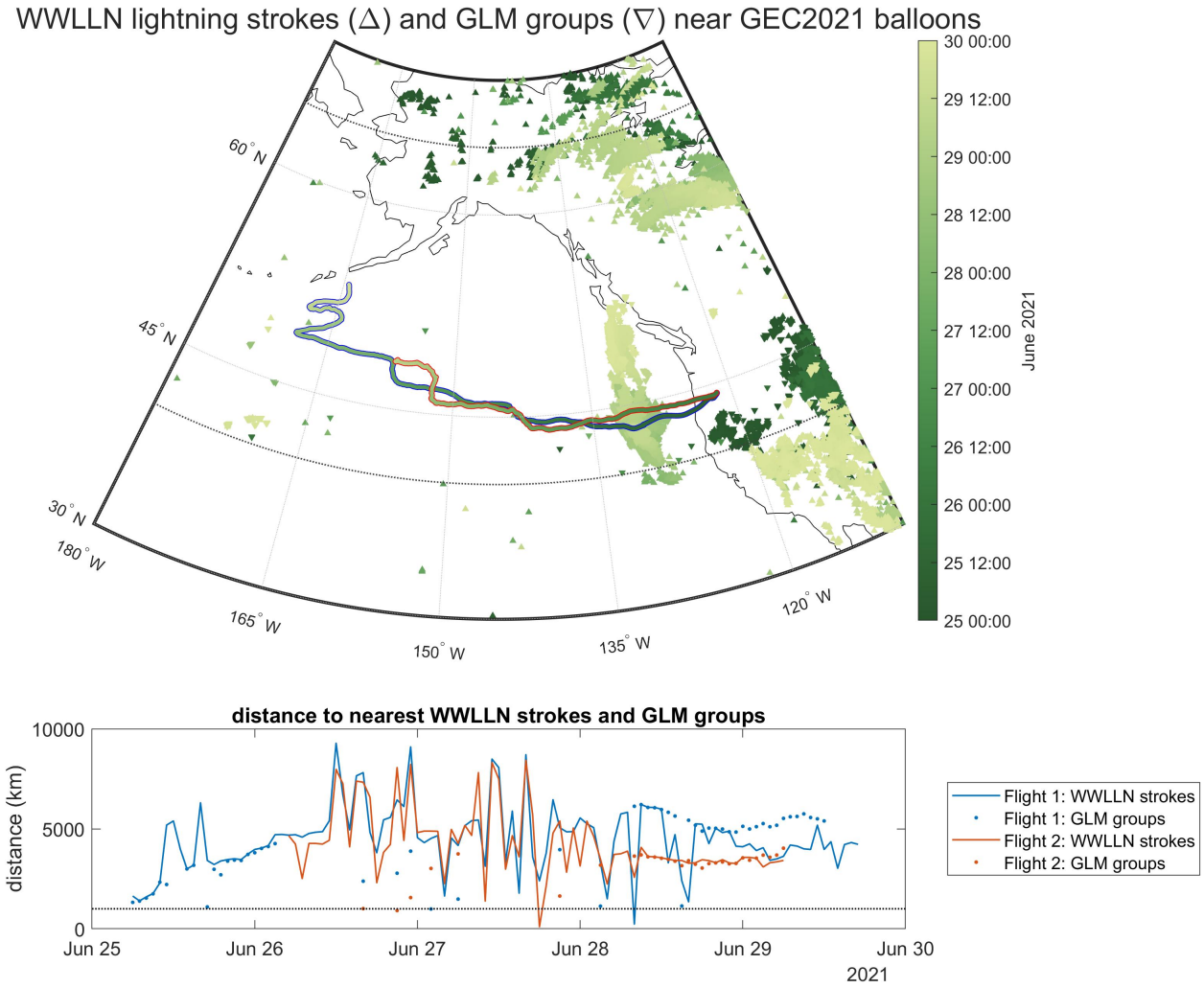

Figure 5.6: (upper) Flight 1 (blue exterior trace) and Flight 2 (red exterior trace) ground tracks plotted with lightning strokes recorded by WWLLN. The interiors of the traces are colored according to time, shown in the colorbar on the right. WWLLN stroke locations are plotted as Δ, while GLM groups are plotted as ∇ also colored according to time. GLM groups are only plotted between $40°$ and $65°$ N, indicated by the dashed parallels. (lower) Hourly time series of distance to the lightning stroke and GLM group nearest to each flight. The horizontal dashed line marks 1000 km distance between strokes/groups and the flights.

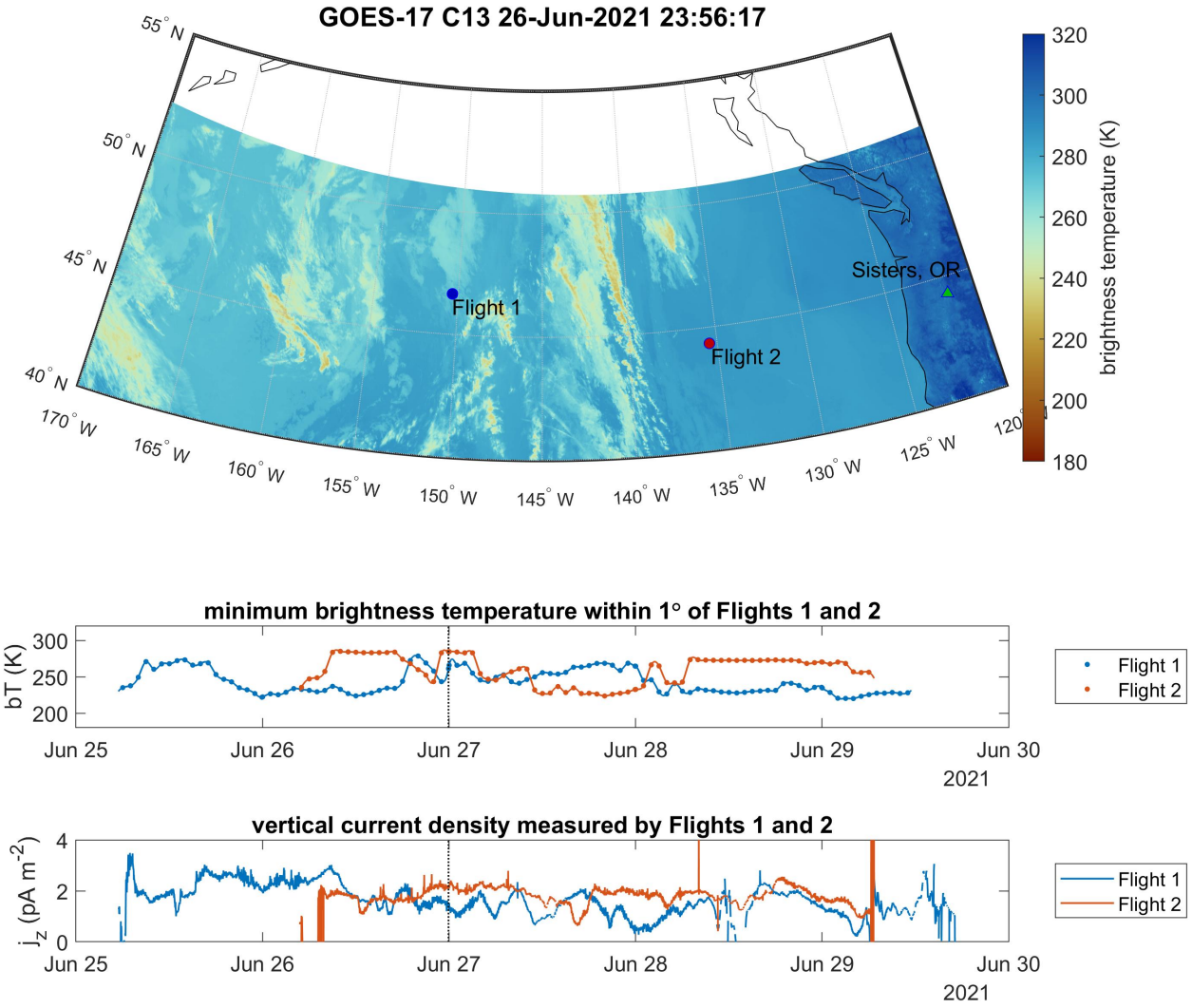

Figure 5.7: (upper) an example GOES C13-derived brightness temperature map with the locations of Flight 1 (blue circle) and Flight 2 (red circle) shown. (lower) Time series of mean brightness temperature within 1° of each balloon.

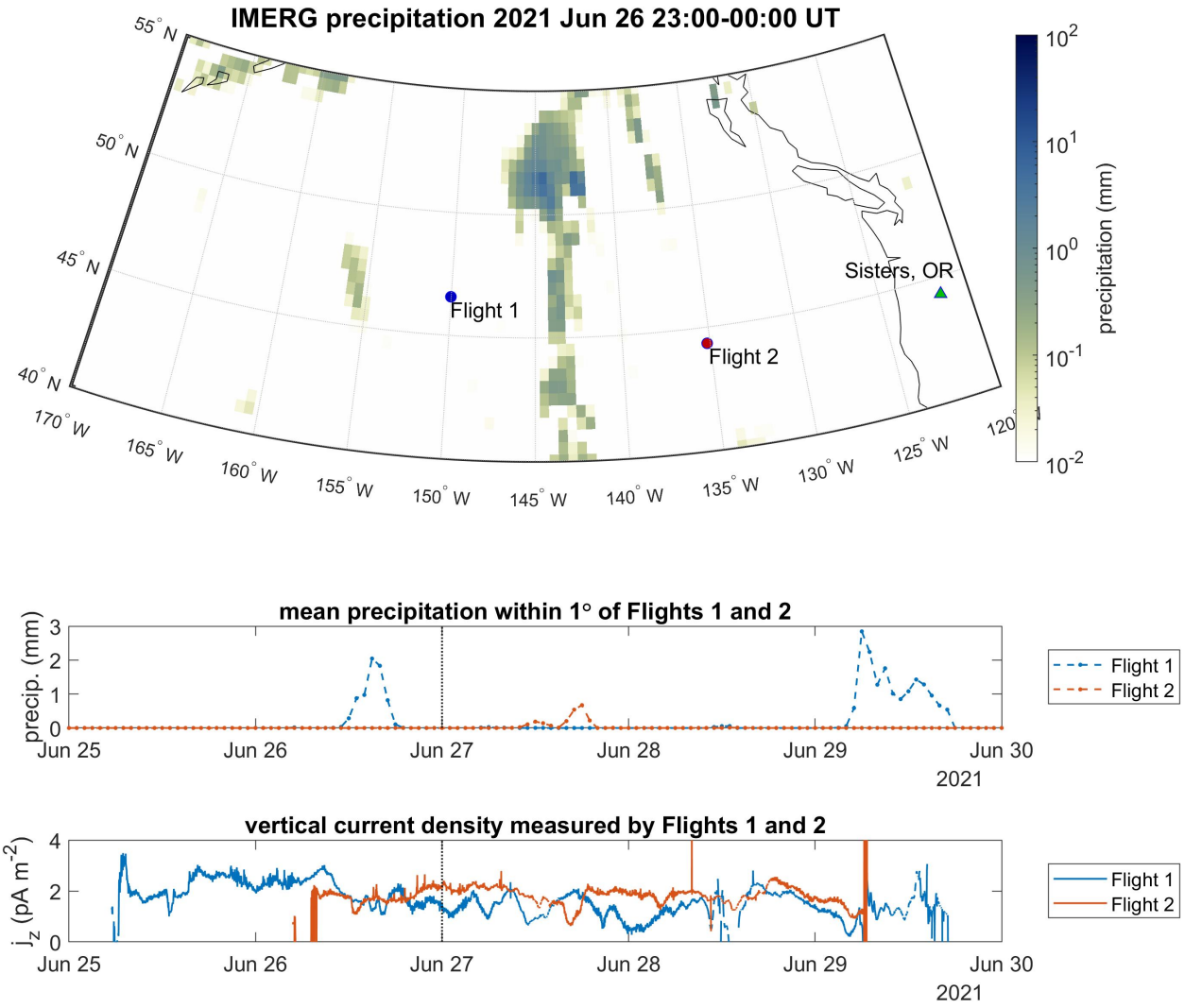

Figure 5.8: (upper) an example IMERG precipitation map with the locations of Flight 1 (blue circle) and Flight 2 (red circle) shown. (lower) Time series of mean precipitation within 1° of each balloon.

clouds and precipitation near the balloons using GOES C13 brightness temperature as a proxy for cloud top height [*Lindsey et al.*, 2012], and the Integrated MultisatellitE Retrievals for GPM (IMERG) dataset to quantify precipitation [*Huffman et al.*, 2020]. Figure 5.7 shows GOES C13 brightness temperature at an example time during the flights, along with the mean brightness temperature near each balloon over the entire flight period; Figure 5.8 shows IMERG precipitation at an example time during the flight, along with the mean precipitation near each balloon over the entire flight period.

Both balloons experienced significant changes in their nearby cloud and precipitation environments during their flights, which is sometimes evident in the vertical current density measurements; for example, Flight 2 measured a decrease in the fair-weather return current density late on June 27, corresponding to an increase in precipitation nearby. However, both balloons should have been optimally positioned to measure the GEC vertical current density during the period of June 26 18:00 UT - June 27 06:00 UT. During this time, both balloons were at nearly constant, high altitudes, where changes in vertical current density should be dominated by changes in the vertical electric field, rather than changes in conductivity. The mean brightness temperature nearby was warm, indicating an absence of high-altitude clouds; and there was no precipitation recorded within 1 degree. Despite this, the vertical current densities measured by the two balloons differed by as much as a factor of 2. This discrepancy represents a major difference from the expected result, based on measurements from the EMA campaigns, which found agreement to within about 20% of electric field measurements made simultaneously on separate balloons.

There are several important differences between this balloon campaign and the EMA campaigns. First, EMA used long-duration superpressure, rather than zero-pressure balloons; although vertical current in a given column of the fair-weather atmosphere should be invariant with altitude, it is possible our balloons experienced charging during diurnal ascent and descent that impacted electric field and conductivity measurements. However, the flights presented here flew at stable high altitude for several multi-hour periods, during which any charge accumulation from the ascent would have had time to equilibrate; during these times, our flights would have had similar charge conditions to the EMA flights.

Second, the EMA campaign balloons were launched from Christchurch, New Zealand, and flew over the Southern Ocean. As the Southern Ocean has much different circulation and cloud characteristics than the North Pacific, it is not difficult to imagine that atmospheric electrical effects in these regions could be

impacted differently by both thunderstorm and fair-weather properties.

5.5 Summary

We expected that distant measurements of the fair-weather vertical current density in the stratosphere would agree, in keeping with prior work *Holzworth et al.* [1984]. One of the two balloon payloads, Flight 2, lost its lower vertical probe during launch. Despite this, we were able to validate several methods for measuring the vertical electric field without the lower vertical probe using Flight 1's measurements, and thus we expect both balloons were able to measure atmospheric electricity as intended. We compared several methods of measuring the vertical electric field on the undamaged payload, and verified that the measurement method used on the damaged payload agreed well with the planned measurement scheme. Further, each conductivity measurement included steps where the upper probe was biased to known potentials; that the measured bias potentials matched nominal values supports the validity of Flight 2's measurements. The range of electric field and conductivity measured at each balloon matched expectations from prior work. Combining these, each balloon measured a vertical current density that varied between 0 and $2\,\mathrm{pA\,m^{-2}}$.

Vertical current density measured by Flight 1 did not agree with the measurement by Flight 2. To eliminate the possibility of contamination by nearby storms, we checked for lightning, high-altitude clouds, and precipitation. For the most part, neither WWLLN nor GLM detected lightning near either balloon during the flights. Both balloons passed above regions of relatively cold cloud-top brightness temperature, as measured in the GOES C13 channel; as well as regions of significant precipitation reported by IMERG. During the period of June 26, 18:00 UTC to June 27, 06:00 UTC, there is no recorded lightning or precipitation near either balloon, and the minimum cloud-top temperature is warm, indicating that both balloons should be measuring the fair-weather electrical environment during this time. Additionally, both balloons are at relatively stable, high altitude during this time, so the electrical conductivity should not change significantly at each balloon. Despite these ideal measurement conditions, the measurements of vertical current density at each balloon varied substantially during this period.

There are several possible explanations for the difference between each payload's measurements. One is that the damage to the Flight 2 payload was more substantial than expected, and some electrical error resulted in unreliable electric field measurements. However, the conductivity measurement via the relaxation curve technique makes use of accurate potential measurements, and Flight 2 measured comparable bias and relaxation potentials with its upper probe to those measured by Flight 1. Based on our analysis, the damage

to Flight 2 appears to have been isolated to the lower probe itself, and measurements made by the other probes should not have been impacted. The only apparent loss to Flight 2's functionality are higher electric field errors, due to the shorter vertical distance between probes, and loss of redundancy in the electric field and conductivity measurements.

Another possible explanation for this discrepancy is that we have failed to account for the perturbative impacts of lightning, clouds or precipitation that affected one or both payloads. Although neither flight appeared to overfly significant lightning, convection or precipitation, lightning detection methods miss some lightning, and perhaps clouds near the flights produced more significant electric fields than expected. Our best estimates of nearby lightning, convection and precipitation indicate that this was not the case, however.

Alternatively, it is possible that the long-held assumption that the stratospheric fair-weather return current is generally spatially invariant is not as valid as previously believed. This assumption is supported by measurements from the EMA multi-flight balloon campaigns [*Holzworth et al.*, 1984; *Norville and Holzworth*, 1987], but these campaigns had several key differences from the one presented here. In particular, differences in ocean and atmospheric circulation over the northern Pacific Ocean, where our flights were located, and the Southern Ocean, where EMA flew, may result in disparities in fair-weather conditions between and within these regions.

This work concludes with several directions in which next steps could be taken. One is to use the measurements of electric fields, conductivities and current densities presented here to inform a model study of GEC drivers and variability. In particular, extraterrestrial drivers have not been given much consideration as potential causes for the measured spatial inhomogeneity of the return current density; although there were no strong solar flares during the flight period, higher-latitude impacts such as electron microbursts could have played an important role in determining the electrical conditions at both balloons [*Borovsky*, 2017].

Additionally, this work was undertaken in concert with an effort to quantify instantaneous global thunderstorm activity, in order to compare this quantity with the fair-weather current density. Although the differences between the two flights' measurements will complicate this effort, perhaps careful comparison of a global thunderstorm activity proxy, validated by comparison to ground-based electric field measurements, with each flight's measurements could determine conclusively whether one flight's measurements

were erroneous, or better elucidate the sources of spatial homogeneity in the fair-weather return current.

Chapter 6

Conclusions and directions for future work

We have examined the lower ionosphere response to two types of space weather phenomena, solar flares and energetic electron precipitation, with an eye towards resolving changes in their signatures on the lower ionosphere in time. In Chapter 3, we showed that both onset timing and size of the subsolar attenuation region during two X-class solar flares could be determined by comparing the most recent sferic propagation path distribution with a trailing median path distribution. In Chapter 4, we extended this path analysis technique to incorporate sferic dispersion information, used a nominal path distribution derived from days with little electron precipitation, and demonstrated that increases in sferic dispersion agreed well with increased precipitating electron flux measured in polar-orbiting spacecraft.

The techniques presented in these chapters represent new ways to study ionospheric processes using established sensor networks. Although the main results thus far are qualitative, we presented several possible extensions to these techniques that would allow for quantitative estimates of lower ionospheric conditions using sferic dispersion. For cases where computation time is not a limiting factor, performing a mode-theory model inversion on each measured sferic dispersion fit would allow for accurate determination of ionosphere height along each propagation path. A range of faster and less precise techniques are possible, including precomputation of simulated sferic dispersion on a grid, to which measured dispersion could be compared; or, an empirically-derived correction factor could be applied directly to measured dispersion to find the ionosphere height.

The general method of computing statistics of variables at grid locations is computationally expedient

and sufficient to demonstrate the promise of ionosphere remote sensing using WWLLN paths and sferics. However, many improvements on this method are possible, including implementation of code that retains the full distributions of path and sferic properties on the grid, rather than the statistics of these distributions; methods to address weighting of disparate populations of paths traversing grid locations; and techniques for assigning paths and sferics to grid locations that take into account the distance of each path from the grid center. Future investigations making use of tomographic methods may significantly improve on the accuracy and quantitative value of this work.

Additionally, we reported on a stratospheric balloon campaign to investigate spatial variability in the fair-weather return current of the global electric circuit. In Chapter 5, we described simultaneous measurements of vertical electric fields and electrical conductivity by two instrumented balloons separated by $\sim 1000\,\mathrm{km}$. Contrary to the long-held expectation that the vertical current density is spatially invariant in fair weather, our measurements showed significant variation of up to a factor of 2 in the current density measured by the two balloon payloads. Despite damage to one payload, we validated each payload's measurements using multiple methods for determining the vertical electric field, and ensured there was no significant lightning, convection, or precipitation near either payload for most of the flight times.

The disparity in return current density measured by each payload suggests that this parameter is not spatially invariant in fair weather as previously believed. While the key motivation of this work remains to quantify the relative importance in global drivers to the fair-weather return current, it is now clear that the causes of regional variability in the fair weather return current must be investigated in order to address relationships between global drivers to the circuit.

Bibliography

Anderson, B. R., S. Shekhar, R. M. Millan, A. B. Crew, H. E. Spence, D. M. Klumpar, J. B. Blake, T. P. O'Brien, and D. L. Turner (2017), Spatial scale and duration of one microburst region on 13 August 2015, *Journal of Geophysical Research: Space Physics*, *122*(6), 5949–5964, doi:10.1002/2016JA023752, _eprint: https://onlinelibrary.wiley.com/doi/pdf/10.1002/2016JA023752.

Anderson, T. S., M. P. McCarthy, and R. H. Holzworth (2020), Detection of VLF Attenuation in the Earth-Ionosphere Waveguide Caused by X-Class Solar Flares Using aGlobal Lightning Location Network, *Space Weather*, *18*(3), e2019SW002,408, doi:10.1029/2019SW002408, _eprint: https://onlinelibrary.wiley.com/doi/pdf/10.1029/2019SW002408.

Andersson, M. E., P. T. Verronen, C. J. Rodger, M. A. Clilverd, and A. Seppälä (2014), Missing driver in the Sun-Earth connection from energetic electron precipitation impacts mesospheric ozone, *Nature Communications*, *5*, doi:10.1038/ncomms6197, publisher: Nature Publishing Group.

Arsenovic, P., E. Rozanov, A. Stenke, B. Funke, J. M. Wissing, K. Mursula, F. Tummon, and T. Peter (2016), The influence of Middle Range Energy Electrons on atmospheric chemistry and regional climate, *Journal of Atmospheric and Solar-Terrestrial Physics*, *149*, 180–190, doi:10.1016/j.jastp.2016.04.008.

Asikainen, T., and M. Ruopsa (2019), New Homogeneous Composite of Energetic Electron Fluxes From POES Satellites: 1. Correction for Background Noise and Orbital Drift, *Journal of Geophysical Research: Space Physics*, *124*(2), 1203–1221, doi:10.1029/2018JA026214, _eprint: https://onlinelibrary.wiley.com/doi/pdf/10.1029/2018JA026214.

Barr, R., D. L. Jones, and C. J. Rodger (2000), ELF and VLF radio waves, *Journal of Atmospheric and Solar-Terrestrial Physics*, *62*(17), 1689–1718, doi:10.1016/S1364-6826(00)00121-8.

Berland, G. D., R. A. Marshall, C. Martin, J. Buescher, R. A. Kohnert, S. Boyajian, C. M. Cully, M. P. McCarthy, and W. Xu (2023), The atmospheric X-ray imaging spectrometer (AXIS) instrument: Quantifying energetic particle precipitation through bremsstrahlung X-ray imaging, *Review of Scientific Instruments*, *94*(2), 023,103, doi:10.1063/5.0127272.

Bilitza, D., M. Pezzopane, V. Truhlik, D. Altadill, B. W. Reinisch, and A. Pignalberi (2022), The International Reference Ionosphere Model: A Review and Description of an Ionospheric Benchmark, *Reviews of Geophysics*, *60*(4), e2022RG000,792, doi:10.1029/2022RG000792, _eprint: https://onlinelibrary.wiley.com/doi/pdf/10.1029/2022RG000792.

Bland, E., F. Tesema, and N. Partamies (2021), D-region impact area of energetic electron precipitation during pulsating aurora, *Annales Geophysicae*, *39*(1), 135–149, doi:10.5194/angeo-39-135-2021, publisher: Copernicus GmbH.

Bland, E., T. Bozóki, and N. Partamies (2022), Spatial extent of the energetic electron precipitation region during substorms, *Frontiers in Astronomy and Space Sciences*, *9*.

Borovsky, J. E. (2017), Electrical conductivity channels in the atmosphere produced by relativistic-electron microbursts from the magnetosphere, *Journal of Atmospheric and Solar-Terrestrial Physics*, *155*, 22–26, doi:10.1016/j.jastp.2017.01.004, publisher: Elsevier Ltd.

Bouderba, Y., S. NaitAmor, and M. Tribeche (2016), Study of the solar flares effect on VLF radio signal propagating along NRK-ALG path using LWPC code, *Journal of Geophysical Research: Space Physics*, *121*(7), 6799–6807, doi:10.1002/2015JA022233, _eprint: https://onlinelibrary.wiley.com/doi/pdf/10.1002/2015JA022233.

Capannolo, L., W. Li, Q. Ma, L. Chen, X.-C. Shen, H. E. Spence, J. Sample, A. Johnson, M. Shumko, D. M. Klumpar, and R. J. Redmon (2019), Direct Observation of Subrelativistic Electron Precipitation Potentially Driven by EMIC Waves, *Geophysical Research Letters*, *46*(22), 12,711–12,721, doi:10.1029/2019GL084202, _eprint: https://onlinelibrary.wiley.com/doi/pdf/10.1029/2019GL084202.

Capannolo, L., W. Li, H. Spence, A. T. Johnson, M. Shumko, J. Sample, and D. Klumpar (2021), Energetic Electron Precipitation Observed by FIREBIRD-II Potentially Driven by EMIC Waves: Location, Extent, and Energy Range From a Multievent Analysis, *Geophysical Research Letters*, *48*(5), e2020GL091,564, doi:10.1029/2020GL091564, _eprint: https://onlinelibrary.wiley.com/doi/pdf/10.1029/2020GL091564.

Carvalho, F. L., M. A. Uman, D. M. Jordan, J. D. Hill, S. A. Cummer, D. A. Kotovsky, and R. C. Moore (2017), Triggered lightning sky waves, return stroke modeling, and ionosphere effective height, *Journal of Geophysical Research: Atmospheres*, *122*(6), 3507–3527, doi:10.1002/2016JD026202, _eprint: https://onlinelibrary.wiley.com/doi/pdf/10.1002/2016JD026202.

Chilton, C. J., F. K. Steele, and E. B. Norton (1963), Very-Low-frequency phase observations of solar flare ionization in the D region of the ionosphere, *Journal of Geophysical Research (1896-1977)*, *68*(19), 5421–5435, doi:10.1029/JZ068i019p05421, _eprint: https://onlinelibrary.wiley.com/doi/pdf/10.1029/JZ068i019p05421.

Clilverd, M. A., C. J. Rodger, N. R. Thomson, J. B. Brundell, T. Ulich, J. Lichtenberger, N. Cobbett, A. B. Collier, F. W. Menk, A. Seppälä, P. T. Verronen, and E. Turunen (2009), Remote sensing space weather events: Antarctic-Arctic Radiation-belt (Dynamic) Deposition-VLF Atmospheric Research Konsortium network, *Space Weather*, *7*(4), doi:10.1029/2008SW000412, _eprint: https://onlinelibrary.wiley.com/doi/pdf/10.1029/2008SW000412.

Codrescu, M. (2010), Global D-Region Absorption Prediction Documentation | NOAA / NWS Space Weather Prediction Center.

Crombie, D. (1965), On the use of VLF measurements for obtaining information on the lower ionosphere (especially during solar flares), *Proceedings of the IEEE*, *53*(12), 2027–2034, doi:10.1109/PROC.1965.4479, conference Name: Proceedings of the IEEE.

Cummer, S. A. (2000), Modeling electromagnetic propagation in the Earth-ionosphere waveguide, *IEEE Transactions on Antennas and Propagation*, *48*(9), 1420–1429, doi:10.1109/8.898776.

Cummer, S. A., U. S. Inan, and T. F. Bell (1998), Ionospheric D region remote sensing us-

ing VLF radio atmospherics, *Radio Science*, *33*(6), 1781–1792, doi:10.1029/98RS02381, _eprint: https://onlinelibrary.wiley.com/doi/pdf/10.1029/98RS02381.

Dowden, R. L., J. B. Brundell, and C. J. Rodger (2002), VLF lightning location by time of group arrival (TOGA) at multiple sites, *Journal of Atmospheric and Solar-Terrestrial Physics*, *64*(7), 817–830, doi: 10.1016/S1364-6826(02)00085-8.

Dowden, R. L., R. H. Holzworth, C. J. Rodger, J. Lichtenberger, N. R. Thomson, A. R. Jacobson, E. Lay, J. B. Brundell, T. J. Lyons, S. 0'Keefe, Z. Kawasaki, C. Price, V. Prior, P. Ortega, J. Weinman, Y. Mikhailov, O. Veliz, X. Qie, G. Burns, A. Collier, O. Pinto, R. Diaz, C. Adamo, E. R. Williams, S. Kumar, G. B. Raga, J. A. Rosado, E. E. Avila, M. A. Clilverd, T. Ulich, P. Gorham, T. J. Shanahan, T. Osipowicz, G. Cook, and Y. Zhao (2008), World-wide lightning location using VLF propagation in the Earth-ionosphere waveguide, *IEEE Antennas and Propagation Magazine*, *50*(5), 40–60, doi: 10.1109/MAP.2008.4674710, conference Name: IEEE Antennas and Propagation Magazine.

Ferguson, J. A. (1998), Computer Programs for Assessment of Long- Wavelength Radio Communications, Version 2.0.

Fisher, N. I. (1995), *Statistical Analysis of Circular Data*, Cambridge University Press, google-Books-ID: wGPj3EoFdJwC.

Gary, D. E., B. Chen, B. R. Dennis, G. D. Fleishman, G. J. Hurford, S. Krucker, J. M. McTiernan, G. M. Nita, A. Y. Shih, S. M. White, and S. Yu (2018), Microwave and Hard X-Ray Observations of the 2017 September 10 Solar Limb Flare, *The Astrophysical Journal*, *863*(1), 83, doi:10.3847/1538-4357/aad0ef, publisher: The American Astronomical Society.

Gasdia, F., and R. A. Marshall (2021), A New Longwave Mode Propagator for the Earth–Ionosphere Waveguide, *IEEE Transactions on Antennas and Propagation*, *69*(12), 8675–8688, doi:10.1109/TAP.2021.3083753, conference Name: IEEE Transactions on Antennas and Propagation.

George, H. E., C. J. Rodger, M. A. Clilverd, K. Cresswell-Moorcock, J. B. Brundell, and N. R. Thomson (2019), Developing a Nowcasting Capability for X-Class Solar Flares Using VLF Radiowave

Propagation Changes., *Space Weather*, *17*(12), 1783–1799, doi:10.1029/2019SW002297, _eprint: https://onlinelibrary.wiley.com/doi/pdf/10.1029/2019SW002297.

Goodman, S. J., R. J. Blakeslee, W. J. Koshak, D. Mach, J. Bailey, D. Buechler, L. Carey, C. Schultz, M. Bateman, E. McCaul, and G. Stano (2013), The GOES-R Geostationary Lightning Mapper (GLM), *Atmospheric Research*, *125-126*, 34–49, doi:10.1016/j.atmosres.2013.01.006.

Gołkowski, M., S. R. Sarker, C. Renick, R. C. Moore, M. B. Cohen, A. Kułak, J. Młynarczyk, and J. Kubisz (2018), Ionospheric D Region Remote Sensing Using ELF Sferic Group Velocity, *Geophysical Research Letters*, *45*(23), 12,739–12,748, doi:10.1029/2018GL080108, _eprint: https://onlinelibrary.wiley.com/doi/pdf/10.1029/2018GL080108.

Gross, N. C., M. B. Cohen, R. K. Said, and M. Gołkowski (2018), Polarization of Narrowband VLF Transmitter Signals as an Ionospheric Diagnostic, *Journal of Geophysical Research: Space Physics*, *123*(1), 901–917, doi:10.1002/2017JA024907, _eprint: https://onlinelibrary.wiley.com/doi/pdf/10.1002/2017JA024907.

Haldoupis, C., M. Rycroft, E. Williams, and C. Price (2017), Is the "Earth-ionosphere capacitor" a valid component in the atmospheric global electric circuit?, *Journal of Atmospheric and Solar-Terrestrial Physics*, *164*, 127–131, doi:10.1016/j.jastp.2017.08.012.

Han, F., and S. A. Cummer (2010), Midlatitude daytime D region ionosphere variations measured from radio atmospherics, *Journal of Geophysical Research: Space Physics*, *115*(A10), doi:10.1029/2010JA015715, _eprint: https://onlinelibrary.wiley.com/doi/pdf/10.1029/2010JA015715.

Holzworth, R., and H. Volland (1986), Do we need a geoelectric index?, *Eos, Transactions American Geophysical Union*, *67*(26), 545–548, doi:10.1029/EO067i026p00545-01, _eprint: https://onlinelibrary.wiley.com/doi/pdf/10.1029/EO067i026p00545-01.

Holzworth, R. H., T. Onsager, P. Kintner, and S. Powell (1984), Planetary-Scale Variability of the Fair-Weather Vertical Electric Field in the Stratosphere, *Physical Review Letters*, *53*(14), 1398–1401, doi:10.1103/PhysRevLett.53.1398, publisher: American Physical Society.

Holzworth, R. H., E. A. Bering, M. F. Kokorowski, E. H. Lay, B. Reddell, A. Kadokura, H. Yamagishi, N. Sato, M. Ejiri, H. Hirosawa, T. Yamagami, S. Torii, F. Tohyama, M. Nakagawa, T. Okada, and R. L. Dowden (2005), Balloon observations of temporal variation in the global circuit compared to global lightning activity, *Advances in Space Research*, *36*(11), 2223–2228, doi:10.1016/j.asr.2005.07.009.

Holzworth, R. H., J. B. Brundell, M. P. McCarthy, A. R. Jacobson, C. J. Rodger, and T. S. Anderson (2021), Lightning in the Arctic, *Geophysical Research Letters*, *48*(7), e2020GL091,366, doi:10.1029/2020GL091366, _eprint: https://onlinelibrary.wiley.com/doi/pdf/10.1029/2020GL091366.

Huffman, G. J., D. T. Bolvin, D. Braithwaite, K.-L. Hsu, R. J. Joyce, C. Kidd, E. J. Nelkin, S. Sorooshian, E. F. Stocker, J. Tan, D. B. Wolff, and P. Xie (2020), Integrated Multi-satellite Retrievals for the Global Precipitation Measurement (GPM) Mission (IMERG), in *Satellite Precipitation Measurement: Volume 1*, edited by V. Levizzani, C. Kidd, D. B. Kirschbaum, C. D. Kummerow, K. Nakamura, and F. J. Turk, Advances in Global Change Research, pp. 343–353, Springer International Publishing, Cham, doi:10.1007/978-3-030-24568-9_19.

Hutchins, M. L., R. H. Holzworth, C. J. Rodger, and J. B. Brundell (2012), Far-Field Power of Lightning Strokes as Measured by the World Wide Lightning Location Network, *Journal of Atmospheric and Oceanic Technology*, *29*(8), 1102–1110, doi:10.1175/JTECH-D-11-00174.1, publisher: American Meteorological Society Section: Journal of Atmospheric and Oceanic Technology.

Jacobson, A. R., R. Holzworth, E. Lay, M. Heavner, and D. A. Smith (2007), Low-frequency ionospheric sounding with Narrow Bipolar Event lightning radio emissions: regular variabilities and solar-X-ray responses, *Annales Geophysicae*, *25*(10), 2175–2184, doi:10.5194/angeo-25-2175-2007, publisher: Copernicus GmbH.

Jacobson, A. R., X.-M. Shao, and R. Holzworth (2010), Full-wave reflection of lightning long-wave radio pulses from the ionospheric D region: Comparison with midday observations of broadband lightning signals, *Journal of Geophysical Research: Space Physics*, *115*(A5), doi:10.1029/2009JA014540, _eprint: https://onlinelibrary.wiley.com/doi/pdf/10.1029/2009JA014540.

Jaynes, A. N., and M. E. Usanova (Eds.) (2020), *The Dynamic Loss of Earth's Radiation Belts - 1st Edition*.

Jánský, J., and V. P. Pasko (2014), Charge balance and ionospheric potential dynamics in time-dependent global electric circuit model, *Journal of Geophysical Research: Space Physics*, *119*(12), 10,184–10,203, doi:10.1002/2014JA020326, _eprint: https://onlinelibrary.wiley.com/doi/pdf/10.1002/2014JA020326.

Lam, M. M., R. B. Horne, N. P. Meredith, S. A. Glauert, T. Moffat-Griffin, and J. C. Green (2010), Origin of energetic electron precipitation >30 keV into the atmosphere, *Journal of Geophysical Research: Space Physics*, *115*(A4), doi:10.1029/2009JA014619, _eprint: https://onlinelibrary.wiley.com/doi/pdf/10.1029/2009JA014619.

Lay, E. H., X.-M. Shao, and A. R. Jacobson (2014), D region electron profiles observed with substantial spatial and temporal change near thunderstorms, *Journal of Geophysical Research: Space Physics*, *119*(6), 4916–4928, doi:10.1002/2013JA019430, _eprint: https://onlinelibrary.wiley.com/doi/pdf/10.1002/2013JA019430.

Levine, E. V., P. J. Sultan, and L. J. Teig (2019), A Parameterized Model of X-Ray Solar Flare Effects on the Lower Ionosphere and HF Propagation, *Radio Science*, *54*(2), 168–180, doi:10.1029/2018RS006666, _eprint: https://onlinelibrary.wiley.com/doi/pdf/10.1029/2018RS006666.

Lindsey, D., T. J. Schmit, W. M. M. Jr, C. P. Jewitt, M. M. Gunshor, and L. Grasso (2012), 10.35 m: atmospheric window on the GOES-R Advanced Baseline Imager with less moisture attenuation, *Journal of Applied Remote Sensing*, *6*(1), 063,598, doi:10.1117/1.JRS.6.063598, publisher: SPIE.

Mach, D. M., H. J. Christian, R. J. Blakeslee, D. J. Boccippio, S. J. Goodman, and W. L. Boeck (2007), Performance assessment of the Optical Transient Detector and Lightning Imaging Sensor, *Journal of Geophysical Research: Atmospheres*, *112*(D9), doi:10.1029/2006JD007787, _eprint: https://onlinelibrary.wiley.com/doi/pdf/10.1029/2006JD007787.

Mach, D. M., R. J. Blakeslee, M. G. Bateman, J. C. Bailey, C. . Mach, R. J. Blakeslee, M. G. Bateman, and J. C. Bailey (2009), Electric fields, conductivity, and estimated currents from aircraft overflights of electrified clouds, *J. Geophys. Res*, *114*, 10,204, doi:10.1029/2008JD011495.

Mach, D. M., R. J. Blakeslee, and M. G. Bateman (2011), Global electric circuit implications of combined aircraft storm electric current measurements and satellite-based diurnal lightning statistics, *Journal of*

Geophysical Research: Atmospheres, *116*(D5), doi:10.1029/2010JD014462, publisher: John Wiley & Sons, Ltd.

Markowski, P., and Y. Richardson (2011), *Mesoscale Meteorology in Midlatitudes*, John Wiley & Sons, google-Books-ID: MDeYosfLLEYC.

Marshall, R. A., and C. M. Cully (2020), Chapter 7 - Atmospheric effects and signatures of high-energy electron precipitation, in *The Dynamic Loss of Earth's Radiation Belts*, edited by A. N. Jaynes and M. E. Usanova, pp. 199–255, Elsevier, doi:10.1016/B978-0-12-813371-2.00007-X.

Marshall, R. A., and U. S. Inan (2010), Two-dimensional frequency domain modeling of lightning EMP-induced perturbations to VLF transmitter signals, *Journal of Geophysical Research: Space Physics*, *115*(A6), doi:10.1029/2009JA014761, _eprint: https://onlinelibrary.wiley.com/doi/pdf/10.1029/2009JA014761.

McCormick, J. C., M. B. Cohen, N. C. Gross, and R. K. Said (2018), Spatial and Temporal Ionospheric Monitoring Using Broadband Sferic Measurements, *Journal of Geophysical Research: Space Physics*, *123*(4), 3111–3130, doi:10.1002/2017JA024291, _eprint: https://onlinelibrary.wiley.com/doi/pdf/10.1002/2017JA024291.

Meraner, K., and H. Schmidt (2018), Climate impact of idealized winter polar mesospheric and stratospheric ozone losses as caused by energetic particle precipitation, *Atmospheric Chemistry and Physics*, *18*(2), 1079–1089, doi:10.5194/ACP-18-1079-2018, publisher: Copernicus GmbH.

Millan, R. M., and R. M. Thorne (2007), Review of radiation belt relativistic electron losses, *Journal of Atmospheric and Solar-Terrestrial Physics*, *69*(3), 362–377, doi:10.1016/j.jastp.2006.06.019.

Millan, R. M., R. P. Lin, D. M. Smith, and M. P. McCarthy (2007), Observation of relativistic electron precipitation during a rapid decrease of trapped relativistic electron flux, *Geophysical Research Letters*, *34*(10), doi:10.1029/2006GL028653, _eprint: https://onlinelibrary.wiley.com/doi/pdf/10.1029/2006GL028653.

Mitra, A. P. (1974), *Ionospheric Effects of Solar Flares*, *Astrophysics and Space Science Library*, vol. 46, Springer Netherlands, Dordrecht, doi:10.1007/978-94-010-2231-6.

NCEI, N. (2019), GOES Space Environment Monitor | NCEI, publisher: U.S. Department of Commerce.

Nesse Tyssøy, H., M. I. Sandanger, L.-K. G. Ødegaard, J. Stadsnes, A. Aasnes, and A. E. Zawedde (2016), Energetic electron precipitation into the middle atmosphere—Constructing the loss cone fluxes from MEPED POES, *Journal of Geophysical Research: Space Physics*, *121*(6), 5693–5707, doi: 10.1002/2016JA022752, _eprint: https://onlinelibrary.wiley.com/doi/pdf/10.1002/2016JA022752.

Nesse Tyssøy, H., M. Sinnhuber, T. Asikainen, S. Bender, M. A. Clilverd, B. Funke, M. van de Kamp, J. M. Pettit, C. E. Randall, T. Reddmann, C. J. Rodger, E. Rozanov, C. Smith-Johnsen, T. Sukhodolov, P. T. Verronen, J. M. Wissing, and O. Yakovchuk (2022), HEPPA III Intercomparison Experiment on Electron Precipitation Impacts: 1. Estimated Ionization Rates During a Geomagnetic Active Period in April 2010, *Journal of Geophysical Research: Space Physics*, *127*(1), e2021JA029,128, doi:10.1029/2021JA029128, _eprint: https://onlinelibrary.wiley.com/doi/pdf/10.1029/2021JA029128.

Norville, K., and R. Holzworth (1987), Global circuit variability from multiple stratospheric electrical measurements, *Journal of Geophysical Research: Atmospheres*, *92*(D5), 5685–5695, doi:10.1029/JD092iD05p05685, _eprint: https://onlinelibrary.wiley.com/doi/pdf/10.1029/JD092iD05p05685.

Parks, G. K. (2019), *Physics Of Space Plasmas: An Introduction*, CRC Press, google-Books-ID: fMfADwAAQBAJ.

Peck, E. D., C. E. Randall, J. C. Green, J. V. Rodriguez, and C. J. Rodger (2015), POES MEPED differential flux retrievals and electron channel contamination correction, *Journal of Geophysical Research: Space Physics*, *120*(6), 4596–4612, doi:10.1002/2014JA020817, publisher: Blackwell Publishing Ltd.

Peterson, M. (2019), Research Applications for the Geostationary Lightning Mapper Operational Lightning Flash Data Product, *Journal of Geophysical Research: Atmospheres*, *124*(17-18), 10,205–10,231, doi: 10.1029/2019JD031054, _eprint: https://onlinelibrary.wiley.com/doi/pdf/10.1029/2019JD031054.

Pettit, J. M., C. E. Randall, E. D. Peck, D. R. Marsh, M. van de Kamp, X. Fang, V. L. Harvey, C. J. Rodger, and B. Funke (2019), Atmospheric Effects of >30-keV Energetic Electron Precipitation in the Southern Hemisphere Winter During 2003, *Journal of Geophysical Research: Space Physics*, *124*(10), 8138–8153, doi:10.1029/2019JA026868, _eprint: https://onlinelibrary.wiley.com/doi/pdf/10.1029/2019JA026868.

Pettit, J. M., C. E. Randall, E. D. Peck, and V. L. Harvey (2021), A New MEPED-Based Precipitating Electron Data Set, *Journal of Geophysical Research: Space Physics*, *126*(12), e2021JA029,667, doi: 10.1029/2021JA029667, _eprint: https://onlinelibrary.wiley.com/doi/pdf/10.1029/2021JA029667.

Picone, J. M., A. E. Hedin, D. P. Drob, and A. C. Aikin (2002), NRLMSISE-00 empirical model of the atmosphere: Statistical comparisons and scientific issues, *Journal of Geophysical Research: Space Physics*, *107*(A12), SIA 15–1–SIA 15–16, doi:10.1029/2002JA009430, _eprint: https://onlinelibrary.wiley.com/doi/pdf/10.1029/2002JA009430.

Qian, L., W. Wang, A. G. Burns, P. C. Chamberlin, A. Coster, S.-R. Zhang, and S. C. Solomon (2019), Solar Flare and Geomagnetic Storm Effects on the Thermosphere and Ionosphere During 6–11 September 2017, *Journal of Geophysical Research: Space Physics*, *124*(3), 2298–2311, doi:10.1029/2018JA026175, _eprint: https://onlinelibrary.wiley.com/doi/pdf/10.1029/2018JA026175.

Rakov, V. A., and M. A. Uman (2003), *Lightning: Physics and Effects*, Cambridge University Press, google-Books-ID: NviMsvVOHJ4C.

Ratcliffe, J. A. (1959), *The Magneto-ionic Theory and Its Applications to the Ionosphere*, University Press, google-Books-ID: lRQvAAAAIAAJ.

Raulin, J.-P., F. C. P. Bertoni, H. R. Gavilán, W. Guevara-Day, R. Rodriguez, G. Fernandez, E. Correia, P. Kaufmann, A. Pacini, T. R. C. Stekel, W. L. C. Lima, N. J. Schuch, P. R. Fagundes, and R. Hadano (2010), Solar flare detection sensitivity using the South America VLF Network (SAVNET), *Journal of Geophysical Research: Space Physics*, *115*(A7), doi:10.1029/2009JA015154, _eprint: https://onlinelibrary.wiley.com/doi/pdf/10.1029/2009JA015154.

Roble, R. G. (1991), On modeling component processes in the Earth's global electric circuit, *Journal of Atmospheric and Terrestrial Physics*, *53*(9), 831–847, doi:10.1016/0021-9169(91)90097-Q, publisher: Pergamon.

Rodger, C. J., S. Werner, J. B. Brundell, E. H. Lay, N. R. Thomson, R. H. Holzworth, and R. L. Dowden (2006), Detection efficiency of the VLF World-Wide Lightning Location Network (WWLLN): initial case

study, *Annales Geophysicae*, *24*(12), 3197–3214, doi:10.5194/angeo-24-3197-2006, publisher: Copernicus GmbH.

Rodger, C. J., B. R. Carson, S. A. Cummer, R. J. Gamble, M. A. Clilverd, J. C. Green, J.-A. Sauvaud, M. Parrot, and J.-J. Berthelier (2010a), Contrasting the efficiency of radiation belt losses caused by ducted and nonducted whistler-mode waves from ground-based transmitters, *Journal of Geophysical Research: Space Physics*, *115*(A12), doi:10.1029/2010JA015880, _eprint: https://onlinelibrary.wiley.com/doi/pdf/10.1029/2010JA015880.

Rodger, C. J., M. A. Clilverd, J. C. Green, and M. M. Lam (2010b), Use of POES SEM-2 observations to examine radiation belt dynamics and energetic electron precipitation into the atmosphere, *Journal of Geophysical Research: Space Physics*, *115*(A4), doi:10.1029/2008JA014023, _eprint: https://onlinelibrary.wiley.com/doi/pdf/10.1029/2008JA014023.

Rycroft, M. J., S. Israelsson, and C. Price (2000), The global atmospheric electric circuit, solar activity and climate change, *Journal of Atmospheric and Solar-Terrestrial Physics*, *62*(17), 1563–1576, doi:10.1016/S1364-6826(00)00112-7.

Rycroft, M. J., A. Odzimek, N. F. Arnold, M. Füllekrug, A. Kułak, and T. Neubert (2007), New model simulations of the global atmospheric electric circuit driven by thunderstorms and electrified shower clouds: The roles of lightning and sprites, *Journal of Atmospheric and Solar-Terrestrial Physics*, *69*(17), 2485–2509, doi:10.1016/j.jastp.2007.09.004.

Sauer, H. H., and D. C. Wilkinson (2008), Global mapping of ionospheric HF/VHF radio wave absorption due to solar energetic protons, *Space Weather*, *6*(12), doi:10.1029/2008SW000399, _eprint: https://onlinelibrary.wiley.com/doi/pdf/10.1029/2008SW000399.

Shao, X.-M., E. H. Lay, and A. R. Jacobson (2013), Reduction of electron density in the night-time lower ionosphere in response to a thunderstorm, *Nature Geoscience*, *6*(1), 29–33, doi:10.1038/ngeo1668, number: 1 Publisher: Nature Publishing Group.

Siingh, D., V. Gopalakrishnan, R. P. Singh, A. K. Kamra, S. Singh, V. Pant, R. Singh, and A. K. Singh

(2007), The atmospheric global electric circuit: An overview, *Atmospheric Research*, *84*(2), 91–110, doi:10.1016/j.atmosres.2006.05.005.

Sinnhuber, M., and B. Funke (2020), Chapter 9 - Energetic electron precipitation into the atmosphere, in *The Dynamic Loss of Earth's Radiation Belts*, edited by A. N. Jaynes and M. E. Usanova, pp. 279–321, Elsevier, doi:10.1016/B978-0-12-813371-2.00009-3.

Sinnhuber, M., H. Nieder, and N. Wieters (2012), Energetic Particle Precipitation and the Chemistry of the Mesosphere/Lower Thermosphere, *Surveys in Geophysics*, *33*(6), 1281–1334, doi:10.1007/s10712-012-9201-3.

Thomas, J. N., R. H. Holzworth, and M. P. McCarthy (2009), In situ measurements of contributions to the global electrical circuit by a thunderstorm in southeastern Brazil, *Atmospheric Research*, *91*(2), 153–160, doi:10.1016/j.atmosres.2008.03.026.

Thomson, N. R. (1993), Experimental daytime VLF ionospheric parameters, *Journal of Atmospheric and Terrestrial Physics*, *55*(2), 173–184, doi:10.1016/0021-9169(93)90122-F.

Thomson, N. R., and M. A. Clilverd (2001), Solar flare induced ionospheric D-region enhancements from VLF amplitude observations, *Journal of Atmospheric and Solar-Terrestrial Physics*, *63*(16), 1729–1737, doi:10.1016/S1364-6826(01)00048-7.

Toledo-Redondo, S., M. Parrot, and A. Salinas (2012), Variation of the first cut-off frequency of the Earth-ionosphere waveguide observed by DEMETER, *Journal of Geophysical Research: Space Physics*, *117*(A4), doi:10.1029/2011JA017400, _eprint: https://onlinelibrary.wiley.com/doi/pdf/10.1029/2011JA017400.

Troshichev, O. A., A. Frank-Kamenetsky, G. Burns, M. Fuellekrug, A. Rodger, and V. Morozov (2004), The relationship between variations of the atmospheric electric field in the southern polar region and thunderstorm activity, *Advances in Space Research*, *34*(8), 1801–1805, doi:10.1016/j.asr.2003.07.063.

Uman, M. A., and E. P. Krider (1982), A Review of Natural Lightning: Experimental Data and Modeling, *IEEE Transactions on Electromagnetic Compatibility*, *EMC-24*(2), 79–112, doi:10.1109/TEMC.1982.304006, conference Name: IEEE Transactions on Electromagnetic Compatibility.

van de Kamp, M., A. Seppälä, M. A. Clilverd, C. J. Rodger, P. T. Verronen, and I. C. Whittaker (2016), A model providing long-term data sets of energetic electron precipitation during geomagnetic storms, *Journal of Geophysical Research: Atmospheres*, *121*(20), 12,520–12,540, doi:10.1002/2015JD024212, _eprint: https://onlinelibrary.wiley.com/doi/pdf/10.1002/2015JD024212.

van de Kamp, M., C. J. Rodger, A. Seppälä, M. A. Clilverd, and P. T. Verronen (2018), An Updated Model Providing Long-Term Data Sets of Energetic Electron Precipitation, Including Zonal Dependence, *Journal of Geophysical Research: Atmospheres*, *123*(17), 9891–9915, doi:10.1029/2017JD028253, _eprint: https://onlinelibrary.wiley.com/doi/pdf/10.1029/2017JD028253.

Volland, H. (1995), *Handbook of Atmospheric Electrodynamics*, CRC Press, google-Books-ID: JO_BVJnc20sC.

Wait, J. R., and K. P. Spies (1964), *Characteristics of the Earth-ionosphere Waveguide for VLF Radio Waves*, U.S. Department of Commerce, National Bureau of Standards, google-Books-ID: jSOXDsgc8xcC.

Wenzel, D., N. Jakowski, J. Berdermann, C. Mayer, C. Valladares, and B. Heber (2016), Global ionospheric flare detection system (GIFDS), *Journal of Atmospheric and Solar-Terrestrial Physics*, *138-139*, 233–242, doi:10.1016/j.jastp.2015.12.011.

Westerlund, S., and F. H. Reder (1973), VLF radio signals propagating over the Greenland ice-sheet, *Journal of Atmospheric and Terrestrial Physics*, *35*(8), 1475–1491, doi:10.1016/0021-9169(73)90149-9.

Whipple, F. J. W., and F. J. Scrase (1936), Point discharge in the electric field of the Earth: An analysis of continuous records obtained at Kew Observatory, *HM Stationery Office*, *No. 68*.

Williams, E. R. (2009), The global electrical circuit: A review, *Atmospheric Research*, *91*(2), 140–152, doi:10.1016/j.atmosres.2008.05.018.

Wilson, C. T. R. (1921), Investigations on Lightning Discharges and on the Electric Field of Thunderstorms, *Monthly Weather Review*, *49*(4), 241–241, doi:10.1175/1520-0493(1921)49<241a:IOLDAO>2.0.CO;2, publisher: American Meteorological Society Section: Monthly Weather Review.

Yando, K., R. M. Millan, J. C. Green, and D. S. Evans (2011), A Monte Carlo simulation of the NOAA POES Medium Energy Proton and Electron Detector instrument, *Journal of Geophysical Research: Space Physics*, *116*(A10), doi:10.1029/2011JA016671, _eprint: https://onlinelibrary.wiley.com/doi/pdf/10.1029/2011JA016671.

Yasyukevich, Y., E. Astafyeva, A. Padokhin, V. Ivanova, S. Syrovatskii, and A. Podlesnyi (2018), The 6 September 2017 X-Class Solar Flares and Their Impacts on the Ionosphere, GNSS, and HF Radio Wave Propagation, *Space Weather*, *16*(8), 1013–1027, doi:10.1029/2018SW001932, _eprint: https://onlinelibrary.wiley.com/doi/pdf/10.1029/2018SW001932.

Zangwill, A. (2013), *Modern Electrodynamics*, Cambridge University Press.